FRACTURE-DIRECTED STEERABLE NEEDLES

By

FAN YANG

A dissertation submitted in partial fulfillment of
the requirements for the degree of

DOCTOR OF PHILOSOPHY

WASHINGTON STATE UNIVERSITY
Department of Mechanical and Materials Engineering

AUGUST 2020

To the Faculty of Washington State University:

The members of the Committee appointed to examine the dissertation of FAN YANG find it satisfactory and recommend that it be accepted.

John P. Swensen, Ph.D., Chair

Arda Gozen, Ph.D., Ph.D.

Kuen-Ren (Roland) Chen, Ph.D.

ACKNOWLEDGEMENTS

First of all, I would like to express my sincere appreciation to my advisor and mentor, Dr.Swensen, for his unlimited support and valuable advice. Thank you for encouraging and inspiring me to keep the ball rolling, I would never complete my doctorate without your help.

I would also like to thank my former and current committee members, Dr.Gozen, Dr.Chen, Dr.Taylor, and Dr.Jerath. Thank you for your time and assistance with steerable needle research and my PhD study.

I wish to say thank you to all my fellas: Mahdieh, Lee, Emily, Ben, Heon, and Alex, for being considerate, caring, supportive, and intelligent. I've learned a lot from you guys. Particularly, I'd like to thank Mahdieh Babaiasl for her assistance with my research and thank Lee Taylor for sharing his expertise in coding and hardware. I've really enjoyed the time as a graduate student in the M3 robotics lab.

My appreciation also goes to all my friends in the States, especially Matt Fan, Yao Chen, Jialong Ning and Che-hao Yang. Thanks to all of you for your kind help and continuously encouragements.

Finally, I would like to acknowledge my family. I want to express my deepest gratitude to my mother, Lijun Yang, who always encouraging me and always being my biggest cheerleader in my life. And I much appreciate my fiancee Fei Zhong and her bunny Elfin. Thanks for taking on all the extra work at home and providing me

endless support. This dissertation would not be possible without anyone of you.

FRACTURE-DIRECTED STEERABLE NEEDLES

Abstract

by Fan Yang, Ph.D.
Washington State University
August 2020

Chair: John P. Swensen

Steerable needles have been widely researched for many years. Since they have the availability to steer to a target point avoiding obstacles and correcting themselves for disturbances, they have great potential to improve the accuracy of both therapies and biopsies. However, the ability to make late-insertion corrections was limited by the attainable insertion radius of curvature. This dissertation describes the design and modeling of a new class of steerable needles, the insertion process is to first control the direction of the tissue fracture with an inner nitinol wire and then follow with a hollow nitinol tube. This insertion approach has the capability to achieve a 6.9 mm insertion radius of curvature inside soft tissue phantoms with only 128Kpa Young's Modulus, and the radius of curvature is controllable from the lower limit up to a near-infinite insertion radius of curvature based on the tissue properties and needle step length. A comprehensive predictive model was developed based on experimental data to predict the insertion radius of curvature across a wide range of tissue stiffnesses and a complete finite element analysis model was conducted to validate it. A variety of inner stylet geometries are investigated using tissue phantoms with multiple stiffnesses, and discrete-step kinematic models of motion are derived heuristically from the experiments. A RG-RRT path planning algorithm and a straight-curve-straight heuristic path planning algorithm were developed to steer the needle in 2D or 3D space with obstacles. Both of them have the capability to conduct closed-loop re-planning based on real-time visual feedback. This steerable needles research was motivated by reducing insertion radius, improving insertion accuracy, and ameliorate the clinical outcome.

TABLE OF CONTENTS

Page

CHAPTER

LIST OF FIGURES

LIST OF TABLES

Dedication

dedicated to ...

(This page is optional)

CHAPTER ONE

INTRODUCTION

1.1 Motivation

Minimally invasive surgery has played an essential role in medical treatment surgery for decades. It's much safer than open surgeries, allows patients to recover more quickly, and the healing process is less unpleasant. The steerable needles research inherits the ideas and advantages of minimally invasive surgery. They are the least invasive tools for surgical propose, self-heal fast, especially at the small gauge. Needle with 1mm diameter or smaller can limit the risk of complication and patient discomfort during a medical procedure [54].

Robotic-aided steerable needles have even more advantages, it's capable to work in an imaging environment that contains ionizing radiation, self-correct its trajectory accurately, and operates consistently steady with no fatigue. Computational tools provide the ability of complex trajectory control and multiple targets reaching with only one initial insertion point.

The steerable needles have three major potential applications: biopsies, ablation electrodes, and radioactive seeds. These applications are highly relevant to the diagnoses and treatments of cancer. The capability to turn in a much smaller radius makes the steerable needles have caught attentions and expectations from the biomedical community. Various simulators in surgical planning were developed and researched

[3, 63, 10].

Biopsies are commonly seen in the clinic, approximately 30 thousand liver biopsies, 1.6 million breast biopsies and 1 million prostate biopsies were performed each year within the U.S. [19, 37, 26]. About 191,930 new cases of prostate cancer will be diagnosed each year, and about 42,810 new cases of liver cancer will be diagnosed each year [37, 36]. The common treatment for prostate cancer is transperineal brachytherapy, where radioactive seeds were implanted through thin needles to the focus [5]. Thermal ablation was often used to treat tumors that have a relatively small size, below 5mm in diameter. A thermal ablation directed at the needle tip was inserted under ultrasound image guidance [6]. In transperineal brachytherapy, to achieve a precise delivery is quite challenging especially with organ deformation and displacement around the target area. An enormous error could take place when the needle is tangential to the prostate capsule wall upon penetration, a trajectory correction upon penetrating the capsule wall is essential for improving the success rate of the insertion [13, 22]. Similarly, due to the different mechanical properties of liver tumors and their surrounding tissue, the tumors present comparable behaviors with respect to needle penetration.

The needle insertions performed mostly in the clinical environment use needles with standard bevel tips, this bevel tip is a simple and economic design that helps to penetrate tissue and skin during medical procedures. Nevertheless, the bevel tip tends to deflect during insertions because of the asymmetric forces generated at the bevel surface. As the needle is pushed into the tissue further, this interaction force keeps pushing the bevel surface to cause a considerable tip placement error. This needle deflection was an unwanted needle behavior for physicians, some physicians started to add an offset based on experience at the beginning of insertion to cancel out this deflection. In the research of steerable needles, rather than trying to reduce the deflection effect, researchers enhanced this deflection effect by making needles more flexible. With properly generated kinematic models and appropriate model-based control method, the needle can be precisely driven by robots to reach a specified target location. This became the framework of bevel tip steerable needles, a dominant steering approach in the steerable needles field.

Although there are many different types of steerable needles with various mechanical design, steering techniques, and control algorithms exist, the objectives of steerable needle research have always been improving the flexibility and precision of insertion. In other words, reduce the insertion radius to reorient the needle more rapidly, and reduce the error of needle tip placement during insertion.

1.2 Related Work

The steerable needles that have been developed can be classified into two major categories, passive steerable needles, and active steerable needles. During passive needle insertion, bending forces are a direct result of the needle–tissue interactions.

For active needles, either the tip or the cannula shape can be modified without tissue contact. During insertion in tissue, this modification typically also translates to a cannula deformation. Passive steering techniques include base manipulation and bevel tip steering. Active steering techniques contain active cannula, active pre-bent steering, programmable bevel tip steering, tendon actuated active tip steering, and pre-curved stylet steering [65].

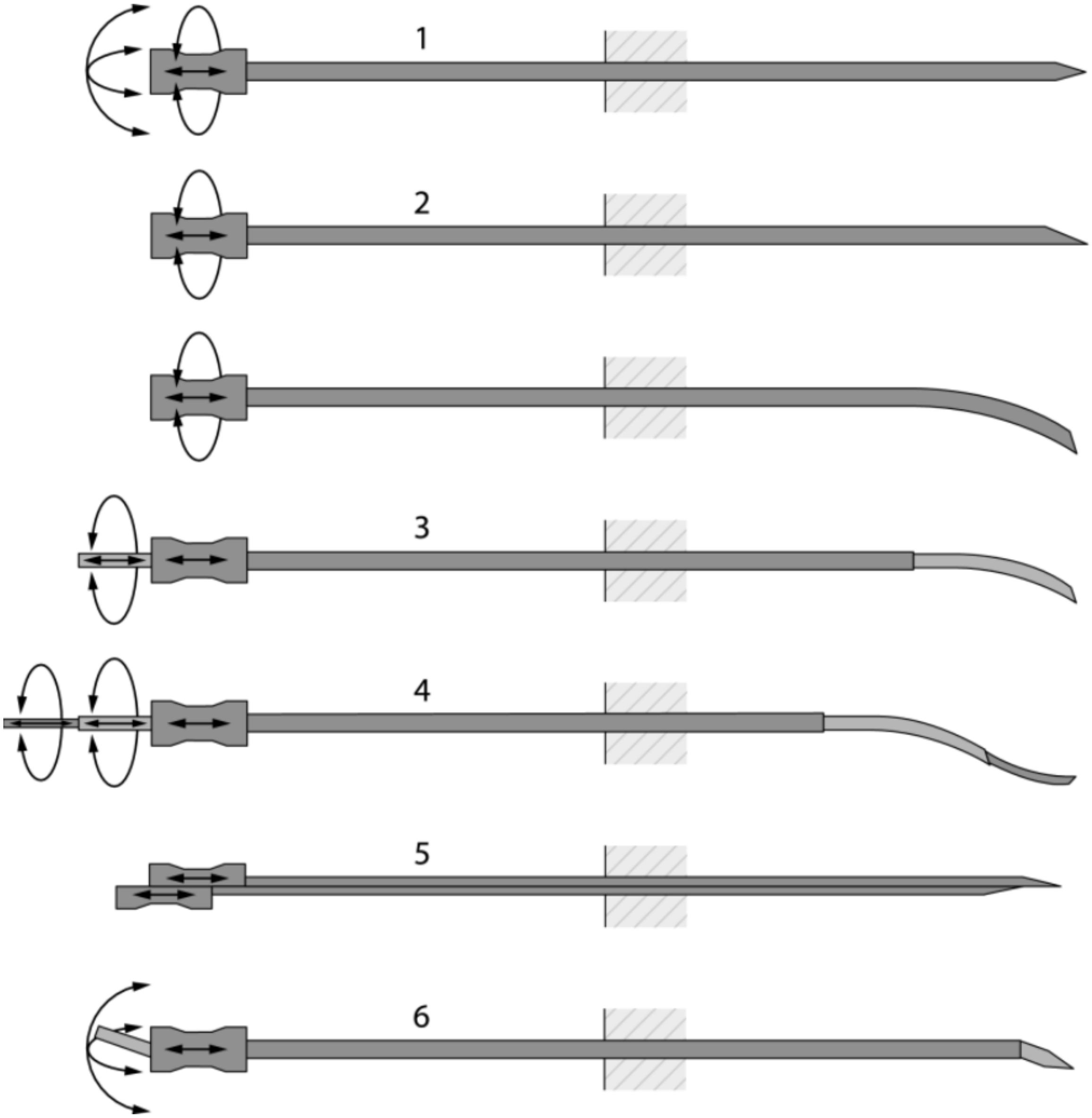

Figure 1.1: Illustration of 6 types of steerable needles in 2 major categories and their degrees of freedom in actuation. The first 2 types of steering techniques are passive steering and the other 4 types are active steering. The depicted techniques are, respectively, (1) base manipulation, (2) bevel tip (with and without preset curve), (3) pre-curved stylet, (4) Active cannula, (5) programmable bevel, and 6) tendon actuated tip steering. The programmable bevel is here presented with two segments, versions with four segments are available as well. © 2014 IEEE.

The base manipulation steering is one of the primitive models that automatically steer a needle. The motion of the base structure was controlled robotically by an open-loop control method to administer the needle tip position and orientation with respect to the target point. This early-stage approach has limited tip placement accuracy due to its depth dependence property, where the moment arm decreases and the tip resistance increases as the insertion depth increase [14, 24, 51].

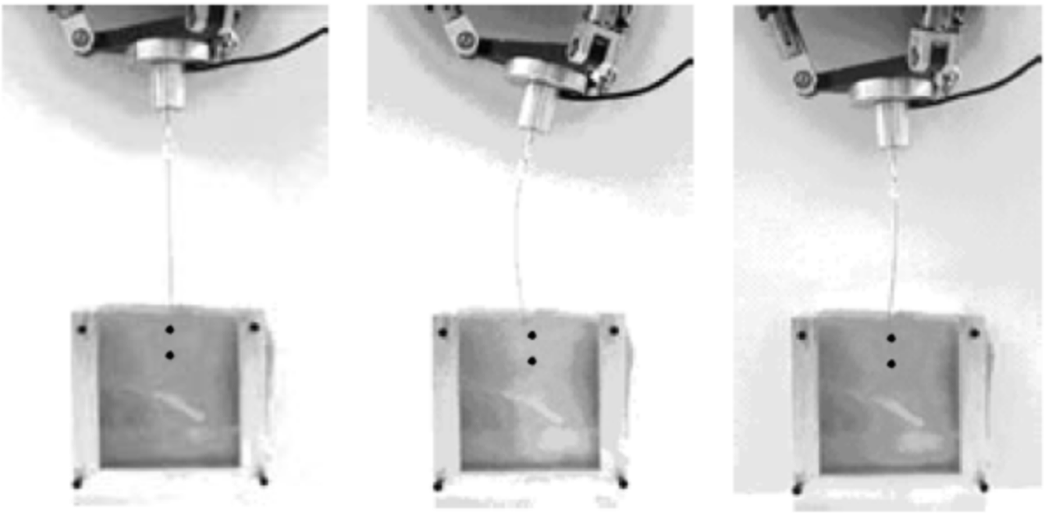

Figure 1.2: Obstacle avoidance by changing the needle base orientation during insertion. Retracted from [24]

The bevel tip steering approach was the focus of many research groups because of the preferable lowest achievable insertion radius compare to the cone or triangular pyramid tip. The insertion radius of a bevel tip steerable needle is also controllable through duty cycling technique [44, 20]. The known minimal insertion radius of bevel tip steerable needles was 52.3mm in ex vivo tissue and 121mm in tissue phantom [35, 60].

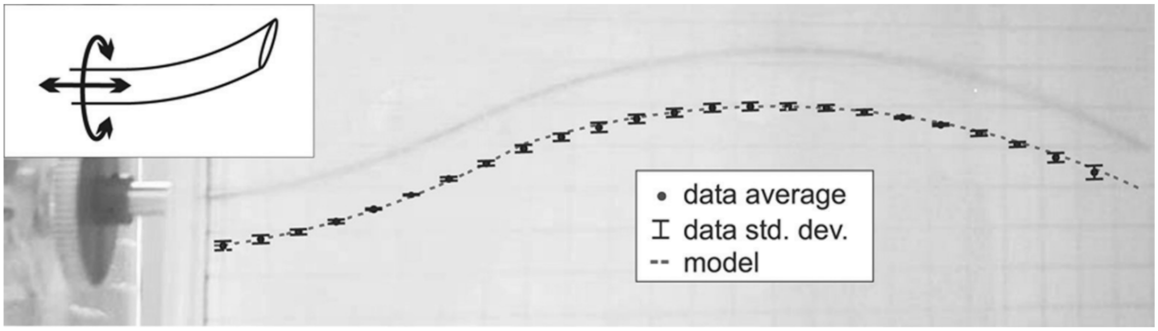

Figure 1.3: A bevel tip steerable needle being inserted into tissue phantom.© 2014 IEEE.

The pre-curved stylet steering was first introduced by Okazawa *et al.*[42] where a pre-curved stylet is extended from a tube to create a controllable prebend. A prototype of this approach was made and tested in ex vivo tissue. The reported steerability over this method was a 30 mm of lateral tip motion versus a 100 mm insertion. A simple conversion to describe the steerability in insertion radius was made, a curve with a constant curvature was fitted into the reported trajectory retracted from the original paper, the converted insertion radius was approximately 325mm.

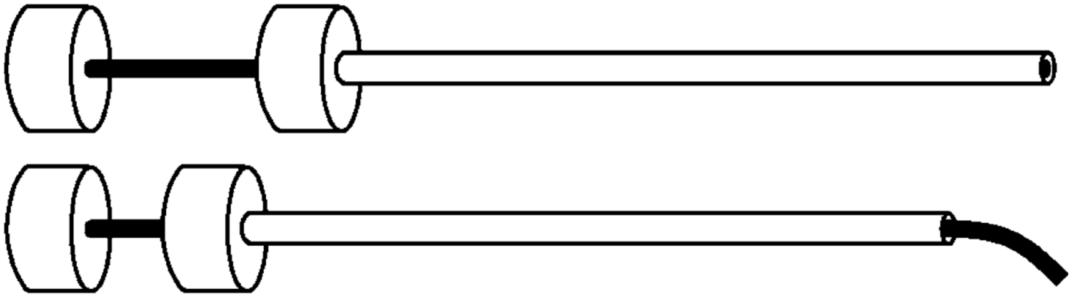

Figure 1.4: pre-curved stylet steering concept presenting the stylet withdrawn(top) and extended(bottom). As the pre-curved wire and outer tube are translated with respect to each other, the length of the exposed pre-curved wire is changed.Retracted from [42]

.

An active cannula consists of multiple pre-curved concentric tubes, cannula tip position, orientation and the resultant curvature of each segment can be controlled by rotating and extending the tubes with respect to one another. A typical active cannula was shown in figure 1.5. The active cannula steering uses forces that generated internally to actuate, so active cannula does not need environmental contact to steer which means the achievable insertion radius does not depend on Young's Modulus of the surrounding tissue. However, the torsion balance can be easily disturbed, this disturbance could lead to both excessive placement errors and sudden snapping motions between stable cannula configurations [70, 17]. The reported best curvature was 0.037 mm-1, which can be converted to a minimal achievable insertion radius 27mm [8].

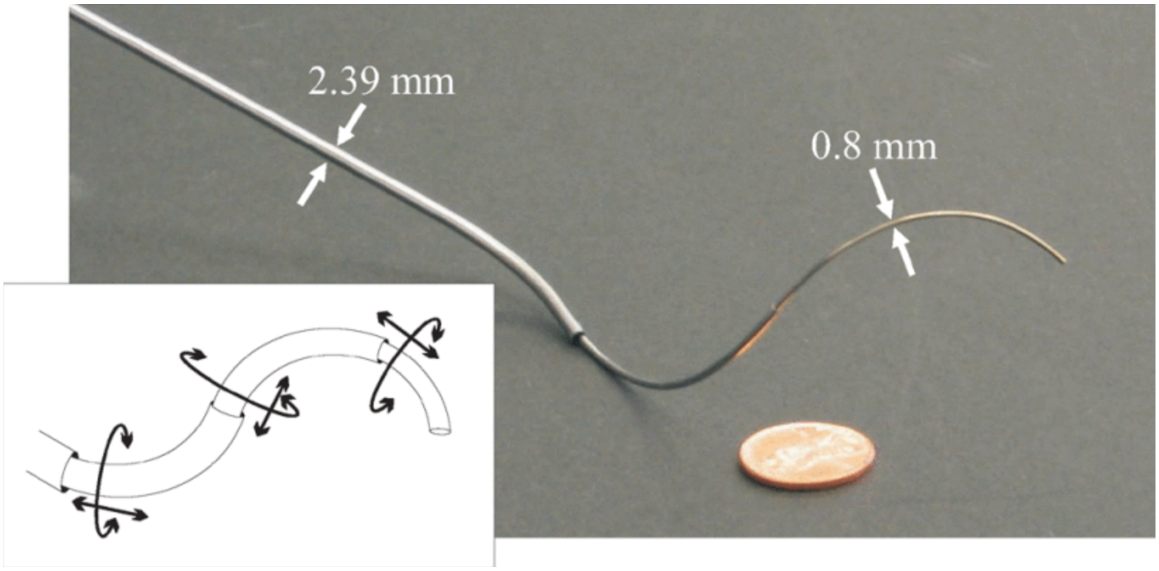

Figure 1.5: A typical three-tubes active cannula made of superelastic nitinol. The drawing at bottom left indicates the active cannula's degrees of freedom. Retracted from [70].

.

The programmable bevel tip steering method is based on biomimetic concepts [31]. The latest design consists of four interlocked quarter cylinders with a beveled tip that can slide along one another [56]. The reported path radius for the double-segment actuation directions is approximately 100mm. And the single-segment actuation directions, a path radius of 59mm can be reached. The two major limitations of programmable bevel tip steering is the large overall size and restricted insertion orientations(eight principal directions). The improved prototype meant for 2-D navigation tasks (using a two-segment needle) was measured to a 4mm diameter, and the latest prototype allows 3-D navigation tasks (using a four-segment needle) that was measured to an 8mm diameter [32, 9].

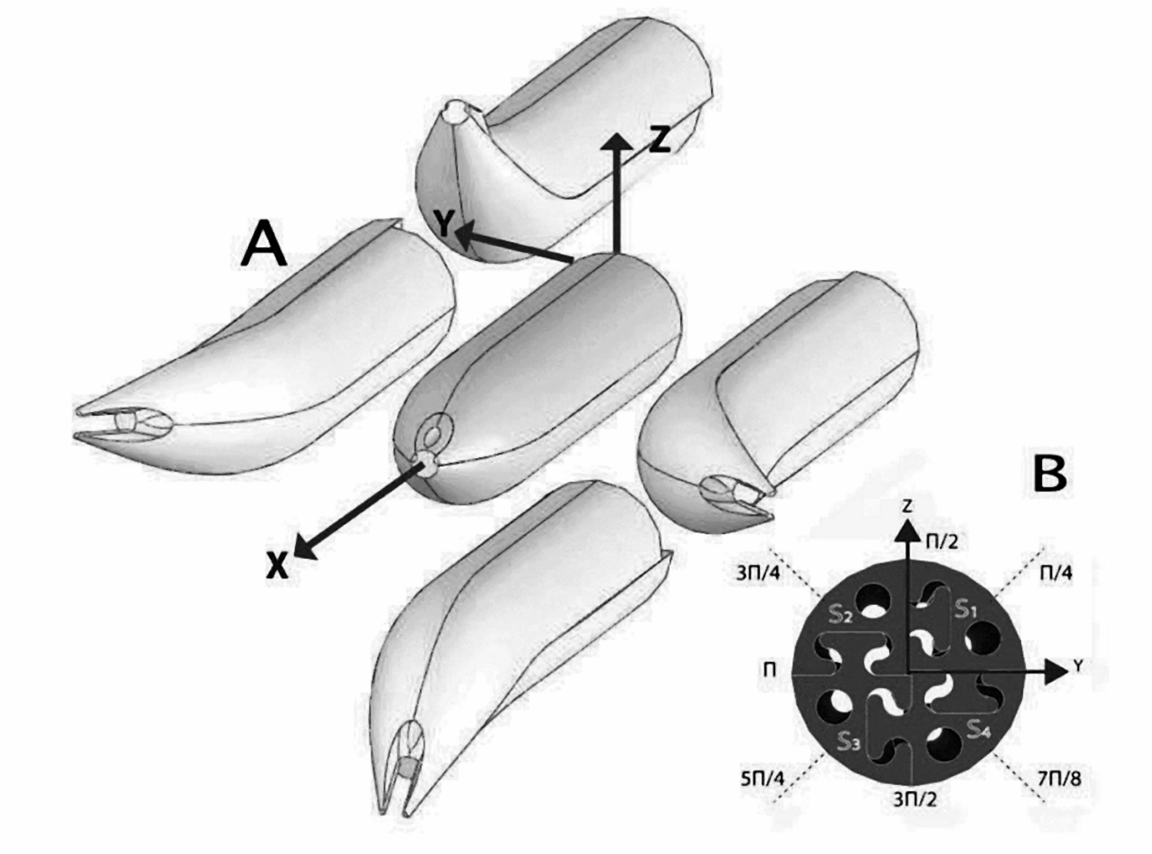

Figure 1.6: The cross section of the programmable bevel tip steerable needle consisting of four interlocked segments: A) needle steering direction; B) cross section of the needle with 8 primary direction. Retracted from [56].

.

The tendon actuated concept was widely involved in medical devices and surgical robotics design [77, 33, 11]. However, designs and prototypes of tendon actuated steerable needles are rare. This steering approach is similar to the bevel tip steering method, which uses the interaction forces between needle tip and tissue to attain various insertion radius and orientation. The achievable insertion radius range reported in a recent active tip steering is from 227mm to 1333mm [33]..

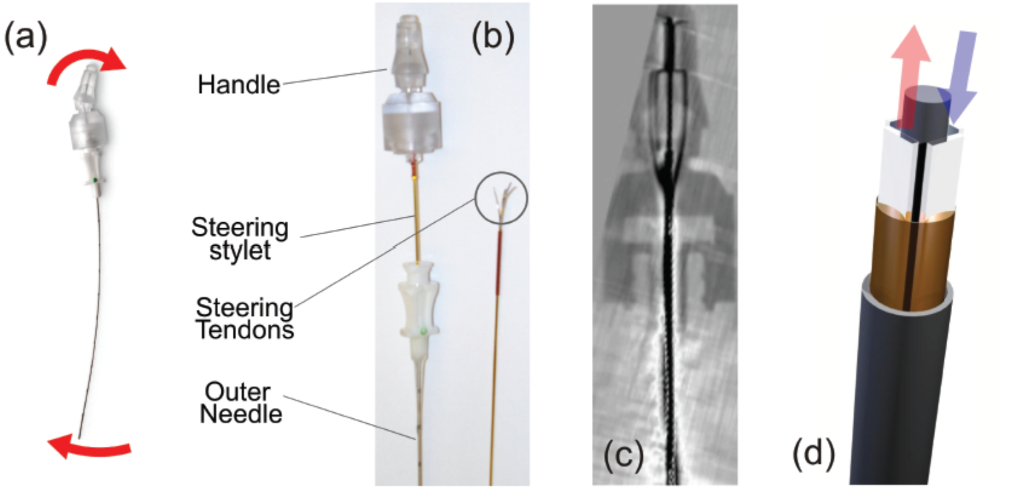

Figure 1.7: A tendon-actuated steerable needle. (a) It can be deflected by manipulating a handle at its base. (b) The complete needle consists of a stylet and outer cannula, where the stylet contains the tendons and generates the steering. On the right, a stylet with handle removed is shown. (c) A CT scan of an intact needle shows how tendons are routed. (d) A CAD illustration of the needle: the tendons surround a central flexible core, and are covered by a polymeric membrane to keep them in place.Retracted from [33].

.

1.3 Contributions

The presented work ”Fracture-directed steerable needles” in this dissertation is in the family of pre-curved stylet steerable needles and related to the primitive steerable needle work by Okazawa *et al.*[42].

The major contributions of this dissertation can be summarized as follows:

(1) The needle insertion platform contains a unique tube-wire simultaneous rotation mechanism which improves the accuracy of needle re-orientation and reduces the needle rotation lag caused by needle-tissue friction. Several limit switches were added to prevent over retraction or insertion of the inner nitinol wire so the actual step length accurately falls under the range of the predictive model. The capability of manipulating needle tip accurately and precisely to target location was improved noticeably [42, 76].

(2) A predictive mathematical model for predicting the resultant insertion radius was created, and the bending stiffness boundaries for stylet size selection based on tissue properties were found. Finite element analysis was also conducted to provide cross-validation to the predictive model which established from experiments. The insertion radius of paired stylets(one pair of tube and wire that being selected in specific sizes made of superelastic nitinol or thermoplastic polyurethane) was significantly improved and can be accurately predicted. The smallest achievable insertion radius of fracture-directed steerable needles is 6.9mm(within 20%SEBS tissue phantom) [76], compare to the best equivalent insertion radius reported in literature, 26mm - 27mm [8, 41]. The predictive model predicts the insertion curvature of each step based on the current step length and tissue properties.

(3)A path planning & closed-loop re-planning algorithm based on a rapidly-exploring random tree was developed based on the nonholonomic kinematic model of fracture-directed steerable needles. Another customized path planning algorithm targeting on minimizing path length and calculation expense was also developed. Both algorithms presented quality results in multi-obstacles environments.

1.4 Dissertation Overview

Chapter 1 introduced the medical motivation of fracture-directed steerable needles. Features, advantages, and disadvantages of different types of steerable needles were briefly discussed. The major contributions of fracture-directed steerable needles were also presented. Chapter 2 discussed fracture-directed steerable needles in detail. This chapter was separated into three parts, includes the design of needle insertion platform, experimental methods, and the establishment of predictive models for the insertion radius of curvature. Prior works were discussed more thoroughly and compared to the work presented in this dissertation. Chapter 3 presented two path planning algorithms based on a nonholonomic kinematic model, one is a traditional and mature algorithm named as reachability-guided rapidly-exploring random tree, the other is a customized straight-curve-straight planning strategy. A conclusion was made in chapter 4, and future works of fracture-directed steerable needles were also concluded in chapter 4.

CHAPTER TWO

FRACTURE-DIRECTED STEERABLE NEEDLES

2.1 Definitions and Notations

The definition of ”insertion radius of curvature” and ”resultant radius of curvature” are both stand for the combined radius of nitinol wire, tube, and tissue channel after following the wire with the tube. This combined radius of curvature is denoted by R_c. The reciprocal of R_c, $kappa_c$, is defined as ”resultant insertion curvature”.

The equations related to the bending stiffness and curvature for calculating multiple overlapped curved tubes has been developed by Webster *et. al.* [71]:

$$\kappa_C = \frac{\sum_{i=1}^{n} E_i I_i \kappa_i}{\sum_{i=1}^{n} E_i I_i} = \frac{K_t \kappa_t + K_b \kappa_b + K_w \kappa_w}{K_t + K_b + K_w} \tag{2.1}$$

whereκ_t, κ_b, κ_w and K_t, K_b, K_w are the curvature and bending stiffness of the tissue channel, tube, and wire, respectively. I_i is the cross-sectional moment of inertia and E is the Young’s Modulus.

$$K_i = E_i I_i \tag{2.2}$$

The product of the Young’s Modulus (Modulus of Elasticity) and cross-sectional moment of inertia is bending stiffness.

2.2 Related Work

The robotic-aided steerable needles have been thoroughly researched in recent years. However, the field of steerable needles has been dominated by the principle of using a beveled or pre-curved tip, or both, to create an asymmetric force at the tip of a needle and thus affecting the direction of tissue fracture as the needle is inserted [68, 46].

In the case of guide wires and sub-millimeter needle diameters, this asymmetric force is wholly dependent on the control surface in the case of bevel tips [64] or the angle, stiffness, and length of the pre-bend [2], in conjunction with the stiffness of the tissue in which the needle tip is operating. This intrinsic dependence of both needle material, needle geometry, and tissue properties to cause a resulting curvature motivates the search for a new paradigm in steerable needles.

The majority of steerable needle approaches can be classified into categories of bevel-tipped steering, pre-bend steering, duty-cycle steering, external lateral manipulation, active cannulae (primarily for traversal of open spaces), and combinations of multiple modalities [53, 12]. The bevel-tipped, pre-bend, and duty-cycle classes of steerable needles are all attempting to create an asymmetric force at the tip of the needle that will cause the tissue fracture to occur at an angle[46, 68, 47]. Of these types, duty-cycle steering is an adaptation of bevel-tipped steering where the relative rate of needle rotation to the insertion distance controls the curvature as a ratio from the zero duty cycle maximum curvature to the 100% duty cycle infinite curvature [20]. Although duty cycling provided an effective and efficient way to regulate the insertion radius of steerable needles, it could result in serious tissue damage around the needle. [60]

Recent efforts have controlled the angle of a pre-bend with a fixed distal length using either tendons [2], with application in liver ablations [23], or an externally applied magnetic field[49], with applications in deep brain stimulation. While able to achieve the best insertion radius to date among all methods of steerable needles, this approach still had the undesirable effect that any change in the angle at the tip of the needle, with the requisite forces to achieve tissue deformation, will necessarily cause large displacements in the tissue directly surrounding the tip. The magnitude of this deformation will depend on the fulcrum length of the distal portion beyond the actuated joint and the softness of the tissue. Duty-cycle methods also must account for the inherent torsional windup associated with twisting a long, super-elastic needle about the insertion axis[52, 62].

Another popular technique used for both bevel-tipped steerable needles and duty-cycle steerable needles has been to find ways to selectively reduce the bending stiffness of the steerable needle in one rotational degree of freedom. One approach has been to create notched needles that effectively reduce the bending stiffness in the plane of the notched section [29]. This is among a whole class of designs that attempt to selectively reduce the stiffness in a portion of the needle through creating thinner geometries along the length of the needle, often near the tip and sometimes with variable geometry [7, 61, 23].

The work presented in this paper is most closely related to very early steerable needle work by Okazawa *et al.*[42] where a pre-curved stylet is extended from a tube to create a controllable prebend. However, this method is still a variation of the pre-bend approach where the intent is to create an asymmetric force at the tip of the needle to try and change the direction of tissue fracture. This paper describes an alternate approach using a stylet and tube, where the stylet is extended from the tube while the tube is held fixed and then the tube follows while holding the stylet fixed. The approach results in a fundamentally different approach to steerable needles where we first control the direction of tissue fracture through the geometric design of the stylet, and simply follow the tissue fracture with the tube. In the latter portion of each step when the tube is following the channel cut by the stylet, the resultant shape of stylet, tube, and tissue channel can be computed in a manner similar to the active cannula approach to open space traversal, where the tissue channel is treated as the outermost tube. The reported lateral motion is 30mm over a 100mm insertion, which can be converted into a 325mm minimal equivalent insertion radius[71, 18].

2.3 Fracture-directed Steering Method

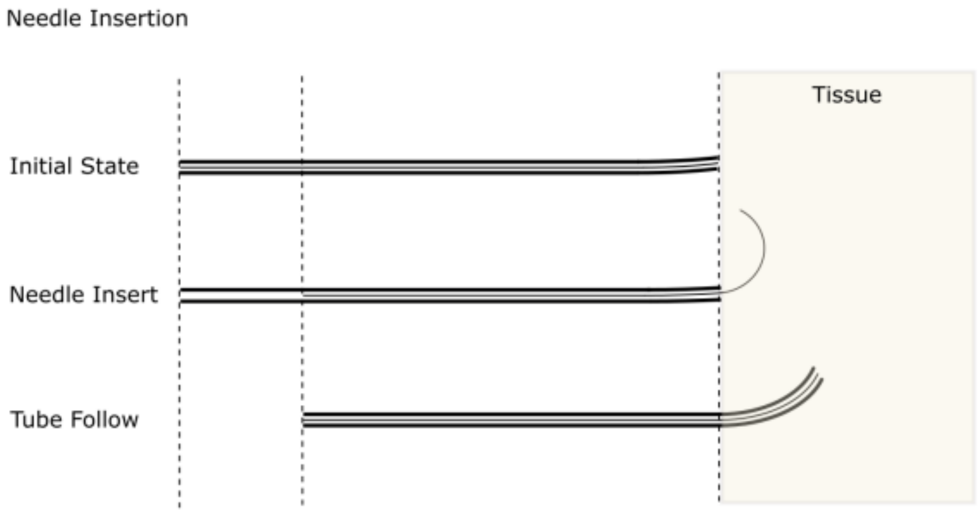

Figure 2.1: Principle of fracture-directed steering. First the inner stylet is advanced, followed by the outer tube. The shape of the tissue fracture closely matches the geometry of the inner stylet. After the outer tube follows the inner stylet, the resulting tip position depends on the static equilibrium of the wire, tube, and tissue.

Figure 2.1 describes the principles of the stylet and tube form of fracture-directed steerable needles, where an inner stylet with a predefined geometry is first extended from the tube to fracture the tissue, after which the tube follows the stylet along the fracture direction.

The proposed method of fracture-directed needle steering consists of a straight outer elastic tube and an inner elastic wire stylet. This paper explores the effects of the pre-set shape of the inner stylet and the relative extension of the stylet from the tube on the achievable curvature of the needle in multiple tissue stiffnesses. A kinematic model relating the distance the inner stylet is inserted before following with the needle is derived and a linear relationship between curvature, κ, and stylet insertion distance is presented. The achievable insertion radius is improved over existing pre-curved and bevel-tipped approaches and the low radius of curvature is demonstrated across a range of simulated tissue stiffnesses. The proposed approach is not the only feasible method of fracture-directed steerable needles, but is a fundamental deviation from existing techniques in that the objective is first to control the direction of tissue fracture and then follow the fracture with the needle. The high curvature and lessened dependence on tissue stiffness demonstrated in this paper, and the relatively small deviation in terms of experimental apparatus from existing steering methods, provide the promise that fracture-directed steerable needles could fundamentally change how needle steering is accomplished in the future.

In a single insertion, there are three different states of curvature, as shown in Figure 2.1:

1. Initial state: Before the insertion, the relatively low tube stiffness is not enough to straighten pre-curved wire completely. Some amount of curvature is evident when tube and wire are fully overlapped.
2. Stylet insertion: The stylet goes into tissue, cutting a channel based on its preset curvature.

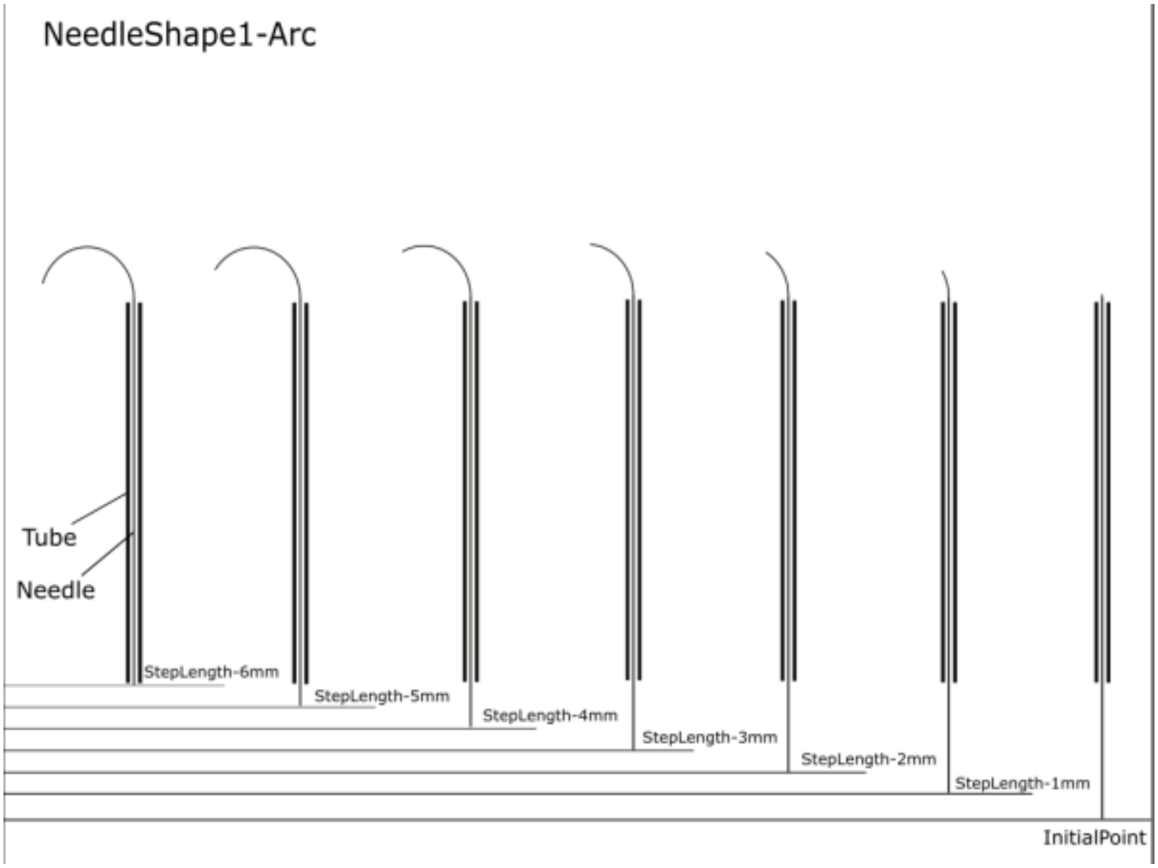

Figure 2.2: Depiction of how the stylet step length causes a longer channel to be cut in the tissue.

3. Tube follows stylet: The stiffness of tissue is insufficient to make the tube follow the exact path of the stylet, so the resultant shape is based on the stored elastic energy of the stylet, tube, and tissue. In our experiments where the tube stiffness is of the same order of magnitude as the tissue, the actual insertion curvature is less than stylet curvature.

Figure 2.3 demonstrates the insertion curvatures of different step lengths inside the tissue phantom. The needle type used here is Arc-Stylet shape.

The technique we have used for needle path tracking is based on image analysis. By fitting a curve on the top view of insertion image, the insertion curvature of each needle can be obtained. As shown in Figure 2.2, as the step length increases, the wire comes out of the tube corresponding to further distance per step, which causes the needle arc length to rise. In the case of the spiral stylet, this corresponds to a changing curvature, but in the cast of the arc and right angle stylets, a constant curvature. The needle showed in Figure 2.2 is the Arc-stylet shape.

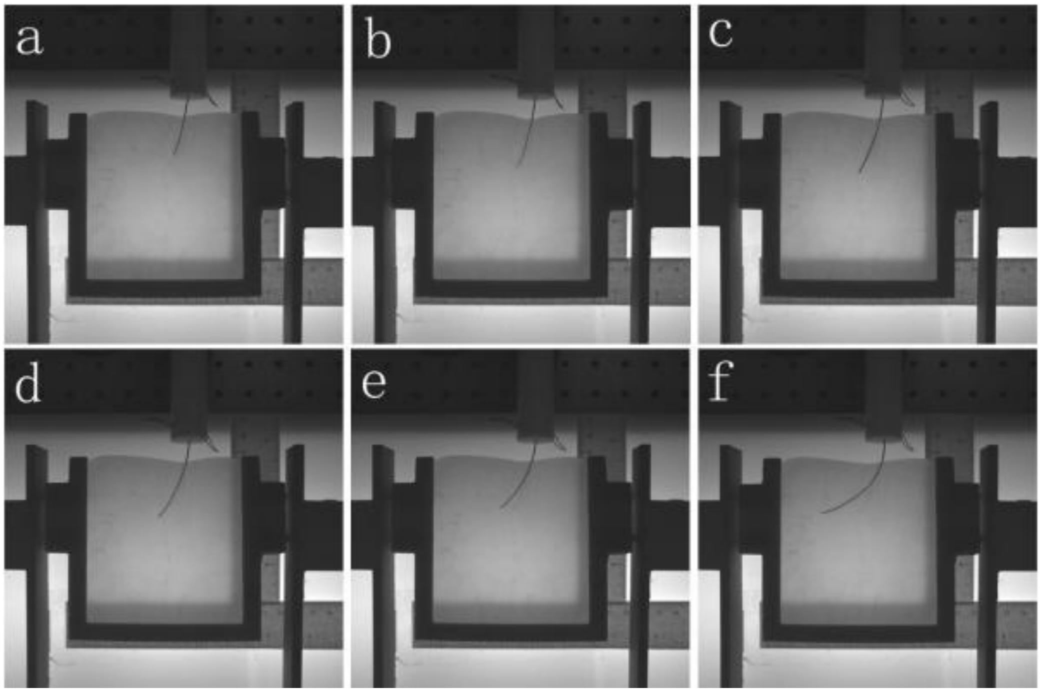

Figure 2.3: Changing the step length in the same tissue sample changes the curvature accordingly.

2.4 Materials and Methods

2.4.1 Recoverable Strain and Nitinol Stylet Heat Treatment

The stylets used in the experiment were made of superelastic nitinol. As such, computing the maximum recoverable strain is a necessary condition when determining the minimum radius of stylet curvature. To ensure that the stylet can be fully straightened without any plastic deformation, we decide to use the common conservative superelastic Nitinol strain limit of $\varepsilon = 8\%$ [71]. The relationship between

parameters	**tube**	**needle**
outer diameter(mm)	0.8	0.47
inner diameter(mm)	0.6	–
length(mm)	350	400

Table 2.1: Parameters of tube and needle for silicone compound tissue phantoms

parameters	**tube**	**needle**
outer diameter(mm)	1.45	0.25
inner diameter(mm)	0.7	–
length(mm)	200	220

Table 2.2: Parameters of tube and needle for SEBS tissue phantoms

recoverable strain limit and needle tip pre-curvature is:

$$\kappa = \frac{2\epsilon}{D(1+\epsilon)} \tag{2.3}$$

Then the calculated minimum radius of needle curve, r, is derived from

$$\kappa = 1/r. \tag{2.4}$$

For the needle used in our experiments described in Table 2.1 and Table 2.2, the minimum radius of 0.47mm diameter stylet without plastic deformation is 3.1718mm, and the minimum radius of 0.25mm diameter stylet without plastic deformation is 1.7145mm.

To achieve a balanced bending stiffness relationship among tissue, stylet and tissue phantom, the tube in Table 2.2 was 3D printed with SemiFlex, a material with 25Mpa

Young's Modulus that dropped 3 folds in comparison to the Young's Modulus of the Nitinol tube, 40Gpa.

To fabricate the optimal shape for each Nitinol stylet geometry, straight Nitinol pieces are pressed in an aluminum mold, heated to 500°C for 30 minutes, then quenched with water. Figure 2.4 shows the three stylet geometries after heat treatment that are used during experimentation.

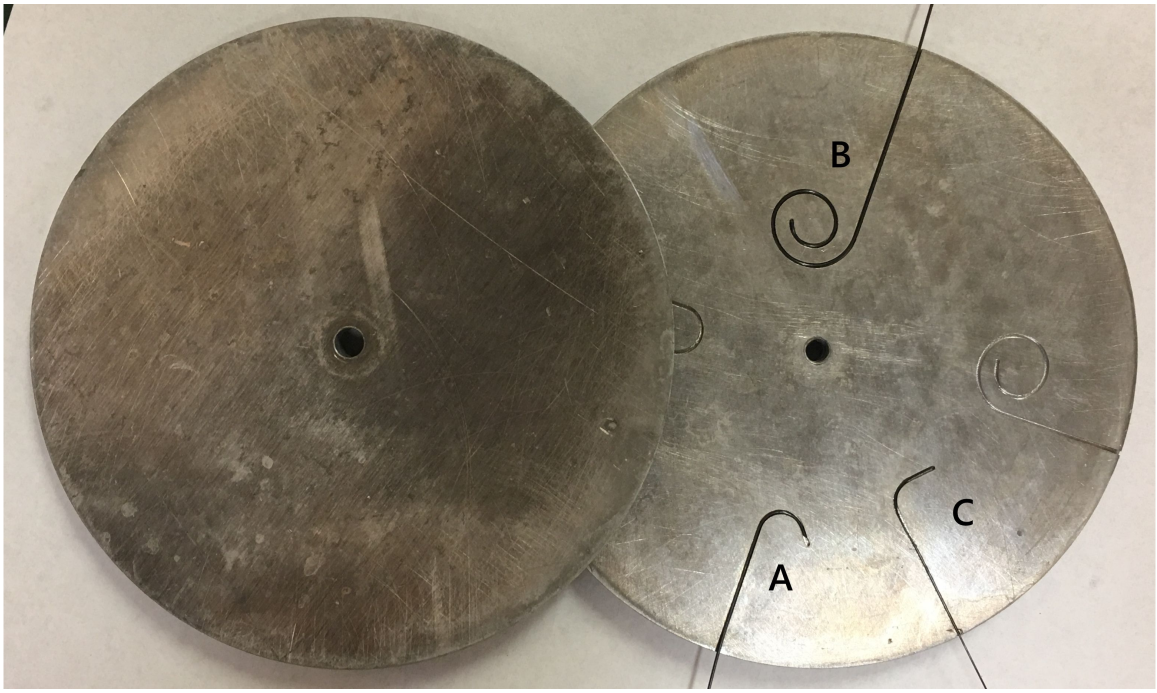

Figure 2.4: Three different needle shapes (A) Arc-stylet (B) Spiral-stylet (C) Right Angle-stylet

2.4.2 Tissue Preparation

Two types of tissues are used for our experiments. The first category is Silicone Compound tissues consisting of Shore 10 Fast, Shore 10 Medium, Shore 20 Medium and Shore 00-50. Shore 00-50 is Platinum-Catalyzed Silicone. Except for Shore 00-50, all elastomers are High-Performance Platinum Cure Liquid Silicone compounds. Shore 20 Medium has the highest Shore A Hardness Scale 20A, Shore 10F and Shore 10M have the same Shore A Hardness, 10A, and Shore 00-50 have the lowest hardness, 00-50. In our experiments, both 10F and 20M are mixed with 20% mineral oil by weight to reduce stiffness and friction during insertion. The 10M and 00-50 are mixed with 10% mineral oil by weight. The Tensile Strength is between 315psi to 550psi, with shrinkage less than 0.001 inches [58, 59]. To estimate Young's modulus of tissues, durometer scale A and durometer scale 00 were developed by Larson et al. [45, 50]. In our experiments, Young's modulus of shore 00-50 can be estimated as:

$$E = (0.0037)e^{(0.0718)S} \tag{2.5}$$

where E is Young's modulus in MPa and S is nominal Shore 00 durometer hardness; Young's modulus of shore 10 Fast, Shore 10 Medium and Shore 20 Medium can be estimated as:

$$E = (0.4863)e^{(0.0345)S} \tag{2.6}$$

Tissue	**Approximate Young's modulus(kPa)**	**Shore hardness**
15%SEBS	68.0	
20%SEBS	128.0	
00-50	134.0	00-50
10 Fast	687.0	10A
10 Medium	687.0	10A
20 Medium	970.0	20A

Table 2.3: Young's modulus and Shore hardness of tissue phantoms

where E is Young's modulus in MPa and S is nominal Shore A durometer hardness. Both Young's modulus and the Shore hardness of tissue phantoms are shown in the Table 2.3. Poly (styrene-b-ethylene-co-butylene-b-styrene) triblock copolymer (SEBS) produced by Kraton Polymers LLC (G1652, Houston, TX, USA) is used as the base material for the second group of tissues used in our experiments. The density of this material is $\rho_{SEBS} = 910\frac{kg}{m^3}$. Mineral oil is used as the solvent for this material. According to R.A. Mrozek *et al.* [40], the stiffness of the tissue is not dependent on the supplier of the mineral oil. The authors used light mineral oil with density $\rho_{oil} = 0.85\frac{g}{mL}$.

SEBS material and mineral oil are weighed out to produce mixtures containing 15, and 20vol% SEBS. The mixture was then put into the oven at 120^oC for 8 hours (for mixtures containing a lower amount of SEBS this time is lower) and was mixed occasionally to produce a homogeneous solution without any visible undissolved powder. The solution is then poured into the mold of rectangular shape with dimensions $100 \times 100 \times 50\,mm$ and let to cool down in room temperature before removing from the mold. In order for the tissue to come off easily, universal mold remover was used.

From the log-log plot of Young's modulus vs. polymer fraction provided in R.A. Mrozek *et al.* [40] we found that there is a power-law relationship between the Young's modulus and the polymer fraction as follows:

$$\text{Young's} \quad \text{modulus} = c(\text{Polymer} \quad \text{fraction})^m \tag{2.7}$$

With $m = 2.2234$ and $c = 4.6018 \times 10^6$. In this equation, the polymer fraction is in percents and the Young's modulus is calculated in Pascals (Pa). Therefore, the elastic moduli for 15% and 20% SEBS are $\approx 68kPa$ and $128kPa$, respectively that are also relevant to stiffness of biological tissues within human body [73]. These values are consistent with the values reported in the paper and that the power-law can be extended to find the Young's modulus of tissues with SEBS concentration less than 20%. It's also worth mentioning that the authors examined samples of cylindrical soft gels with diameter of $25\,mm$ and thickness of $2\,mm$ using a rheometer to verify the results presented in R.A. Mrozek *et al.* [40]. Rheological tests are done at 25^oC (because in a region with center at 20^oC, the modulus shows less sensitivity to temperature [40] and needle insertion experiments are usually performed in room temperature) with $1Hz$ frequency and strain range is within $0.01\% \sim 5\%$ to ensure linear viscoelastic response of these gels. The shear modulus obtained from the rheometer is converted to Young's modulus (E) considering Poisson's ratio of $\nu \approx 0.5$

for an incompressible solid and using the equation $E = 2G(1 + \nu)$ where G is the shear modulus obtained from rheology experiments.

2.5 Design of Devices and Experiments

2.5.1 Design considerations

This subsection described a robotic solution that enables coordinated simultaneous motions of two input degrees of freedom. The insertion system was designed to drive the needle in one translational motion along the needle shaft and one rotational motion about the needle shaft. Actuators control the speed of insertion and rotation, l and θ directly for an insertion radius r. A simultaneous rotation mechanism was implemented to address the rotation lag caused by the friction between needle and tissue phantom. Collets were installed concentric and coaxial on both tube and wire platforms to enhance the grip of nitinol materials and avoid buckling. Limit switches were applied to prevent the over retraction or insertion of the inner nitinol wire so the actual step length can accurately fall under the range of insertion radius predictive model.

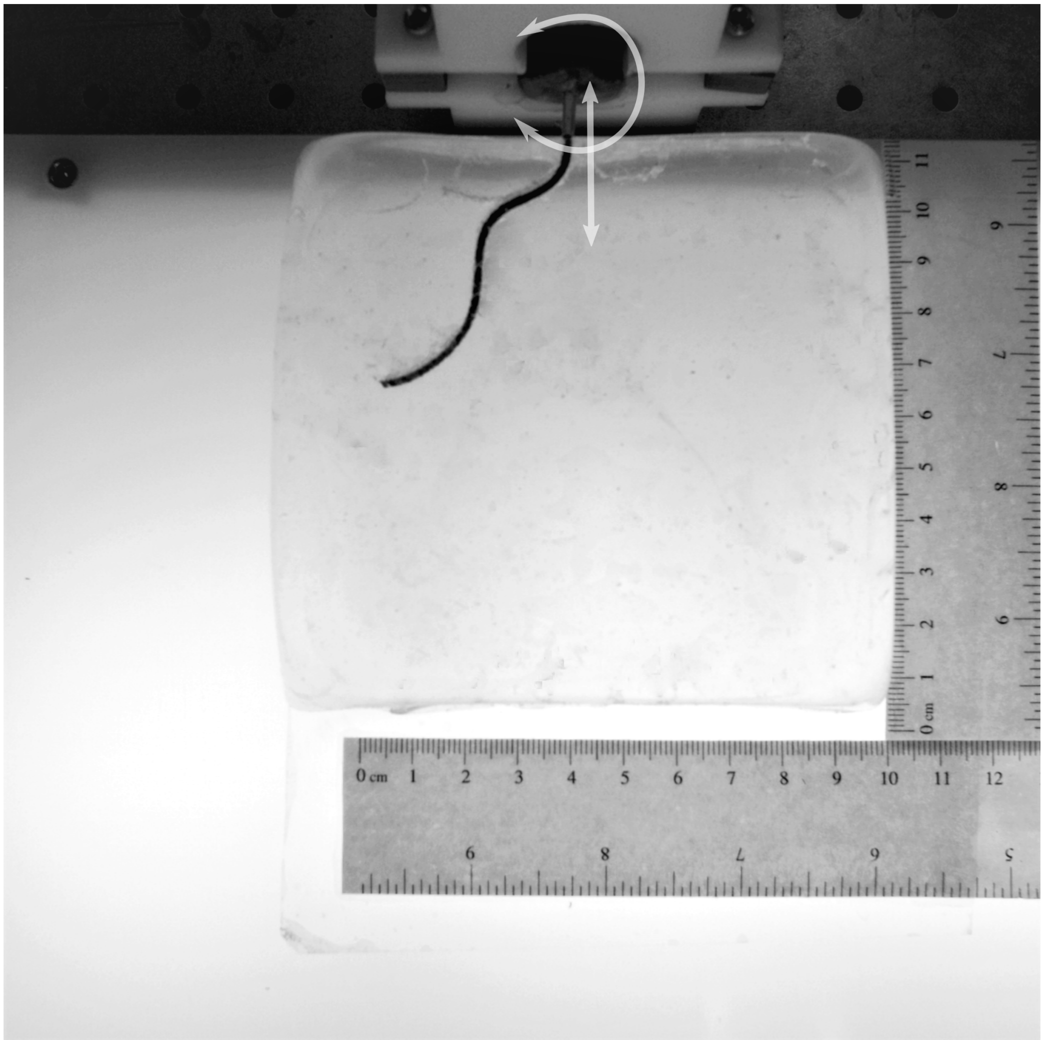

Figure 2.5: The needle has one translational degree of freedom along the needle shaft and one rotational degree of freedom about the needle shaft as shown in shallow white mark in the figure.

2.5.2 Device for Needle Insertion

To achieve high steerability inside tissues, there are three separate motions needed. First, the stylet with predefined geometry and the tube that encases the stylet must be able to be moved relative to each other. Second, the stylet and tube need to be rotated simultaneously. Through these two motions, steerability in 6 degrees of freedom can be achieved. To accomplish this, the main part of the needle insertion system consists of two linear slides and one rotational servo motor. Other components, including limit switches, collets and bearings, are connected to the main structure by 3D printed parts and traditional fasteners. The linear slide and servo motor are controlled by micro-step drivers to achieve accurate linear motion and the rotational servo achieves accurate rotational motion through internal feedback. The control of the needle insertion device is accomplished through firmware running on a chipKit uC32 microcontroller (Digilent Inc., Pullman, WA, USA), which accepts simple linear and rotational velocity commands from a PC running control scripts in the Python environment. The microcontroller is continually monitoring the status of the limit switches to ensure no portion of the system is driven past its physical limits.

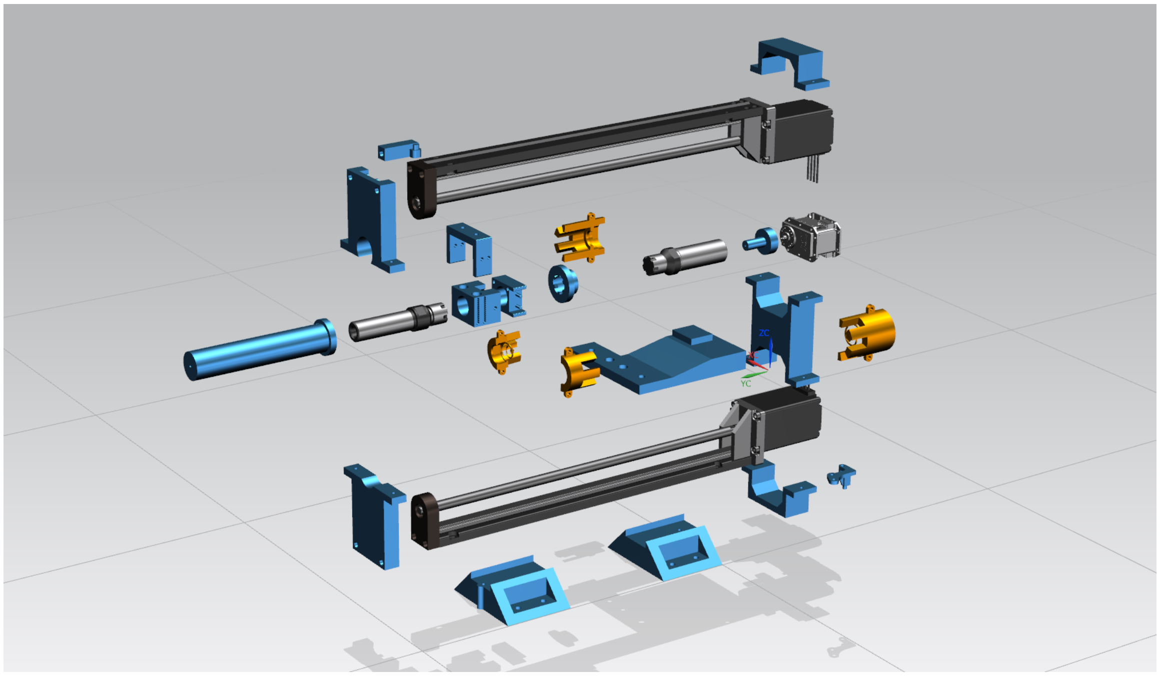

Figure 2.6: Exploded-view drawing of the CAD model for main structure of the needle insertion system.

Figure 2.6 presents the main structure of the needle insertion system. The design was conducted in Siemens Unigraphics NX environment(Siemens Corporation, Washington, D.C., United States).

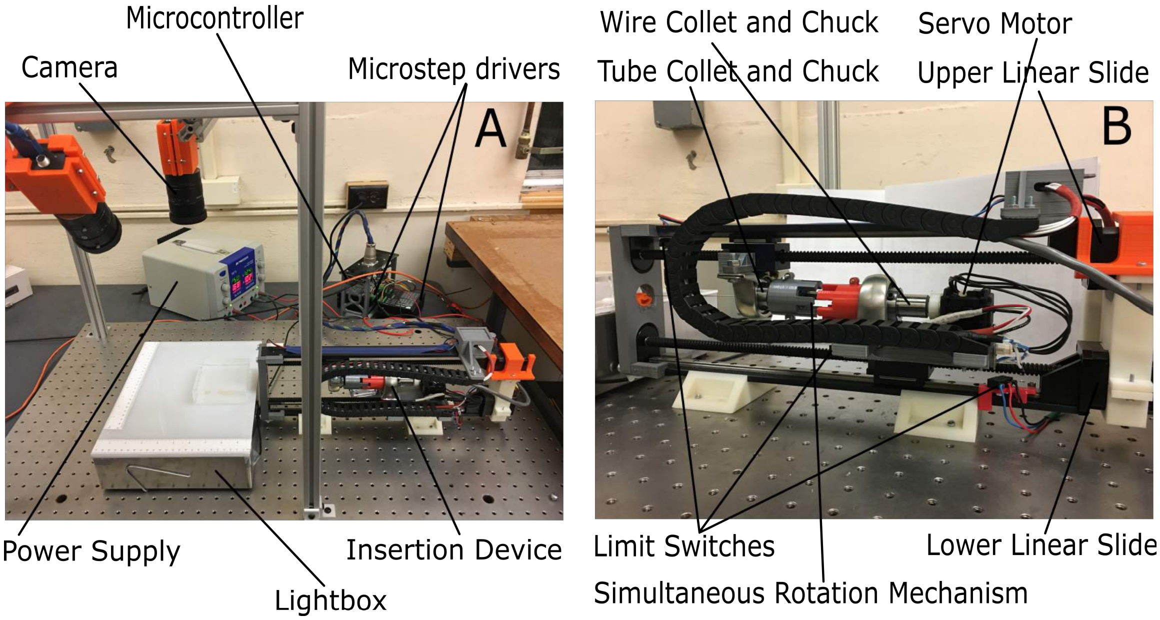

Figure 2.7: (A) The whole needle insertion system setup, including the insertion device, two micro step drives for linear slides, a light box, a camera, a microcontroller, and a power supply. (B) Insertion device setup, including three limit switches, simultaneous rotation mechanism, tube and wire collets and chucks, two linear slides and two bearings.

Figure 2.7-A shows the overall system with the insertion device, overhead camera capture, a lightbox for transparent tissue simulant , and the associated electronics. Figure 2.7-B depicts the assembly of the insertion system, with each critical component labeled. Each collet and bearing was mounted on the opposing linear slides, such that the bores of the collets are collinear. The tube collet is located distally, closest

to the insertion point, and the wire collet is located proximally, such that the wire can be pushed out of the tube. Three limit switches are located at the most distal limit of travel, the most proximal limit of travel, and between the wire and tube stages.

2.5.3 Design of Experiments

The experiments were aimed at two major objectives. The first objective is to discover the change of resultant insertion radius caused by altering the shape of needle tip. The second objective is to derive the relationship between the resultant insertion radius and various step length. As such, we first determine the allowable geometries of the Nitinol stylets that would result in strains that remain below the point of plastic deformation for both the stylets and the tubes when in the completely overlapped configuration. We have also developed transparent tissue phantoms that span a certain range of simulated tissue stiffnesses to evaluate the effectiveness of the approach using different needles inserted into multiple tissue stiffnesses. Three different needle tip shapes were evaluated in experiments with various step length from 1 millimeter to 6 millimeters.

A complete needle insertion system with the insertion device, overhead camera capture, a lightbox for transparent tissue simulant , and the associated electronics can be seen in Figure 2.7-A

Figure 2.7-B depicts the assembly of the insertion system, with each critical com-

ponent labeled. Each collet and bearing was mounted on the opposing linear slides, such that the bores of the collets are collinear. The tube collet is located distally, closest to the insertion point, and the wire collet is located proximally, such that the wire can be pushed out of the tube. Three limit switches are located at the most distal limit of travel, the most proximal limit of travel, and between the wire and tube stages.

A typical insertion progress using "stop & rotate" strategy consists of the following steps:

1. The wire platform moves backward until retreat limit switch activated. The tube collet follows needle platform to move back until inter-stage limit switch activated.
2. Send a step length for moving forward motion, the wire collet moves first, then the tube platform follows it.
3. Send a rotation angle, if necessary, to the servo motor to rotate the tube and wire.
4. Repeat Step 2 and Step 3 until the needle tip reaches the desired position.

2.6 Discrete Model for Fracture-directed Steerable Needles in Two-dimensional Space

The bicycle model is the most common model used to describe the motion of bevel-tipped and pre-bent steerable needles[72, 68, 46]. It generally prescribes the motion of the steerable needle in terms of a fixed rate of angular rotation in a plane as a function of insertion velocity and the ability to re-orient the plane in which the needle is traveling by twisting the needle at the base.

Here, we present a discrete analogue of the bicycle model for the proposed method of fracture-directed needles. In this model, the independent variable is now the step length of the stylet before following with the tube. Consider a pre-curved stylet that is driven by step length from the end of the tube. As the stylet exits the tube and enters the tissue, the stylet will nominally follow the pre-defined shape of the stylet. The step length is modeled as the input to the system. In the following subsection, mathematical preliminaries to propose a suitable model will be investigated. Then, a model based on Lie groups and Lie algebra will be proposed and finally the simulation results indicating the relationship between the curvature and step length will be given. The model for the curvature as a function of step length is derived from the experimental results presented in Figure 2.10. In this section a mathematical model is developed for position of needle tip with respect to the base frame as a function of the step lengths. Figure 2.8 shows the three distinct stages of needle insertion into the tissue.

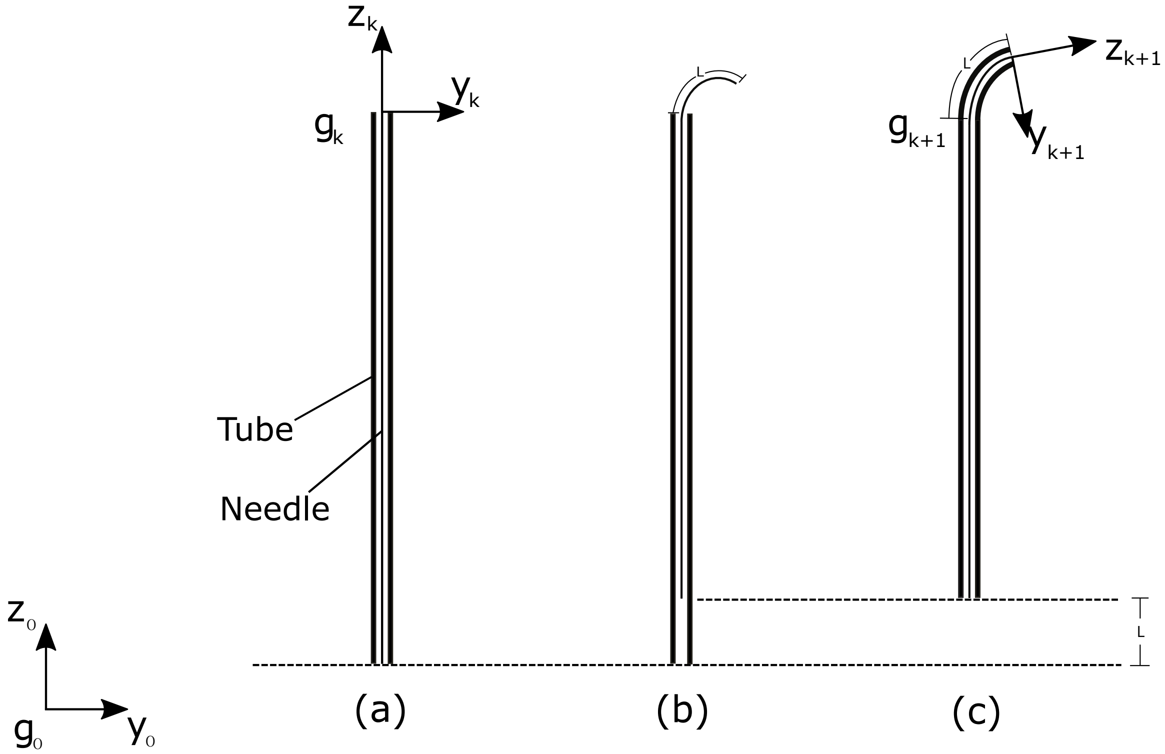

Figure 2.8: position and orientation of needle tip in 2-D

First, the stylet is extended out of the tube, after which the tube follows the stylet. The z-axis of the body fixed frame is the direction of insertion. The arc length of each step is parameterized by l, in millimeters.

In order to find the position and orientation of needle with respect to the base frame, a model is developed for the relationship between the curvature, κ, the step length, l, and the rigid body motion between the body fixed frames, g_k and g_{k+1}, before and after the completed step, as shown in Figure 2.8(a),(c). The twist coordinates of the system are defined as follows:

$$\xi(l) = \begin{bmatrix} \omega \\ v \end{bmatrix} = \begin{bmatrix} \kappa(l) \\ 0 \\ 0 \\ 0 \\ 0 \\ 1 \end{bmatrix} \tag{2.8}$$

The twist describes the discrete-step needle motion and is a function of l, which is the length of the needle that is inserted before the tube follows.

By inspection of the vector field defined by the twist, the needle system has rotation around the body-fixed x-axis and linear translation along the z-axis. Using the matrix exponential of the twist describing the motion in each discrete step of the stylet and tube, the pose of the needle after a step can be calculated as the product of matrix exponential of the twist and the previous pose,

$$g_{k+1} = g_k e^{\hat{\xi}_k l} \tag{2.9}$$

The discrete-step position/ orientation change is only a function of the length of the needle that is inserted before the tube follows. The matrix $g_k \in SE(3)$ is the tube tip position/orientation before the needle is inserted and $g_{k+1} \in SE(3)$ is the tube tip position/orientation after the needle has been inserted and the tube has followed. This model can be used, based on experimentally determined curvature as a function of step length, $\kappa(l)$, to simulate needle insertions for any number of steps and for any step length along the way. In this section, simulation results demonstrating the change of needle insertion radius are investigated. With this simulation, the insertion radius with long step length can be predicted disregard the restriction of tissue phantom szie.

Use arc shape stylet in Shore 10M tissue simulant as an example, the values of radius for different values of step lengths are shown in Table **??**.

step length(mm)	**radius(mm)**
1	136.09
2	98.13
3	88.79
4	70.48
5	65.70
6	48.25

Table 2.4: Arc-stylet insertion radius for different values of step lengths

Curve fitting using MATLAB (The MathWorks, Inc., Natick, Massachusetts, United States) showed that the relationship between radius and step length can be approximated by a line with the following equation

$$\kappa = 0.002l + 0.0057 \tag{2.10}$$

2.7 Resultant curvature based on step length

Figure 2.9 depicts the radius change as a linear function of needle insertion radius for different step lengths. This linear relationship between the insertion radius and the step length allows precise prediction of the insertion radius across insertions with larger step lengths.

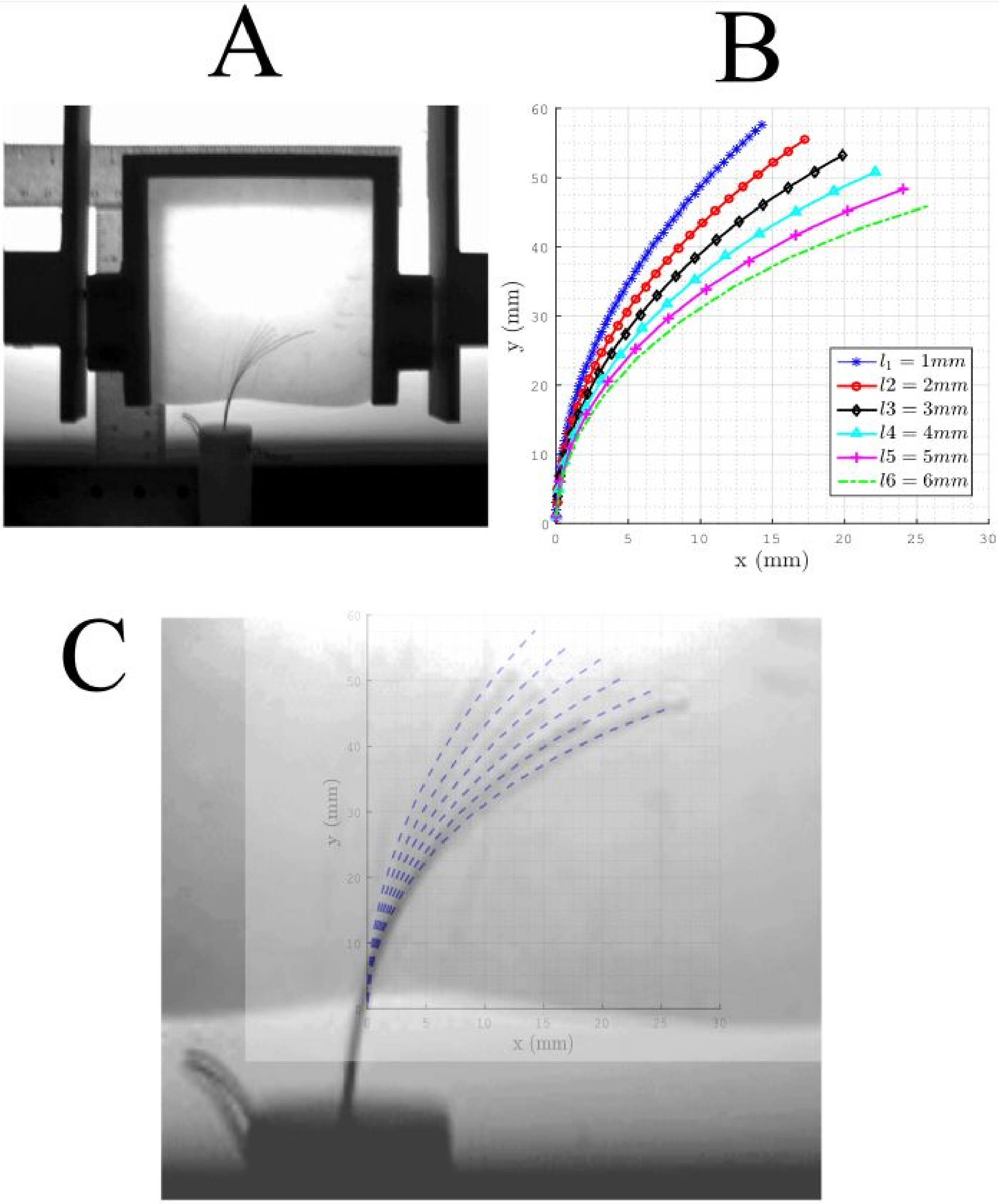

Figure 2.9: (A) An overlay of multiple real trials with differing step lengths, demonstrating the curvature increase as the step length increases. (B) The model based on real experiments, provide the capability of predicting insertion radius with large step lengths. (C) An overlay of experimental insertion radii (black continuous curves) and model generating insertion radii (blue dashed curves), which shows the reliability of the model.

parameters	**tube**	**needle**
outer diameter(mm)	0.8	0.47
inner diameter(mm)	0.6	–
length(mm)	350	400

Table 2.5: Parameters of tube and needle for silicone compound tissue phantoms

parameters	**tube**	**needle**
outer diameter(mm)	1.45	0.25
inner diameter(mm)	0.7	–
length(mm)	200	220

Table 2.6: Parameters of tube and needle for SEBS tissue phantoms

2.8 Resultant Insertion Curvature Based on Tissue and Needle Properties

2.8.1 Proposed Method and Experiments

This tissue and needle properties based model describes the resultant insertion radius and equivalent bending stiffness change based on variety of tissue channel radii and tissue's Young's Modulus. The equations related to the bending stiffness and curvature for calculating multiple overlapped curved tubes has been developed by Webster *et. al.*[71]:

$$\kappa_C = \frac{\sum_{i=1}^{n} E_i I_i \kappa_i}{\sum_{i=1}^{n} E_i I_i} = \frac{K_t\kappa_t + K_b\kappa_b + K_w\kappa_w}{K_t + K_b + K_w} \tag{2.11}$$

where κ_C is the combined curvature where the tube and wire are fully overlapped, and κ_t, κ_b, κ_w and K_t, K_b, K_w are the curvature and bending stiffness of the tissue

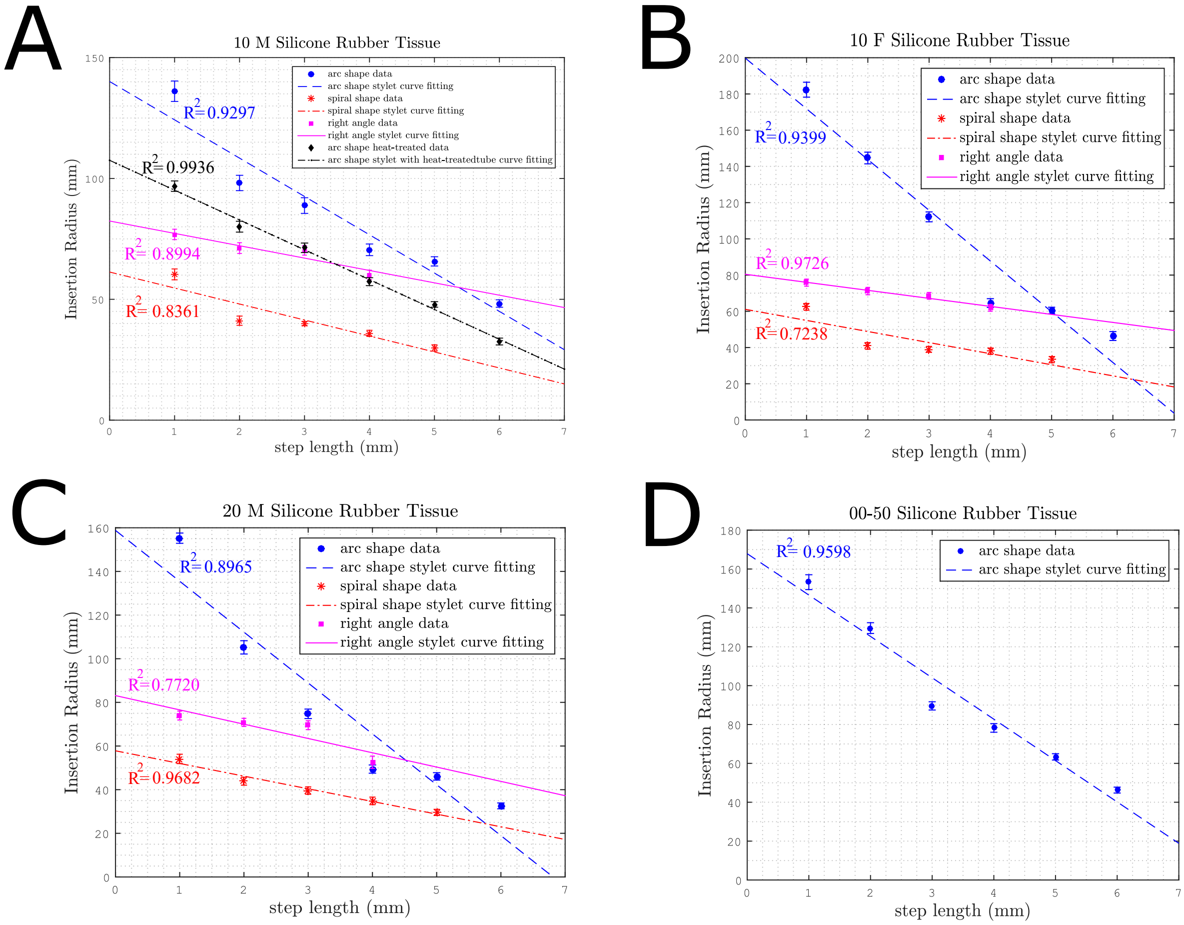

Figure 2.10: Radius as a function of step length in different silicone compound tissue phantoms. The bars on the data points are Standard Deviation of the data. Ten experiments are done for each step length and the average of the data are calculated to minimize error. The curve fitting and R-squared value indicates the relatively linear relationship between the step length and the radius. Young's Modulus of each tissue can be found in Table 2.3. (A) Curvature as a function of step length in 10M tissue phantom. The heat-treated Arc-shape stylet has a lower radius than non-heat-treated one because of the decrease in bending stiffness caused by heat treatment. (B) Relationship between radius and step length in 10F tissue phantom. (C) Curvature as a function of step length in 20M tissue phantom. (D) Curvature as a function of step length in 00-50 tissue phantom

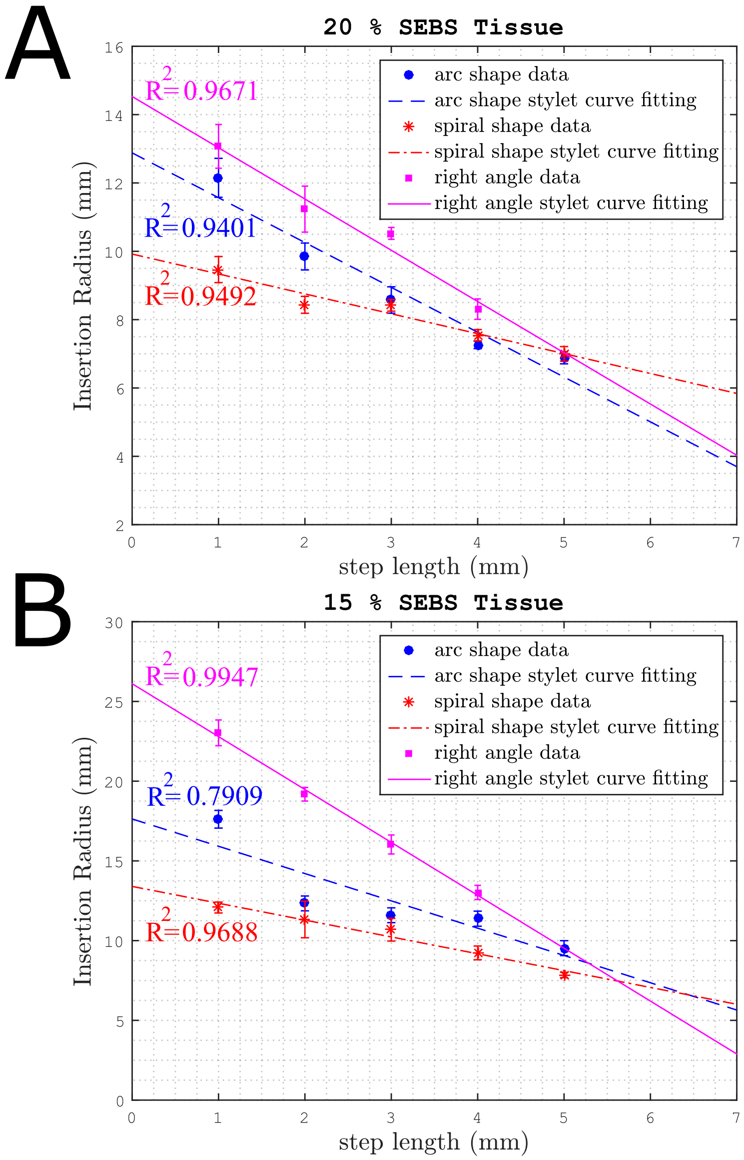

Figure 2.11: Curvature as a function of step length in two different SEBS tissue phantoms. The error bars show the standard deviation. The curve fitting and R-squared value indicate the relatively linear relationship between step length and curvature. The tube and stylet used with SEBS tissues are different from previous type used with silicone compound tissue. The parameters of stylets and tubes can be found in Table 2.1 and Table 2.2. (A) Curvature as a function of step length in 20% SEBS tissue phantom. (B) Curvature as a function of step length in 15% SEBS tissue phantom.

channel, tube, and wire, respectively. I_i is the cross-sectional moment of inertia and E is the Young's Modulus.

$$K_i = E_i I_i \tag{2.12}$$

The product of the Young's Modulus (Modulus of Elasticity) and cross-sectional moment of inertia is bending stiffness. Here is where we make the assumption and treat the tissue channel as an outer tube. Because of the relatively small strains of the tissue using the relative stiffness heuristic, this simplifying assumption is valid.

By switching K_t to the left side, we can obtain equation below from equation(2.11):

$$K_t = \frac{K_b\kappa_b - K_b\kappa_C + K_w\kappa_w - K_w\kappa_C}{\kappa_C - \kappa_t} \tag{2.13}$$

Since the Nitinol tubes we used in the experiment are straight and the tissue channel holds the same curvature as the wire, κ_b=0, κ_t=κ_w.

Thus, equation(4.3) can be written as:

$$K_t = \frac{-K_b\kappa_C + K_w\kappa_w - K_w\kappa_C}{\kappa_C - \kappa_w} \tag{2.14}$$

The approach we used for path tracking is based on image analysis. By fitting curve to the captured image via MATLAB (The MathWorks, Inc., Natick, Massachusetts, United States), the insertion curvature of each tube can be obtained.

Figure 2.12 depicts the stress-strain curve of the soft tissue simulants. The Young's

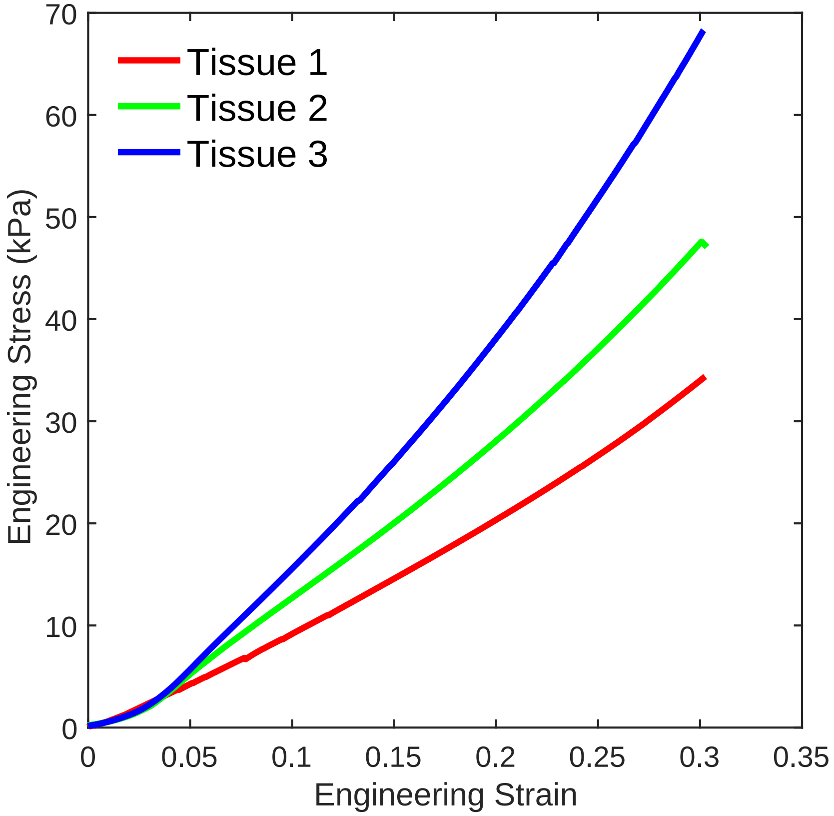

Figure 2.12: Stress vs. strain curve of SEBS soft tissue simulants. The Young's modulus of each tissue is obtained by finding the slope of the linear section of the curves. Tissue 1, 2, and 3 are 15%, 20%, and 25% G1650 SEBS in mineral oil soft tissue simulants, respectively.

modulus is obtained from finding the slope of the linear section of the curve, and the Young's Moduli of Tissue 1, 2, and 3 are 112.89, 159.80, and 229.57 kPa, respectively. The properties of the soft tissue simulants used in the experiments are provided in Table 2.7. The Young's Modulus of this type of SEBS(G1650) tissue [39] is different from the previous SEBS(G1652) that used in step length insertion curvature experiment [75].

Surface plots of equivalent bending stiffnesses generated from experimental data are provided in Fig. 2.13. Since equivalent bending stiffness is directly derived from the resultant radius of curvature, these two groups of plots hold high similarity and the equivalent bending stiffness computed from experimental data is marginally higher than FEA in the same type of tissue phantom.

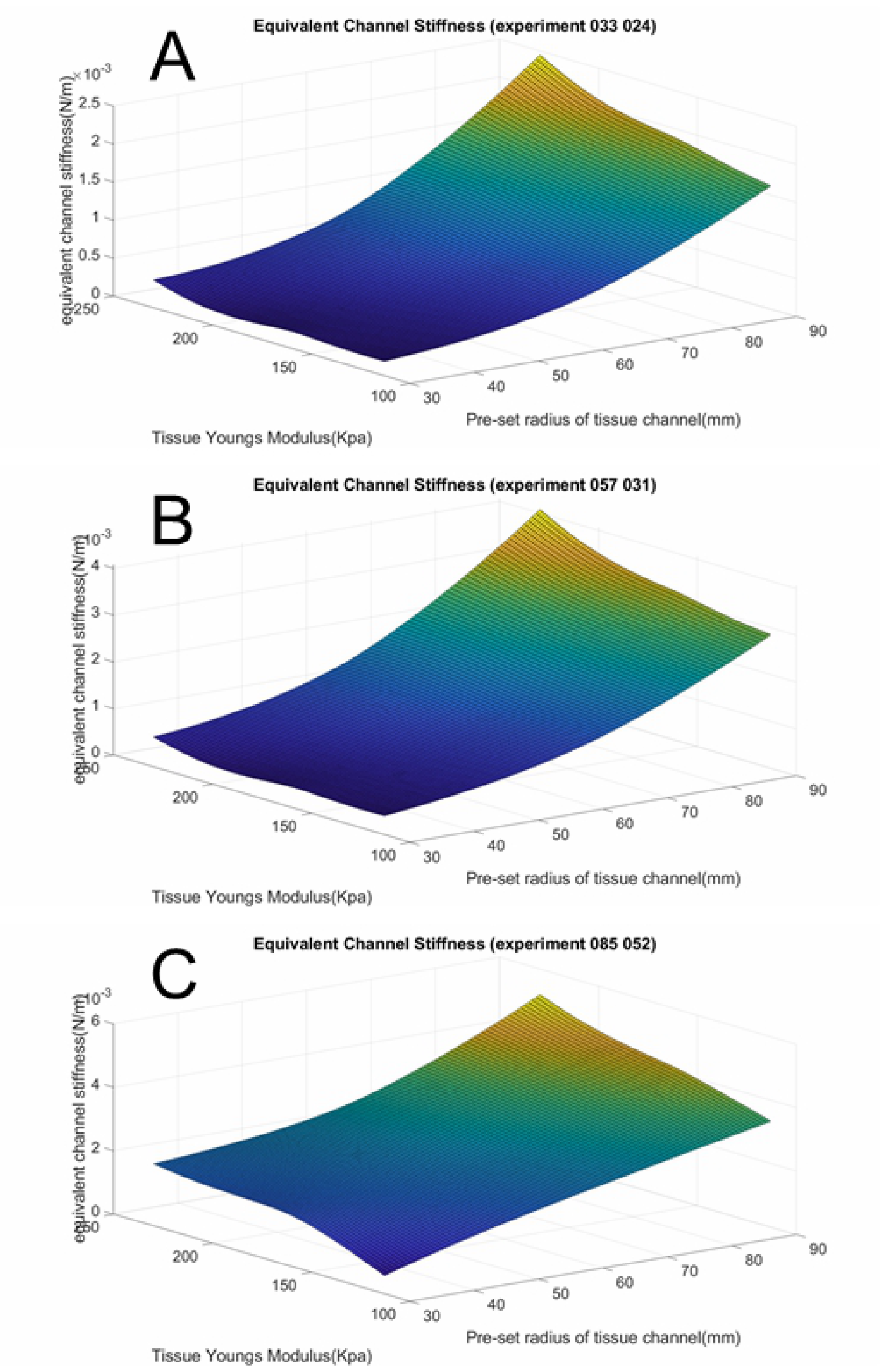

Figure 2.13: The equivalent bending stiffness surfaces in experiments with different tissue phantoms and varying channel radii. (A) The equivalent bending stiffness of tissue channel created by 0.1905mm wire and 0.26mm ID 0.33mm OD tube in experiments. (B) The equivalent bending stiffness of tissue channel created by 0.2921mm wire and 0.3175mm ID 0.5715mm OD tube in experiments. (C) The equivalent bending stiffness of tissue channel created by 0.47mm wire and 0.52mm ID 0.85mm OD tube in experiments.

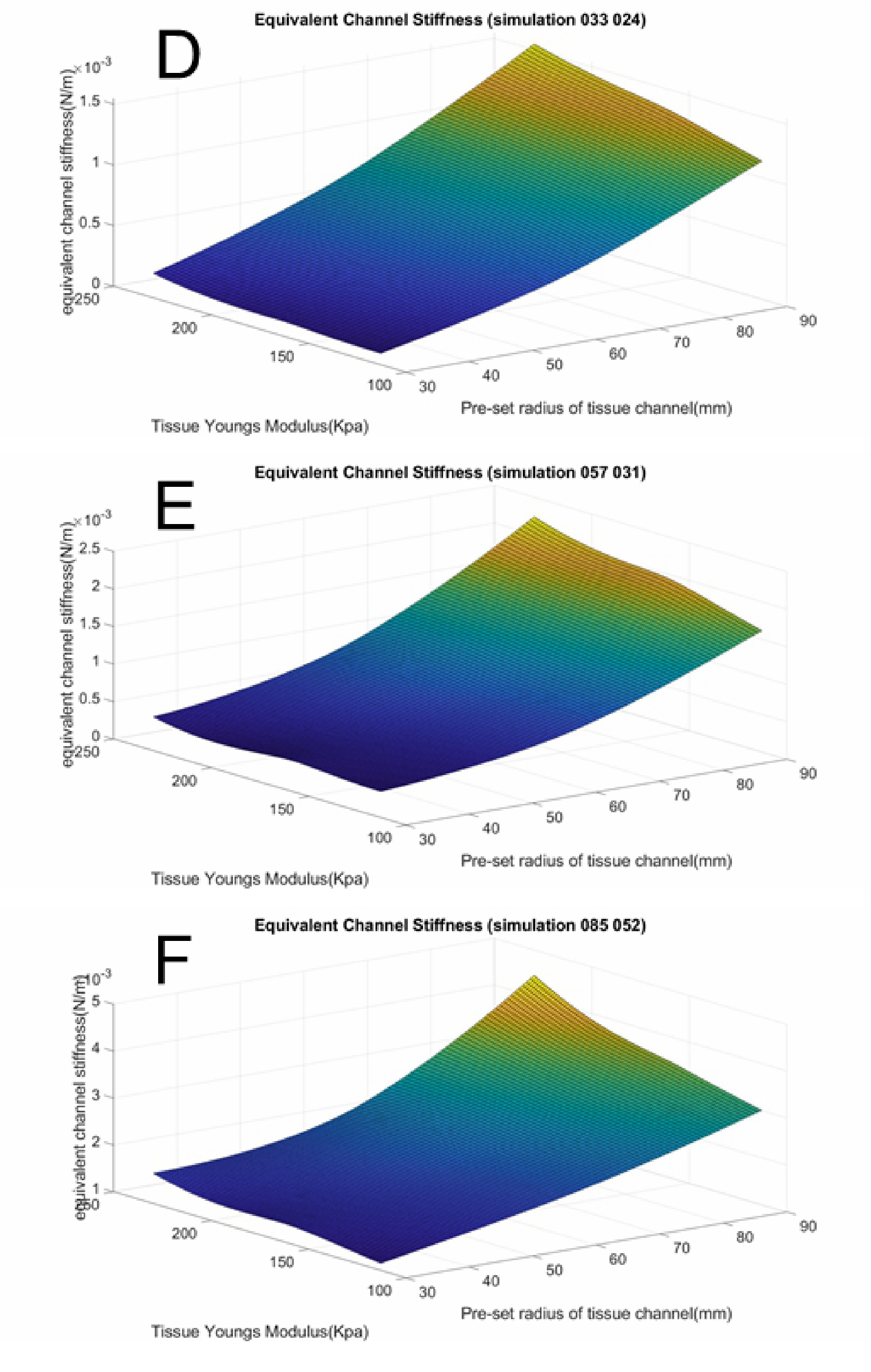

Figure 2.14: The equivalent bending stiffness surfaces in FEA with different tissue phantoms and varying channel radii. (D) The equivalent bending stiffness of tissue channel created by 0.1905mm wire and 0.26mm ID 0.33mm OD tube in FEA. (E) The equivalent bending stiffness of tissue channel created by 0.2921mm wire and 0.3175mm ID 0.5715mm OD tube in FEA. (F) The equivalent bending stiffness of tissue channel created by 0.47mm wire and 0.52mm ID 0.85mm OD tube in FEA.

Table 2.7: Mechanical properties of SEBS tissue phantoms. Tissues 1, 2, and 3 are 15%, 20%, and 25% G1650 SEBS in mineral oil soft tissue phantoms, respectively.

Tissue Phantom	**Density** ($\frac{g}{cm^3}$)	**Young's Modulus (kPa)**	**Poisson's ratio**
Tissue 1	0.85	112.9	0.49
Tissue 2	0.862	159.8	0.49
Tissue 3	0.865	229.57	0.49

As it is shown in Figure 2.13 and 2.14, the equivalent bending stiffness of tissue is not only dependent on the bending stiffness of the wire and tube being inserted, but also affected by pre-set channel radius of curvature. In other words, the equivalent bending stiffness of the tissue channel is dependent on the Young's Modulus and cross-sectional moment of inertia of the wire and tube as well as the pre-set wire radius of curvature (during insertion, the tissue channel is always created by the pre-curved wire, so their radii of curvature remain the same). Thus, tissue channel equivalent bending stiffness is a variable that reacts to the inserted stylet, it will increase as the bending stiffness of the stylet increases.

The resultant radius of curvature describes the combined radii of curvature of a pre-curved wire, a straight tube and a curved channel in the tissue phantom. The resultant radius of curvature depends on the bending stiffnesses of the wire, tube, and tissue channel. Three-dimensional surfaces were fit on both FEA data and experimental data.

In experiments, the insertion of 0.85mm diameter tube exceeded the tolerance of the tissue channel in Tissue 1 for 30mm radius channel. It couldn't follow the inner

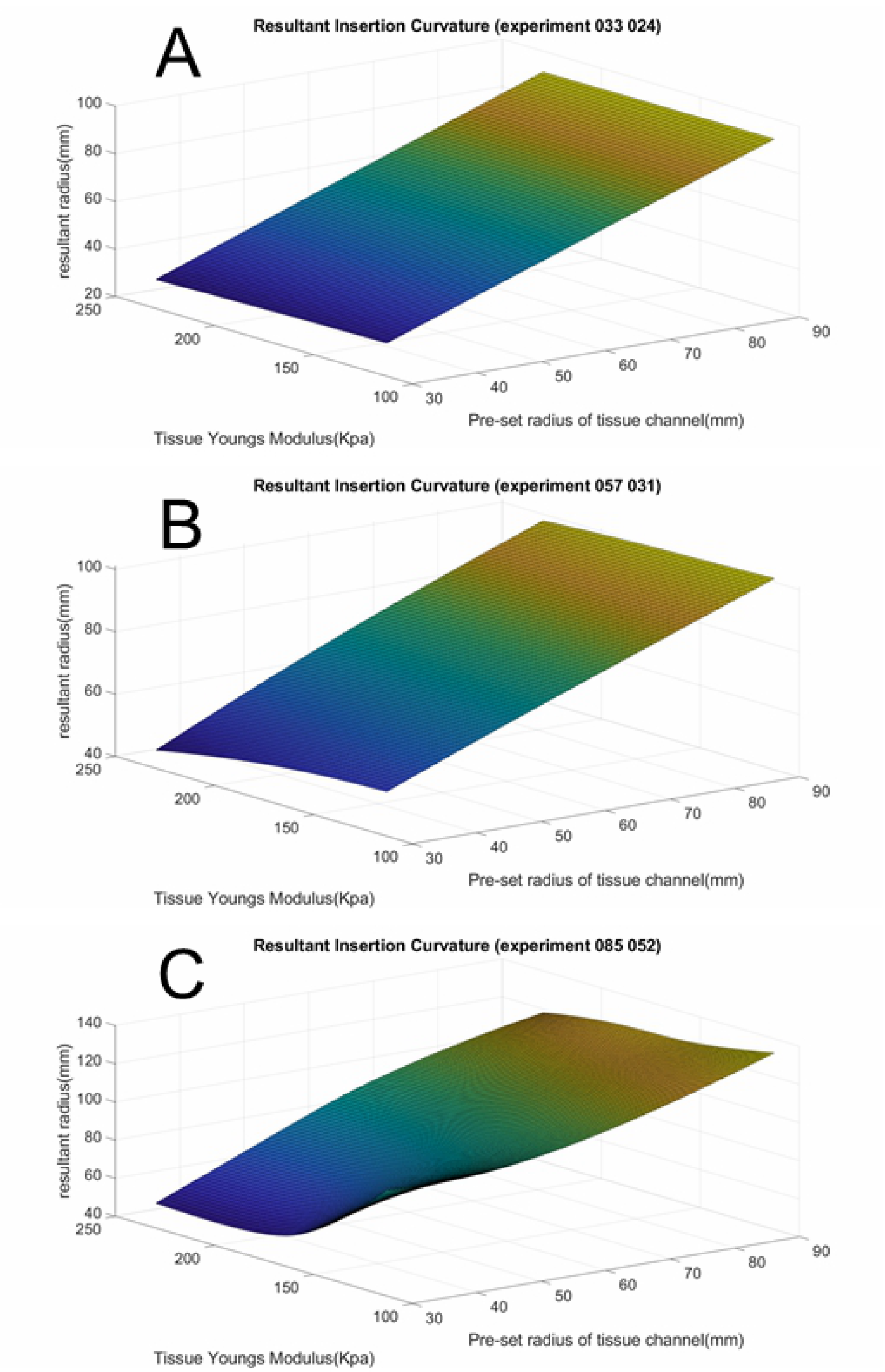

Figure 2.15: Resultant radii of curvature surfaces in experiments and FEA with different tissue phantoms and varying channel radii. (A) 0.33mm OD, 0.26mm ID tube, and 0.19mm wire in experiments. (B) 0.57mm OD, 0.32mm ID tube, and 0.29mm wire in experiments. (C) 0.85mm OD, 0.52mm ID tube, and 0.47mm wire in experiments.

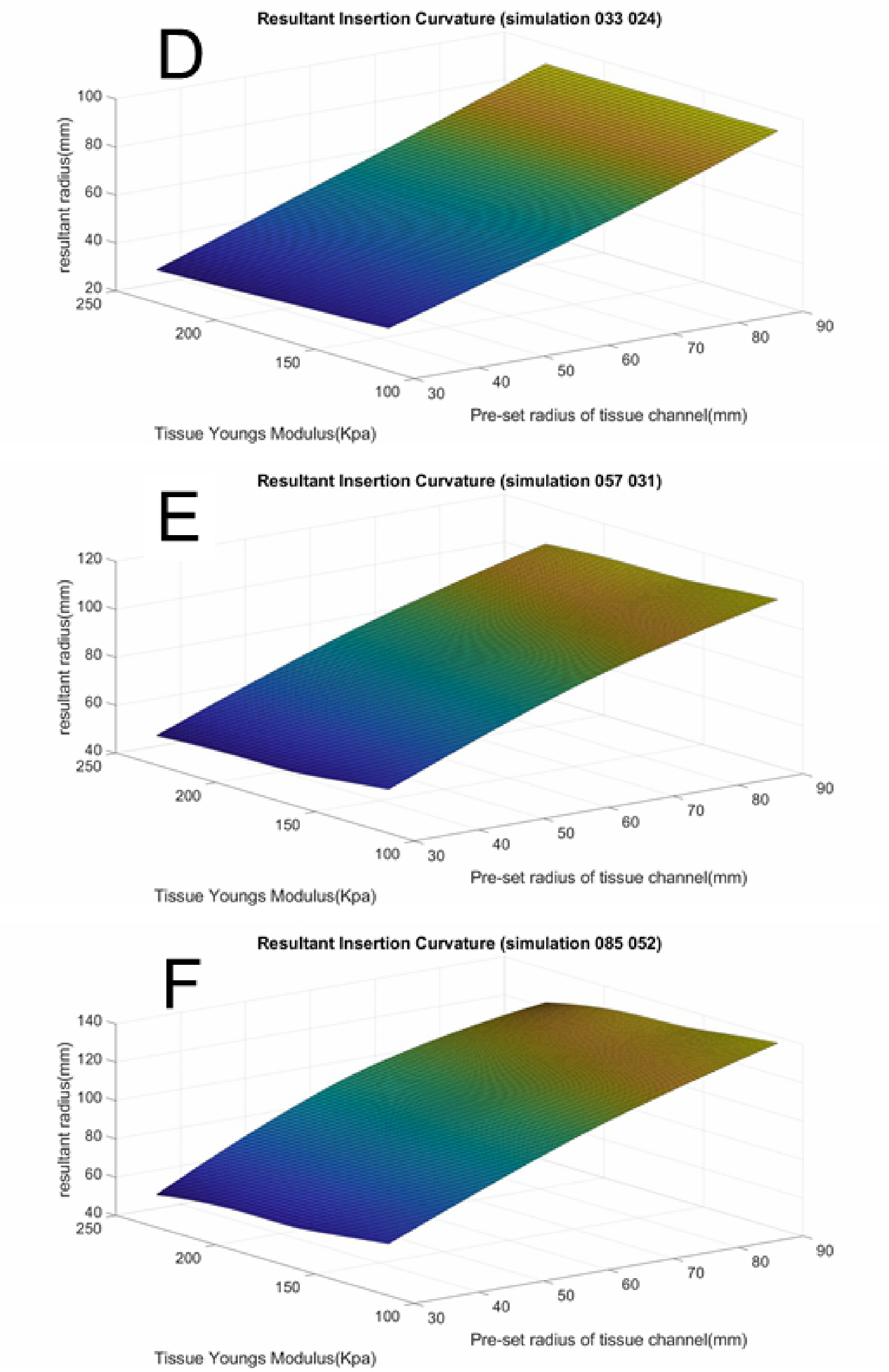

Figure 2.16: Resultant radii of curvature surfaces in experiments and FEA with different tissue phantoms and varying channel radii. (D) 0.33mm OD, 0.26mm ID tube, and 0.19mm wire in FEA. (E) 0.57mm OD, 0.32mm ID tube, and 0.29mm wire in FEA. (F) 0.85mm OD, 0.52mm ID tube and 0.47mm wire in FEA.

wire properly and tend to break through the boundary of the channel after the first 10-12mm during insertion because of the tight curvature of the channel and its high bending stiffness. The FEA provided a reasonable prediction for 30mm channel in Tissue 1 when high bending stiffness tube being inserted, the reason is that the tube was pre-loaded and pre-bend then put into the channel, so the pressure exerted on the channel wall was smooth and uniform. In reality, it's arduous to duplicate the setup we used in FEA, so we used a different approach to obtain the resultant radius of curvature. Since the FEA and experimental data have high similarity, the FEA data will be used to replace this specific data point when discussing tissue behavior in future sections.

By comparing the FEA data with experimental data, it's obvious that the resultant radius of curvature in experiments is slightly lower than the resultant radius of curvature in FEA except for the data point where the high bending stiffness tube inserted in Tissue 1 at 30mm channel. A hypothesis is that some of the mineral oil was escaped from the phantoms during storage since the experiments were conducted in around two days. The ratio rise of SEBS polymer will result in a stiffer tissue phantom which caused a decrease in resultant curvature.

In general, if tube and wire are selected, the stiffer the tissue phantom is, the smaller the resultant radius of curvature is. On the other hand, if tissue phantom has a specific Young's Modulus, the larger the bending stiffness of the tube, the larger the resultant radius of curvature is.

2.8.2 Finite Element Analysis for Validation

Finite element analysis has been used for finding the behavior and consequent deflection in both active and passive steerable needle research by Khashei Varnamkhasti et al.[30], Oldfield et al.[43] and Jushiddi et al.[27].

In fracture-directed stylet-and-tube needle steering approach, a channel is created first by an inner Nitinol stylet, and then is followed by a tube. Therefore, knowing the equivalent bending stiffness of the tissue channel after insertion of the needle is essential for predicting the resultant ROC and path planning. Thus, A finite element analysis has been developed for predicting equivalent bending stiffness of the tissue channel after needle insertion.

All SEBS tissue phantoms, Nitinol tubes, and wires involved in finite element analysis are exactly the same as those in experiments. Table 2.7 shows the mechanical properties of each tissue phantom, and Table 2.8 represents the sizes and mechanical properties of each combination of Nitinol tubes and wires. The complete finite element analysis contains two different parts, both are performed in the static structural solver. In the first part, a serial of points are selected along a straight Nitinol stylet, and then the moment reactions on these points are computed based on desired stylet curvature. In the second part, reversed moments are applied on these points along a curved stylet to simulate a pre-loaded straight stylet being released. In the end,

	Low Bending Stiffness		Medium Bending Stiffness		High Bending Stiffness	
Parameters	**Tube**	**Wire**	**Tube**	**Wire**	**Tube**	**Wire**
Outer Diameter (mm)	0.33	0.19	0.57	0.29	0.85	0.47
Inner Diameter (mm)	0.26	-	0.32	-	0.52	-
Bending Stiffness (N/m)	2.68e-05	4.85e-06	3.55e-04	2.68e-05	1.65e-03	1.80e-04
Length (mm)	150	180	150	180	150	180
Young's Modulus (GPa)	75	75	75	75	75	75
Poisson's ratio	0.33	0.33	0.33	0.33	0.33	0.33

Table 2.8: Parameters of the Tube, and Wire with Different Bending Stiffnesses: Low, Medium, and High

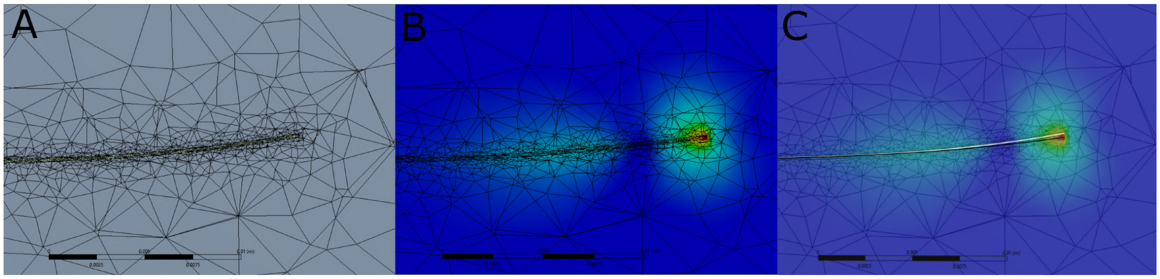

Figure 2.17: FEA model of the needle insertion into soft tissue. (A) A straight Nitinol tube is loaded with moments to form the same curvature as the pre-curved tissue channel. (B) Loads are released, and the tissue channel is deformed by Nitinol tube. (C) Overlap of parts A, and B, a clear curvature change can be observed. The centerline of loaded Nitinol tube was marked as white and the centerline of unloaded Nitinol tube was marked as black.

resultant radii of curvature are calculated based on displacement results from the FEA. Fig. 2.17 depicts The FEA modeling to find the resultant ROC of the needle which is a function of bending stiffness of the wire, tube, and soft tissue being inserted.

Tissue Phantom	**Density ($\frac{g}{cm^3}$)**	**Young's Modulus (kPa)**	**Poisson's ratio**
Tissue 1	0.85	112.9	0.49
Tissue 2	0.862	159.8	0.49
Tissue 3	0.865	229.57	0.49

Table 2.9: Mechanical properties of SEBS tissue phantoms. Tissues 1, 2, and 3 are 15%, 20%, and 25% G1650 SEBS in mineral oil soft tissue phantoms, respectively.

2.9 Comprehensive Predictive Model of Insertion Radius of Curvature

The comprehensive predictive model of insertion radius is presented under this section, it plays an essential role in the path planning algorithm, because it defines the reachable points set in state space. This model combines the step length model along with the tissue property model to predict the insertion radius based on a pair of designated tube-wire combination and a selected tissue phantom with unique Young's Modulus. Both finite element analysis and real-world experiments were conducted to enhance the reliability of this model.

The resultant insertion curvature κ_r, which is the reciprocal of resultant insertion radius, can be described as:

$$\kappa_r = f(\ell, K_w, K_b, K_t, \kappa_w, \kappa_b) \tag{2.15}$$

In the equation above, ℓ is the step length of the insertion, K_w, K_b, K_t are the bending stiffness of nitinol wire, tube and tissue respectively. κ_w and κ_b are the curvatures of nitinol wire and tube.

The stylets used in the experiment were made of superelastic nitiol. The common conservative superelastic Nitinol strain limit of $\varepsilon = 8\%$ [71]. The relationship between the recoverable strain limit and needle tip pre-curvature is:

$$\kappa = \frac{2\epsilon}{D(1+\epsilon)} \tag{2.16}$$

Then the calculated minimum radius of needle curve, r, is derived from

$$\kappa = 1/r \tag{2.17}$$

To effectively and efficiently describe the resultant insertion radii change caused by altering the pre-set radii of the needle tip, nitinol wires were pre-set to 0.03 strain, 0.04 strain, and 0.05 strain. All three strains are below the safe strain limit for nitinol 8% to ensure that the stylet can be fully straightened without any plastic deformation. The corresponding radii of pre-set curves were presented in Table 2.10, the curvature of all pre-set curves were constant.

In the experiments, two sets of tube-wire combinations were used, the parameters were shown in Table 2.11. Three types of tissue phantom were evaluated, 15%, 20%, and 25% SEBS tissue phantom, produced by Kraton Polymers LLC (G1650, Houston, TX, USA). Their mechanical properties can be found in Table 2.12.

Strain	R-0.1905mm wire	R-0.2901mm wire
3% strain	6.52mm	9.96mm
4% strain	4.94mm	7.54mm
5% strain	3.99mm	6.09mm

Table 2.10: Radius of pre-set needle tip curvature with different strain

	Low Bending Stiffness		High Bending Stiffness	
Parameters	**Tube**	**Wire**	**Tube**	**Wire**
Outer Diameter (mm)	0.33	0.19	0.57	0.29
Inner Diameter (mm)	0.26	-	0.32	-
Bending Stiffness (N/m)	2.6837e-05	4.85e-06	3.55e-04	2.6801e-05
Length (mm)	120	150	120	150
Young's Modulus (GPa)	75	75	75	75
Poisson's ratio	0.33	0.33	0.33	0.33

Table 2.11: Parameters of the tube, and wire with different bending stiffness

Tissue phantom	density ($\frac{g}{cm^3}$)	Young's Modulus (kPa)	Poisson's ratio
15% SEBS	0.859	112.9	0.49
20% SEBS	0.862	159.8	0.49
25% SEBS	0.865	229.57	0.49

Table 2.12: Mechanical properties of G1650 SEBS tissue-mimicking phantoms

The comprehensive resultant insertion radius predictive model was established by fitting surface into the data grid obtained from both experiments and FEA results. Experiments follow the standard insertion procedures described in steering method section. A top view photo was taken after each insertion. Then a curve with constant curvature was fitted into the captured image using MatLab(The MathWorks, Inc., Natick, Massachusetts, United States) to acquire insertion radii at designated step length. In Figure 2.18 and 2.19, ten insertions were performed at each step length from 1mm to 6mm in 15%, 20%, and 25% tissue phantoms and the average of data is obtained to reduce error. The plotted data are the mean value of ten insertions at each data point, the standard deviation from the mean was also calculated. The standard deviations of all data points fall under the range of 0.43mm - 1.62mm. The largest standard deviation was observed at 1mm step length of the high bending stiffness tube with 0.04 strain, the standard deviation at this data point is 3.08%.

Predictive models generated from FEA data can be found in Figure 2.20 and

2.21. The conducted FEA uses the same setup presented in ”Resultant Insertion Curvature Based on Tissue and Needle Properties” section. Pre-curved needles were placed in the center of tissue phantom to ensure proper boundary conditions.

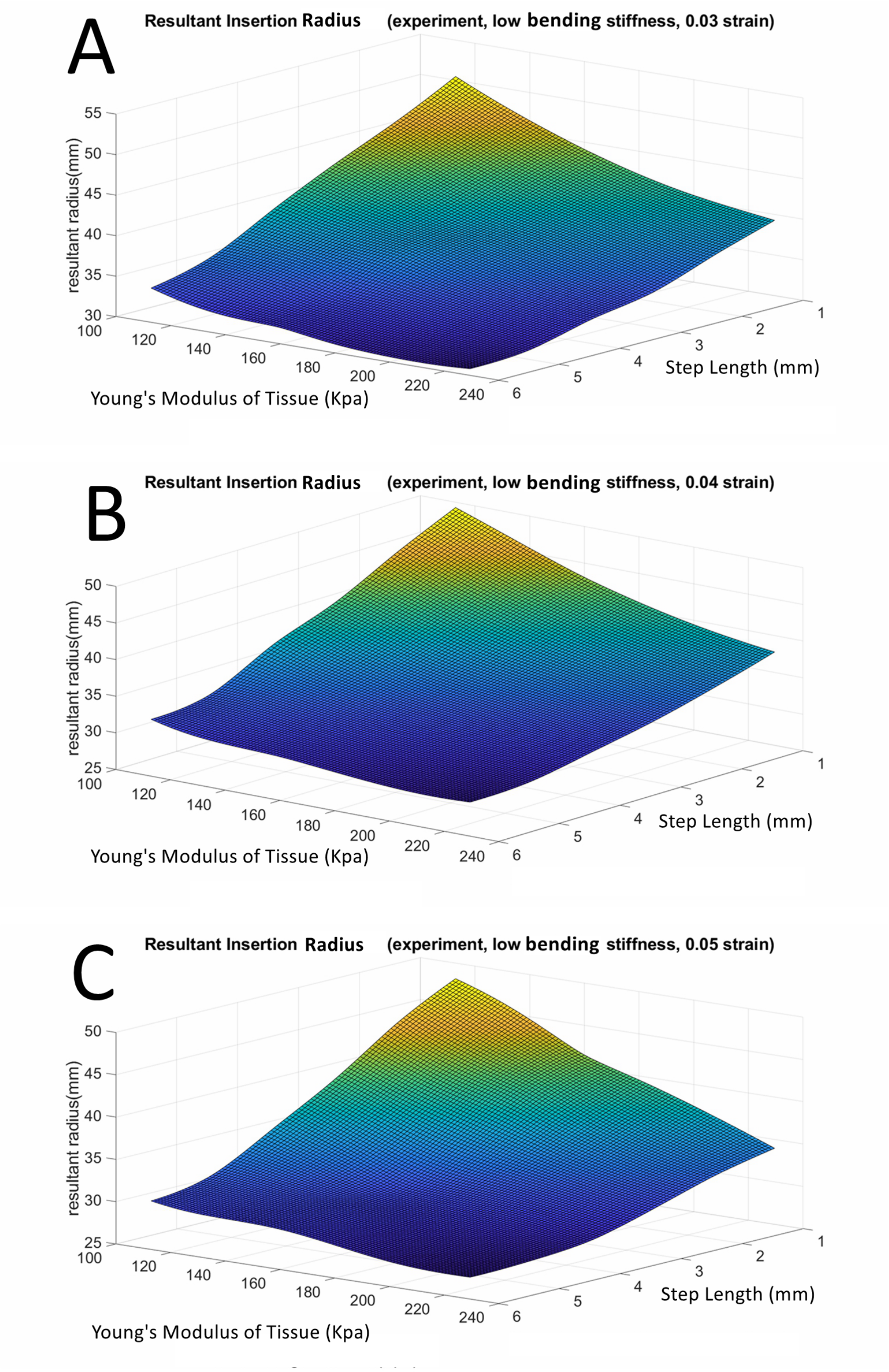

Figure 2.18: Predictive model generated from experiments data for three different low bending stiffness stylet. (A) The predictive model for low bending stiffness stylet with a 0.03 strain. (B) The predictive model for low bending stiffness stylet with a 0.04 strain. (C) The predictive model for low bending stiffness stylet with a 0.05 strain.

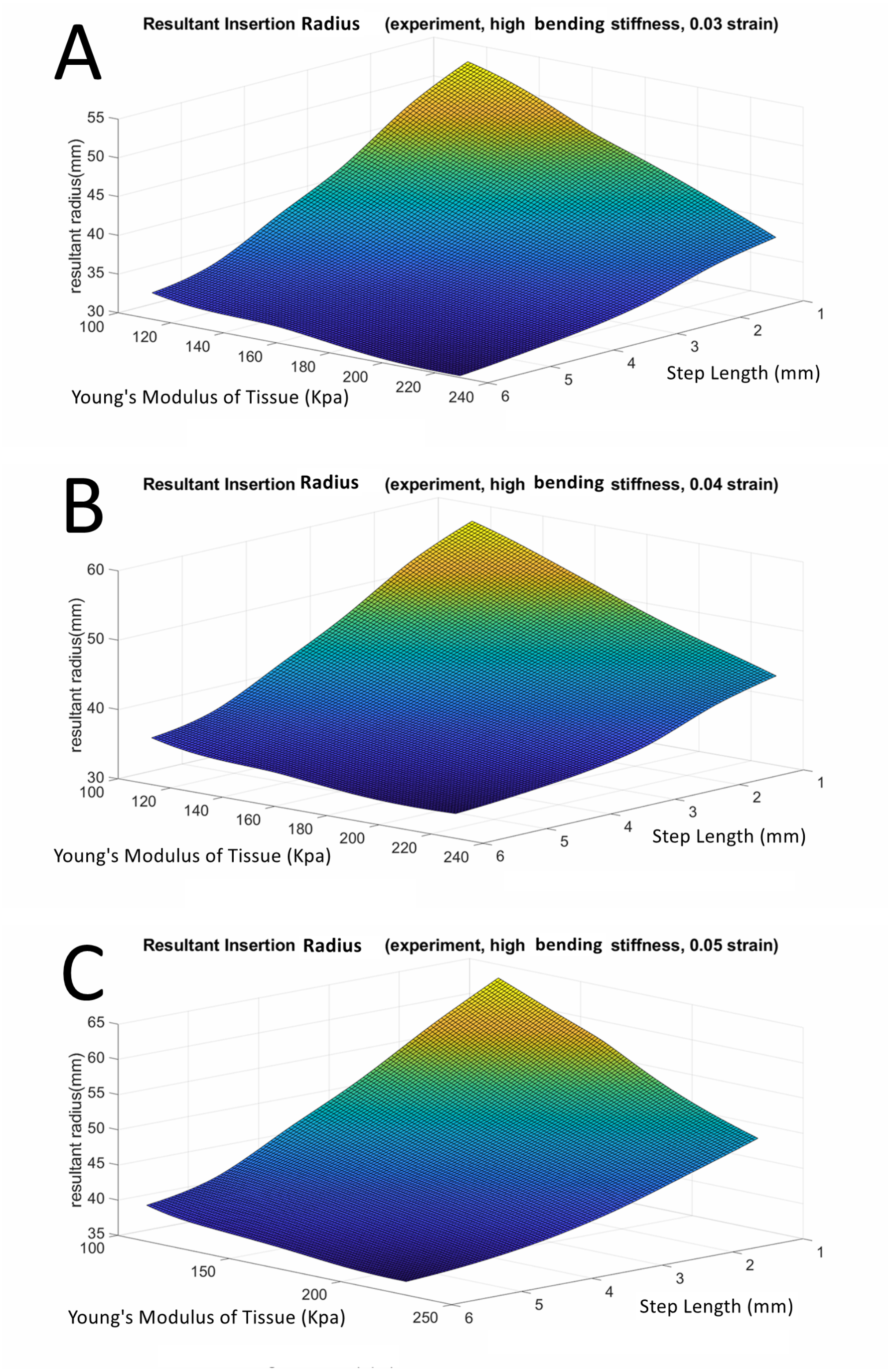

Figure 2.19: Predictive model generated from experiments data for three different high bending stiffness stylet. (A) The predictive model for high bending stiffness stylet with a 0.03 strain. (B) The predictive model for high bending stiffness stylet with a 0.04 strain. (C) The predictive model for high bending stiffness stylet with a 0.05 strain.

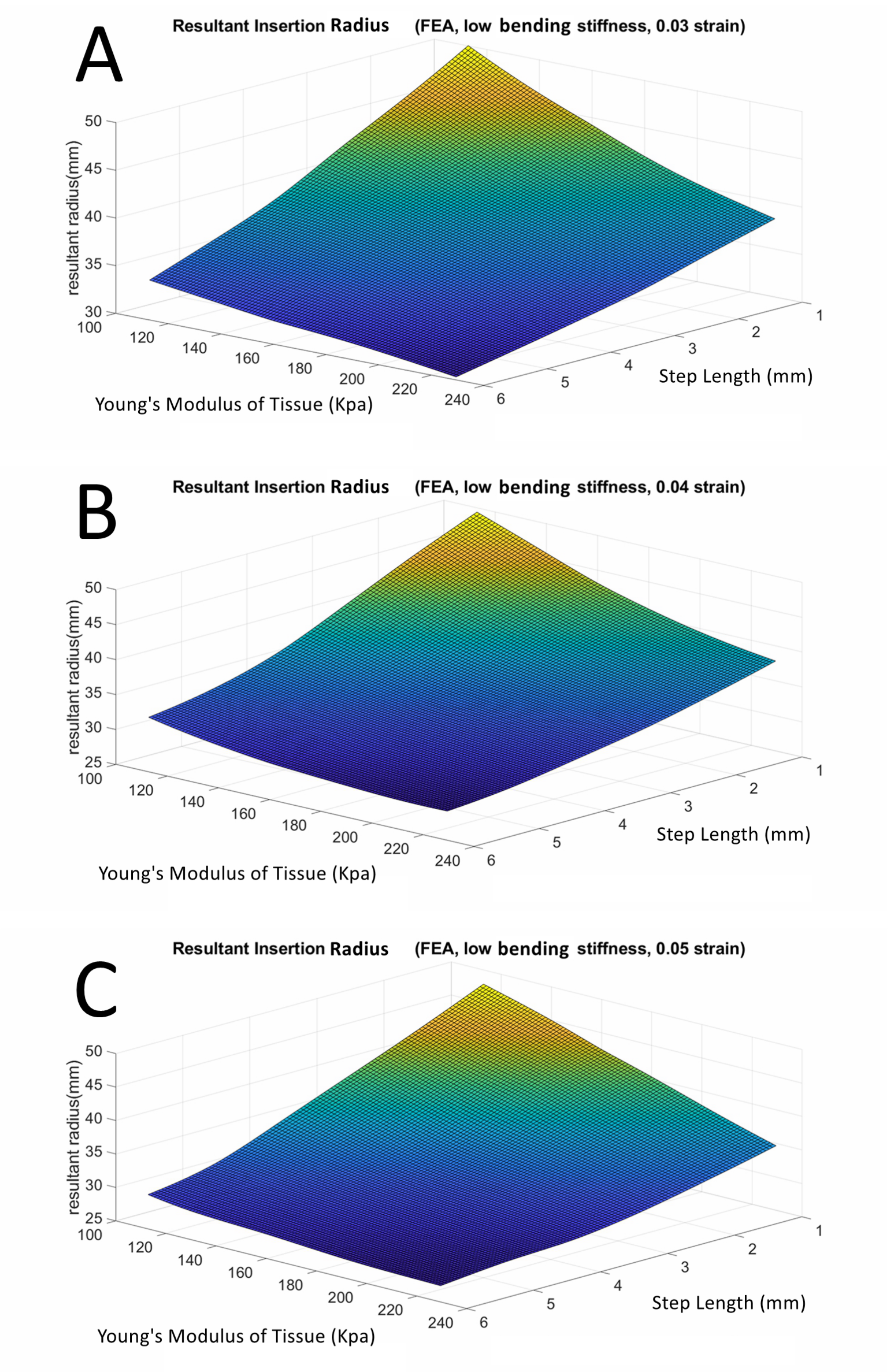

Figure 2.20: Predictive model generated from FEA data for three different low bending stiffness stylet. (A) The predictive model for low bending stiffness stylet with a 0.03 strain. (B) The predictive model for low bending stiffness stylet with a 0.04 strain. (C) The predictive model for low bending stiffness stylet with a 0.05 strain.

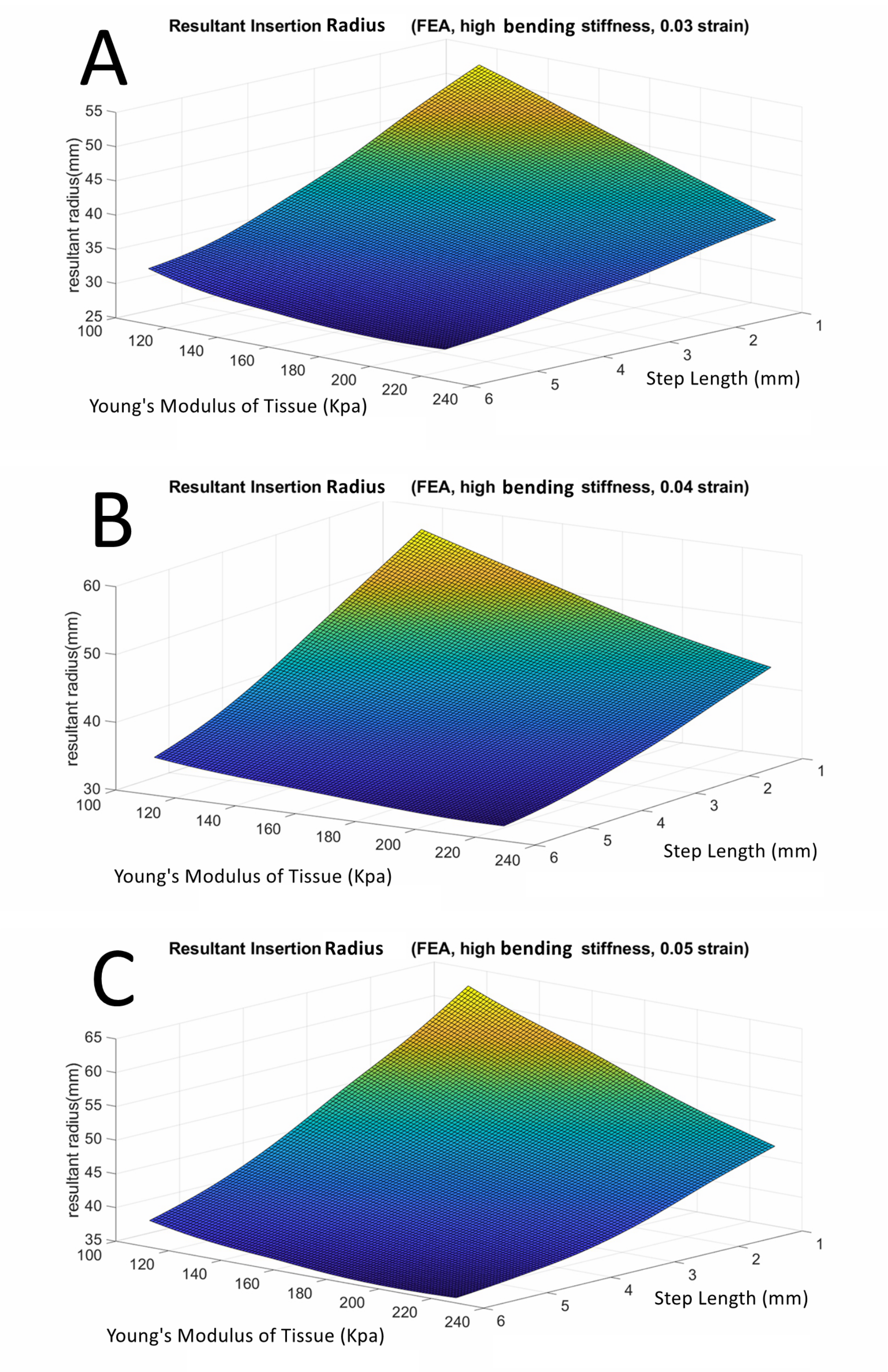

Figure 2.21: Predictive model generated from FEA data for three different high bending stiffness stylet. (A) The predictive model for high bending stiffness stylet with a 0.03 strain. (B) The predictive model for high bending stiffness stylet with a 0.04 strain. (C) The predictive model for high bending stiffness stylet with a 0.05 strain.

As we can observe from Figure 2.18, 2.19, 2.20, and 2.21, The resultant insertion radius surface map generated from FEA were smoother and more linear in step length-resultant radius plane. Also, most data points used to form the data grid in FEA have tighter radii than those from experiments. The observation above is reasonable, because the physical process simulated in FEA is closer to the ideal than experiments. There are few events that could possibly result in an inaccurate resultant radius of curvature: In the stylet insertion stage, when the needle is attempting to begin to fracture the tissue phantom, it first deforms the tissue until the fracture begins. With small step lengths, it is possible that some of the steps only deform the tissue and do not cause a fracture to begin. As such, the failure to fracture the tissue, or to have a larger deformation and smaller fracture distance, would result in a deviation from a scenario where the fracture and stylet step was perfectly coincident. Similar behavior occurs in the tube-follow stage when the tube is trying to follow the path created by the stylet. Additionally, some of the variability in the resultant insertion radius occurs because of the inexact angle in which the needle initially punctures the tissue. For larger stylet step lengths, the initial steps penetrate further into the tissues and create a better tissue anchor near the surface. Consequently, as the step length increases, the relationship between curvature and step length will be more stable. Another occurrence that could influence the accuracy of the measured resultant insertion radius in experiments is the loss of mineral oil in SEBS tissue phantom. SEBS powder was mixed in mineral oil then heated to fabricate the tissue phantom. However, the mineral oil can separate out from tissue phantom slowly after the fabrication. Either by evaporation or seep, mineral oil separates out from the tissue phantom with the standing time increases. Although all experiments were completed in 48 hours starts from the fabrication time of tissue phantoms, the loss of mineral oil could possibly cause the tissue phantoms' Young's Modulus to grow, which results in a tighter insertion radius.

2.10 Results

2.10.1 Insertion Directions

In these series of experiments, we showed how to control insertion direction. As can be seen from the Figure 2.22 and Figure 2.5, the direction of insertion can be reoriented by the rotation of the wire collet. Figure 2.22 depicts the first advancement of the inner stylet in the opposite direction from the initial curvature in the silicone compound tissue. As shown, both needle and tube originally exhibit a clockwise curvature; however, after the stylet and tube were rotated 180 degrees, the curvature is now directed in the counterclockwise direction. When rotating, the stylet has to be retracted back into the tube first. Figure 2.5 represents a triple-bend tube following the stylet each step after reorientation inside SEBS tissue.

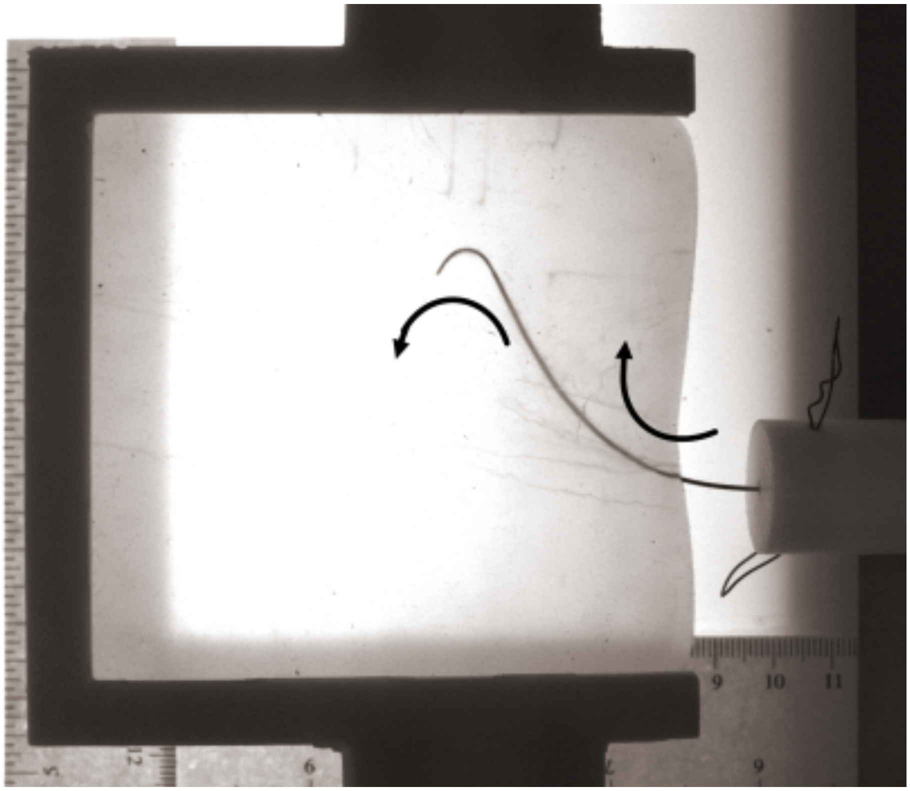

Figure 2.22: Rotation of the stylet changes direction of subsequent stylet insertions into silicone compound tissue.

2.10.2 Insertion Curvature

The technique we have used for needle path tracking is based on image analysis. By fitting a curve on the top view of insertion image, the insertion curvature of each needle can be obtained. As shown in Figure 2.2, as the step length increases, the wire comes out of the tube corresponding to further distance per step, which causes the needle arc length to rise. In the case of the spiral stylet, this corresponds to a changing curvature, but in the cast of the arc and right angle stylets, a constant curvature. The needle showed in Figure 2.2 is the Arc-stylet shape.

In a single insertion, there are three different states of curvature, as shown in Figure 2.1:

1. Initial state: Before the insertion, the relatively low tube stiffness is not enough to straighten pre-curved wire completely. Some amount of curvature is evident when tube and wire are fully overlapped.

2. Stylet insertion: The stylet goes into tissue, cutting a channel based on its preset curvature.

3. Tube follows stylet: The stiffness of tissue is insufficient to make the tube follow the exact path of the stylet, so the resultant shape is based on the stored elastic energy of the stylet, tube, and tissue. In our experiments where the tube stiffness is of the same order of magnitude as the tissue, the actual insertion curvature is less than stylet curvature.

2.10.3 Curvature as a Function of Step Length

Though the radius decreases with decreased step length, a characterization of the relationship between radius, step length, stylet geometry, and tissue stiffness is necessary. For each combination of tissues and stylet shapes, we have used several equal-interval step lengths to get different curvatures of needle insertion. Figure 2.10 demonstrates the relationship between the achievable radius with step length for different silicon compound tissue phantoms. This figure depicts the relatively linear relationship between the radius and step length for four different tissue phantoms with three different stylet shapes. Ten experiments are done for each step length and the average of data is obtained to reduce error. The error bars shown are standard deviation from the mean. For the heat treatment, Nitinol tube was heated up to $500^o C$ then let to be at $450^o C$ for 30 minutes, and then let to cool down to room temperature in the oven. The tissue phantom used in Figure 2.10D, 00-50, has the lowest Young's Modulus of 134 kPa among silicone compound tissues. In this tissue phantom, a slight lateral motion can be observed when the tube follows an inserted needle with a long step length. The cause of this lateral motion is the unbalanced bending stiffness relationship among tissue, stylet, and tube.

2.10.4 Insertion Radius and The Relationships among Tissue Bending Stiffness, Tube Bending Stiffness and Wire Bending Stiffness

The resultant insertion radius of the proposed stepping stylet and tube method is wholly dependent on the relationship between the bending stiffness of the tissue, K_t, the bending stiffness of the tube, K_b, and the bending stiffness of the wire, K_w. A very course description of an appropriate relationship of K_t, K_b and K_w is that $K_t > K_b > K_w$. Where the stylet geometry is often very small and stores very little elastic energy in bending, the most essential relationship is $K_t > K_b$. This relationship is derived from experimental data presented in this paper using and the equations relating the bending stiffness and curvatures of multiple overlapping curved tubes by Webster *et. al.*[71]:

$$\kappa_C = \frac{\sum_{i=1}^{n} E_i I_i \kappa_i}{\sum_{i=1}^{n} E_i I_i} = \frac{K_t \kappa_t + K_b \kappa_b + K_w \kappa_w}{K_t + K_b + K_w} \tag{2.18}$$

where κ_C is the combined curvature after the tube is fully overlapping the wire inside the tissue channel, and κ_t, κ_b, κ_w and K_t, K_b, K_w are the curvature and bending stiffness of the tissue channel, tube, and wire, respectively. I_i is the cross-sectional moment of inertia and E is the Modulus of Elasticity(Young's Modulus).

$$K_i = E_i I_i \tag{2.19}$$

The product of the Modulus of Elasticity and cross-sectional moment of inertia is bending stiffness. Here we are making a simplifying assumption and treating the channel that has been cut in the tissue as an outer tube. Because of the relatively small strains of the tissue using the relative stiffness heuristic, this simplifying assumption is valid.

If the tube bending stiffness is slightly higher than the tissue bending stiffness, it will cause an observable increase of the insertion radius. If the tube bending stiffness is significantly higher than the tissue bending stiffness, a significant straightening of the tissue channel will be observed and the tissue will undergo large strains.

Figure.2.11 shows the experimental results obtained by changing tube material from Nitinol to SemiFlex to satisfy the bending stiffness relationship between tube and tissue phantom. Furthermore, to adjust the stylet bending stiffness to match the tube, we picked a Nitinol stylet with a smaller diameter. The tissue phantoms used are 15% and 20% concentration SEBS. Comparing the silicone results shows in Figure 2.10 with those for the much more compliant tissues shown in Figure 2.11, the drastic improvement in the radius of curvature is due directly to the higher tissue stiffness relative to the tube and wire stiffness. Additionally, Figure 2.11A and Figure 2.11B show that when the tissue stiffness is decreased while using the same tube and wire stylet, the insertion radii of all three kinds of stylet shapes are increased. The two factors that will cause the change of tube bending stiffness, given a fixed material Young's modulus, are tube diameter and tube wall thickness.

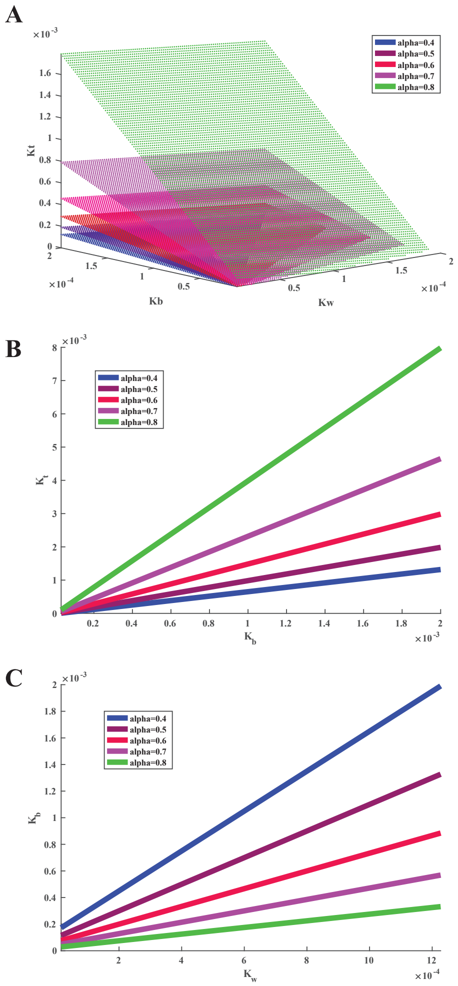

Figure 2.23: A simplified relationship between the curvature of the overlapped wire, tube, and tissue as a function of the bending stiffnesses of each of these components. The simplifications to the general relationship given in Equation (6) is that we assume the curvature of the tube is zero, $\kappa_b = 0$, the curvature of the tissue channel and the wire are equivalent, $\kappa_t = \kappa_w$, and we examine the specific cases where the curvature of the combined wire, tube, and tissue is a constant fraction of the curvature of just the wire stylet ($\kappa_C = \alpha\kappa_w$, where $0 < \alpha < 1$). (A) A plot of the simplified relationship between the stiffnesses for five different curvature ratios. The general trend is that as the tube and wire stiffness increases the tissue stiffness must also increase to maintain the same curvature ratio. (B) For a fixed tissue channel bending stiffness, K_t, the relationship between wire and tube stiffnesses that maintains the curvature of the overlapping configuration. (C) For a fixed wire bending stiffness (i.e. a particular wire diameter and material), the relationship between the tube bending stiffness (i.e. a particular tube diameter, wall thickness, and material) and the tissue bending stiffness that maintains the curvature of the overlapping configuration.

Figure.2.23 shows a simplified tissue, wire and tube relationship for a single step length. We assume the curvature of the tube is zero, and the curvature of the tissue channel is equivalent to the wire. These simplifying assumptions turn Equation (6) into the simplified form:

$$0 = (1 - \alpha) K_w K_t - \alpha K_b + (1 - \alpha) K_w \tag{2.20}$$

Equation (8) describes a planar surface in K_w, K_t, and K_b. Note that the relationship no longer depends on curvature terms, such that the stiffness relationships between tissue, tube, and wire hold true for any curvature of the wire and the tissue channel it cuts.

The proper establishment of relationships among K_t, K_b and K_w will bring a high steerability to the system. By selecting wires and tubes that have much lower bending stiffness than the tissue, the insertion radius has the tendency to be reduced to nearly the curvature of the pre-shaped wire stylet.

2.11 Discussion

2.11.1 Similar Resultant Insertion Radius across a Range of Young's Modulus of The Tissue Phantoms

Experimental data of various stylet shapes, tube materials, and different tissue phantoms demonstrate that once an appropriate bending stiffness relationship among tissue phantoms, stylets, and tubes is established, an approximately linear relationship between insertion radius and step length can be achieved. Figure 2.10 shows that this fracture-directed method of steering results in a small change in the radius across a certain range of Young's modulus of the tissue phantoms. Figure 2.11 shows that a doubling in the Young's modulus between the 15% and 20% SEBS tissues resulted in 20-40% change in the insertion radius. This is an observable increase of insertion radius, but the modeling presented provides a method of determining an upper bound on the curvature for the most compliant tissue that will be encountered in insertion and feedback control can achieve any curvature lower that the maximum through the step length control. Figure 2.23 B explained the phenomenon appeared in SEBS tissue phantom and demonstrates the tissue agnostic behavior. As the bending stiffness of the tube and stylet become low compared to the tissue bending stiffness (the situation in SEBS tissue), the tissue bending stiffness can vary by a large amount while having a small effect on the effective resultant combined curvature. Once the bending stiffness of the tube and stylet become high compared to the tissue bending stiffness (situation in silicon tissue), any softer tissue will result in rapid degradation of the achievable insertion curvature. Thus the objective should be to create stylets and tubes with as low of bending stiffness as possible while still maintaining the ability to effectuate cutting.

Additionally, the lowest insertion radius attained in experiments with silicone compound tissue phantom using Nitinol tube is 29.58mm, and the lowest insertion radius attained in experiments with SEBS tissue phantom using SemiFlex tube is 6.88mm. To the authors' knowledge, this is the best-reported radius of curvature achieved among all needle steering methods.

2.11.2 Insertion Radius is linear as a function of step length

The achievable insertion radius, as a function of the step length of the stylet out of the tube before following with the tube, can be fitted with a high degree of accuracy to a line. The curve fitting and the goodness of fit are shown in Figure 2.10 and Figure 2.11. For each of the stylet designs, those two figures also demonstrate that the linear relationship between step length and curvature is only valid for a limited range of the insert lengths tested. While having a linear relationship is not necessary for accurate control, it does simplify the process of simulation and control. For the right angle stylet, the curved region of the stylet has fully exited the tube at the $4mm$ step length, thus any additional insertion becomes less effective and the linear fit is only computed using the $1mm$ through $4mm$ step lengths.

2.11.3 Establishment of Comprehensive Resultant Insertion Radius Predictive Model

In this dissertation, the comprehensive predictive models were established on the data grids obtained from experiments in various tissue phantoms. Based on the relatively linear relationship between resultant radius and step length, once a proper combination of the outer tube and inner wire was selected for tissue phantom with specified Young's Modulus, a surface present resultant insertion radius can be generated. This model can be potentially expanded among different pre-set needle shapes and diverse tissue phantoms. Finite element analysis was conducted to enhance the reliability of all provided predictive models. Data points collected from FEA only had minor differences comparing to experimental data. The maximum relative error based on experimental data was observed in 25% SEBS tissue phantom with 0.04 strain nitinol wire and high bending stiffness tube, the value of the maximum relative error was 4.08%. More than 75% of relative errors were fallen under the range of 1.44%-2.27%. The path planning and re-planning algorithms introduced in chapter 4 was developed based on predictive models described above.

2.12 Conclusion

We have presented the design, assembly, and analysis of a new class of needle insertion system, which we have called fracture-directed steerable needles. The needle insertion can be controlled by changing the servo motor rotation angle and the step length of the stylet relative to the tube which will follow. A comprehensive analysis based on material stiffness, single insertion step length and insertion radius were given. This analysis provided a functional model about the radius-step length relationship for three different stylet geometries and across several tissue simulants with more than an order of magnitude variability in Young's Modulus. A linear relationship between the radius and stylet step lengths for each tissue stiffness was also established.

We have additionally presented a preliminary bending moment analysis between the tube, tissue, and needle. By selecting the wire stylet and tube geometries based on the bending stiffness of the channel cut in the tissue, approximated as an outermost tube, the proposed method is capable of achieving high curvature across all tissue having a higher stiffness than the tissue for which the tube and wire were selected.

A method of treating tissue channel as an outer tube and an approach to predict the resultant radius of curvature for fracture-directed stylet-and-tube needle steering technique was also described in this chapter. The experiments conducted for the resultant radius of curvature serve as a part of fracture directed steerable needle research. The model can be expanded across a wider range of tissues' Young's Moduli or pre-set wire curvatures by simply conducting experiments on the target data field. By combining with the step length model, a complete model for a specific insertion can be described as

$\kappa_r = \mathrm{f}(\ell,\, K_w,\, K_b,\, K_t,\, \kappa_w,\, \kappa_b)$

where κ_r is the insertion curvature, ℓ is step length, κ_t, κ_b, κ_w and K_t, K_b, K_w are the curvature and bending stiffness of the tissue channel, tube, and wire, respectively.

Comprehensive predictive models for predicting resultant insertion radius was established, Finite element analysis was conducted to enhance the reliability of predictive models. Various pre-set needle shapes and tissue phantoms with diverse Young's

Modulus can be fit in this approach. It forms a good fundamental for needle path planning and needle manipulation in both 2D and 3D spaces.

CHAPTER THREE

VISION-BASED PATH PLANNING AND CLOSED-LOOP RE-PLANNING FOR NEEDLE STEERING

3.1 Related work

Robotically steered steerable needles have been thoroughly researched in recent years, the kinematic models of insertion and tissue reactions are diverse. However, the dominant approaches of describing tissue-needle interaction force and insertion models are virtual spring models and kinematic models that described by an insertion velocity of ν and a rotation velocity ω [15, 55, 1, 42, 67, 21, 69].

An analysis of tissue-needle interaction forces was conducted using FE simulations by S.Misra et al [38]. The forces on the needle tip were determined to be sensitive to the rupture toughness of the tissue. And needle tip forces were not significantly influenced by nonlinear material elasticity up to 38% variation. Since most steerable needles are designed to be steered in soft tissues, a variation larger than 38% is not excepted.

V.Kallem et al. [28] proposed a controller that stabilizes steerable needle to a 2D plane, a reduced order of needle tip with only position and no orientation can be recovered by a linear observer designed by the author. With this proposed method, only 3 of the 6 degrees of freedom need to be tracked during an insertion. This method was tested with 1000 initial conditions and 98.56% converged to within ±1

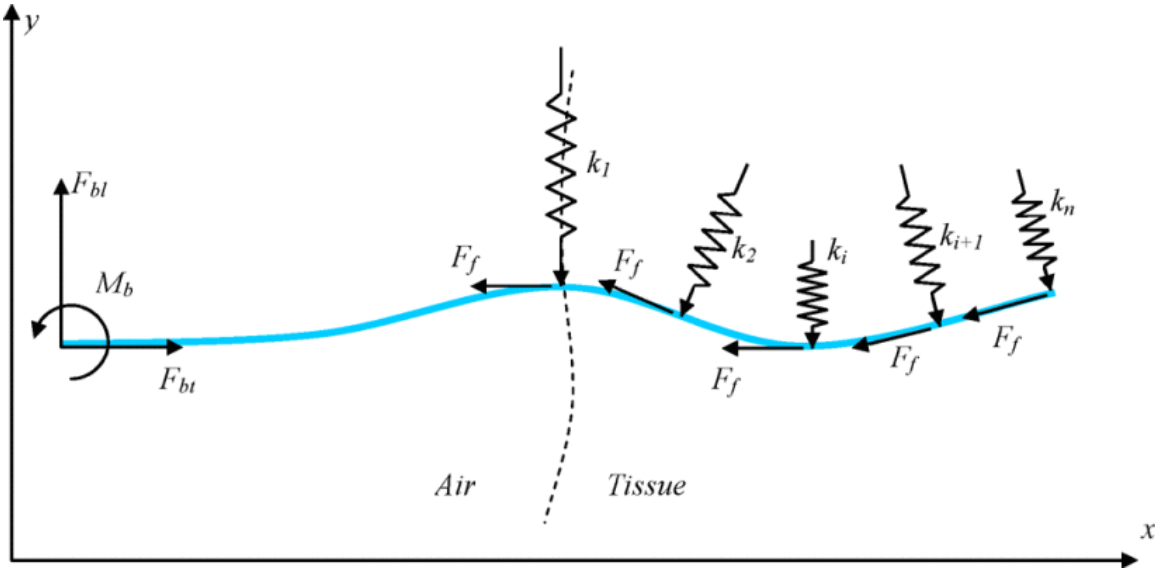

Figure 3.1: An example of virtual springs model: the interaction of the tissue with the needle is modeled by distributed virtual springs. Retracted from [25]

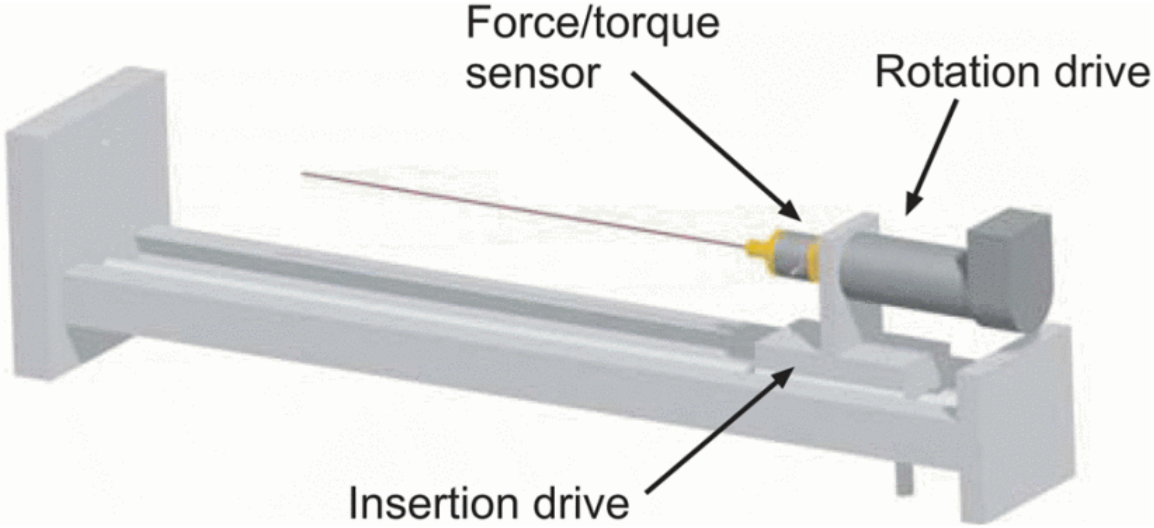

Figure 3.2: A typical needle insertion device to steer flexible needles that contains both a insertion mechanism and a rotation mechanism. Retracted from [67]

mm, which is the sensor noise floor. The remaining 1.44% initial conditions were also inspected, and they did not show the sign of diverging in finite insertion distance. This approach also proved to be robust to parametric uncertainty and take up to 20% error for insertion curvature κ.

The path planning algorithms that commonly used for steerable needles are minimal lateral pressure algorithm [24], plane transformation algorithm [42], LQG(linear–quadratic–Gaussian)-based algorithm [66], and RRT(rapidly-exploring random trees) algorithm [48, 4, 74]. Each algorithm has its own priorities. Distance expense, computation time, insertion safety, and ability of later adjustment are the four main considerations.

V.Duindam et al. [16]proposed a path planning algorithm with two types of discretizations for needle rotation velocity, stop-and-rotate insertion strategy, and helical insertion strategy. By applying the discretizations of control input, the algorithm was described as a nonlinear optimization problem, which is solving analytic expression for the position of the needle as a function of the control input.

S.Patil et al. [48] developed a RRT path planning algorithm that able to compute hundreds of feasible motion plans inside a single second. The motion planner was implemented in C++ and tested on a 3.33 GHz 4-core Intel PC. This work also supports adding obstacles in real-time during operation.

Another RRT path planning algorithm was presented by J.Xu et al. [74] This work used a randomly sampled space instead of traditional deterministic spaces that appeared more often in RRT path planning. The feasible entry point problem was solved by the back-chaining technique. The average number of iterations for RRT with back-chaining was 279.2, the corresponding CPU time was 195.2 seconds. The described simulation was conducted on 1.66MHz Intel PC with 1GB memory.

J.Berg et al. [66] developed a LQG based path planning algorithm for needle steering. This research was focused on insertion safety, it takes into account the noisy feedback from senor and insertion uncertainty to minimize the possibility of needle-obstacle intersects. A Kalman filter was also applied to reduce errors from sensor readings. The operation time of the algorithm to get an optimal pair over all possible solutions is 185 seconds.

3.2 Kinematic Model of Fracture-directed steerable needles

The kinematic model of fracture-directed steerable needles was presented in Figure 3.3. The body-fixed frame ψ_k at step k is attached to the needle tip. And the body-fixed frame at next step k+1 is described as ψ_{k+1}. ψ_w is defined as the world frame. Z-axis of the body-fixed frame is aligned along the stylet shaft when tube and wire are overlapped, Y-axis of the body-fixed frame is the axis parallel to the rotation axis of needle tip. The x-axis of the body-fixed frame is defined as the direction towards the center of the imaginary step length circle. An imaginary circle with radius r can be fit on to the step length arc. This radius for step k is defined as r_k, and the range of r_k is pre-defined by the comprehensive resultant insertion radius predictive model for each tube-wire combination and tissue phantom.

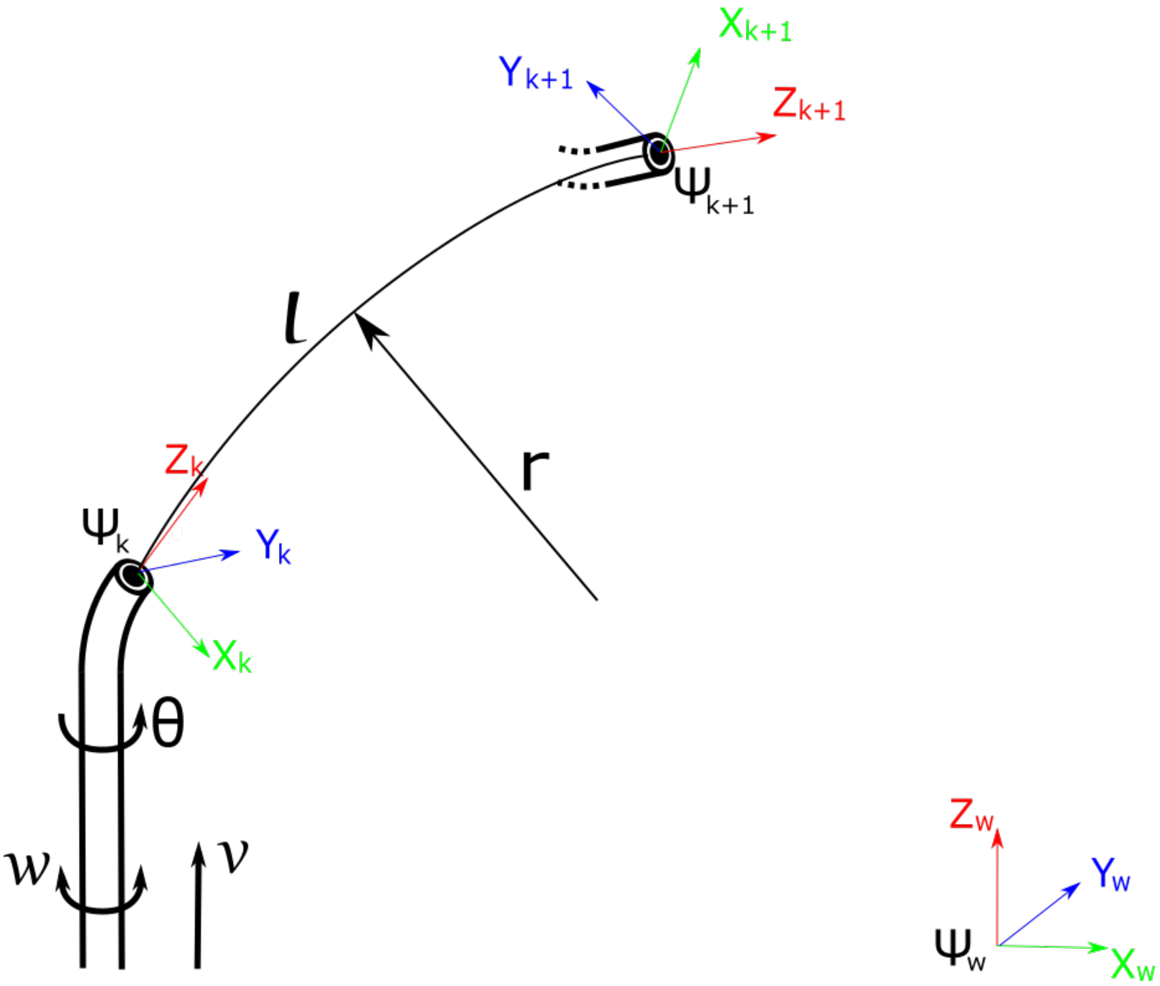

Figure 3.3: position and orientation of needle tip at k step is defines as the body-fixed frame ψ_k relative to world frame.

The pose of the needle tip after a step can be calculated as the product of matrix exponential of the twist and the previous pose,

$$g_{k+1} = e^{\hat{\xi}_k l} g_k. \tag{3.1}$$

The discrete-step position/orientation change is only a function of the length of the needle that is inserted before the tube follows. The matrix $g_k \in SE(3)$ is the needle tip position/orientation before the wire is inserted and $g_{k+1} \in SE(3)$ is the needle tip position/orientation after the wire has been inserted and the tube has followed. The position and orientation of the needle tip at step k with respect to the previous reference frame can be described by a $4 * 4$ matrix:

$$g_k = \begin{bmatrix} R_k & P_k \\ 0 & 1 \end{bmatrix}. \tag{3.2}$$

where the rotation matrix $R_k \in SE(3)$ describes the orientation relative to previous frame and the translation vector $P_k \in T(3)$ describes the position relative to previous frame.

The insertion strategy of needle insertion is stop-and-rotate. The twist coordinates of the insertion phase are defined as follows:

$$\xi(l) = \begin{bmatrix} \omega \\ v \end{bmatrix} = \begin{bmatrix} \kappa(l) \\ 0 \\ 0 \\ 0 \\ 0 \\ 1 \end{bmatrix} \tag{3.3}$$

or equivalently represented as:

$$\xi(l) = \begin{bmatrix} 0 & 0 & 0 & 0 \\ 0 & 0 & -\kappa_k & 0 \\ 0 & \kappa_k & 0 & l \\ 0 & 0 & 0 & 0 \end{bmatrix}. \tag{3.4}$$

The twist coordinates of the rotation phase are defined as follows:

$$\xi(l) = \begin{bmatrix} \omega \\ v \end{bmatrix} = \begin{bmatrix} 0 \\ 0 \\ \theta \\ 0 \\ 0 \\ 0 \end{bmatrix} \tag{3.5}$$

or equivalently represented as:

$$\xi(l) = \begin{bmatrix} 0 & -\theta_k & 0 & 0 \\ \theta_k & 0 & 0 & 0 \\ 0 & 0 & 0 & 0 \\ 0 & 0 & 0 & 0 \end{bmatrix}. \tag{3.6}$$

3.3 RRT Based Path Planning and Closed-loop Re-planning for Fracture-directed Steerable Needles

The RRT path planning method was introduced by J.Kuffner et al. [34]. The goal of this RRT based path planning algorithm is to first find an optimal path that the needle can follow to reach the target locations while avoiding all existing obstacles in state space, then re-plan the path when the error of needle tip position or orientation was observed. The simulation of RRT path planning for fracture-directed steerable needles was conducted in MatLab, the parameters of obstacles and needle were assumed to be collected from images captured from two cameras shown in the chapter of needle insertion device. Figure 3.4 shows the setup of camera and tissue.

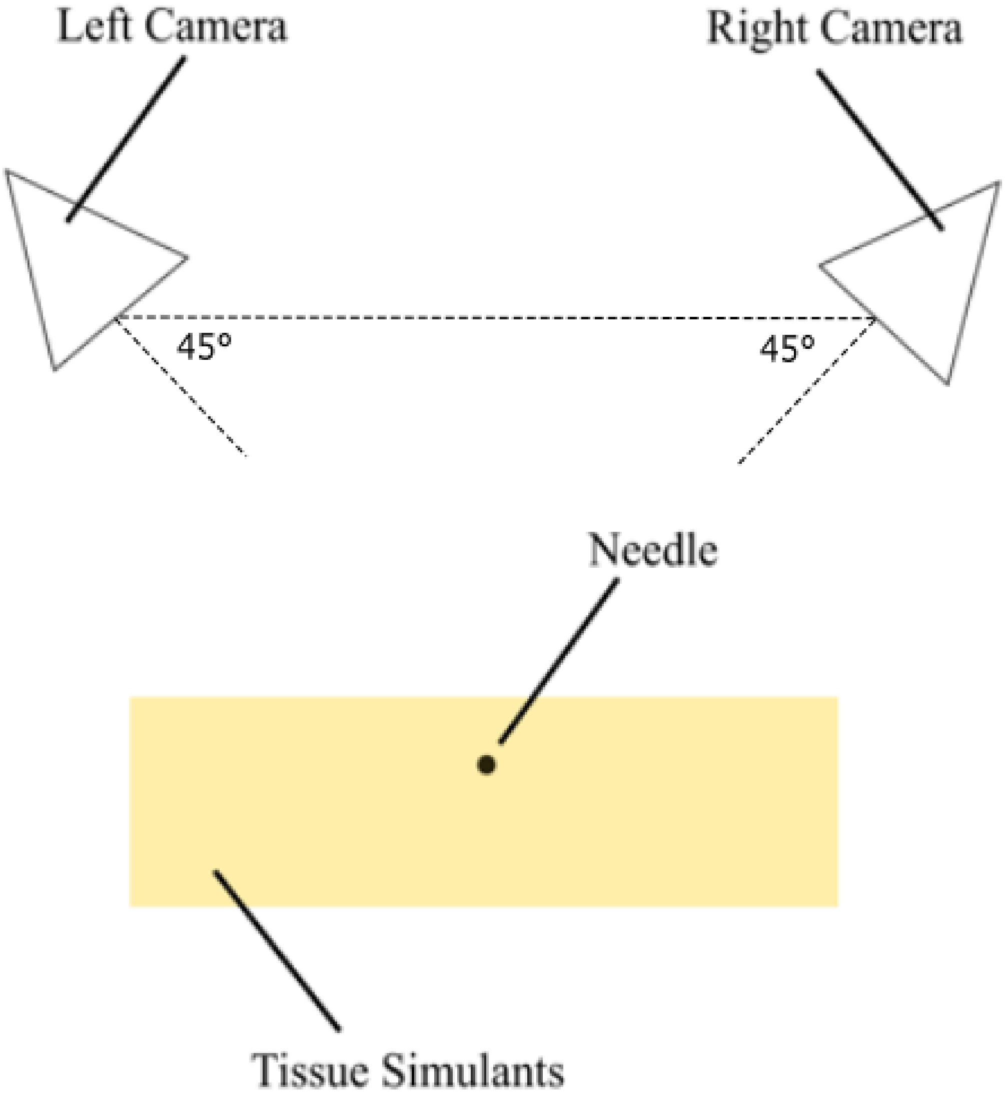

Figure 3.4: The front view of the camera setup

The two inputs of path planning algorithm are the step length of insertion l and the rotation angle along the needle shaft θ. And the output is a set of potential insertion paths. After all potential insertion paths being generated, an optimal path with the lowest distance expense will be selected. An overview of RRT based path planning process can be found in Figure 3.5.

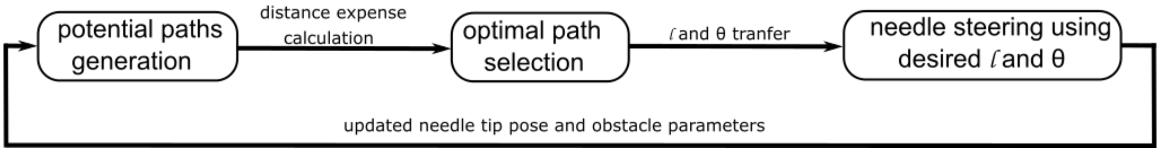

Figure 3.5: The overview of RRT based path planning process

3.3.1 Reachable set of nodes

A traditional RRT algorithm randomly generates a set of new nodes around an existing node to grow the tree. But not all of the generated nodes are reachable for the needle tip due to the kinematic constraints. The achievable insertion radius depends on the length of the pre-set curve, the mechanical properties of the tissue, as well as the mechanical properties and geometries of the selected combination of tube and wire. Rather than filtering out unreachable nodes after random nodes generation, we chose to develop a reachability-guided RRT algorithm to restrict the nodes generation within the reachable set of needle tip positions. The idea of a reachability-guided rapidly-exploring random tree (RG-RRT) was first introduced by A.Shkolnik et al. [57]. This approach eliminated the lengthy nodes filtering process and allowed for quick completion of the search.

3.3.2 Collision Avoiding

An essential part of RRT based path planning algorithm for steerable needles is collision checking and avoiding. The geometry used to define obstacles in our algorithm is cubes. The approach to check collision is by examining the insertion arc in each configuration. If the insertion intersects any surface of the cubes, the node x_{new} will be removed from the previous node x_{near}.

3.3.3 Potential Paths Generation and Optimal Path Selection

The proposed RG-RRT based path planning algorithm is shown below in algorithm 1:

The tree starts with an initial configuration *x_init*, and expands towards the target location X_{target}. During the expansion of the tree, a set of potential paths τ is established, all elements in τ satisfy both the nonholonomic kinematic constraints defined by the comprehensive predictive model of resultant insertion radius and the obstacle avoiding requirements. The tree keeps expanding until the target location being hit or the pre-set maximum process time t has been reached. The distance expense of reachable nodes along all potential paths, then the nodes on the optimal path with the lowest distance expense were connected from the target back to the start point.

Algorithm 1 RG_RRT_needle_3D(x_{init}, X_{target}, t, N_{max})

```
$\tau \leftarrow$ Initialize_tree($x_{init}$)
while ($\tau \cap X_{target} = \emptyset$ and process_time $<$ t) do
    repeat
        $X_{reach} = \emptyset$
        $N_p = 0$
        $p_{rand} \leftarrow$ random_point_in_$\mathbb{R}^3$
        for $x_i \in \tau$ do
            if reachable($p_{rand}$,$x_i$) then
                $X_{reach} \leftarrow X_{reach} \cup x_i$
                $N_p = N_p + 1$
            end if
        end for
    until $N_{max} - N_p = 0$
    $x_{near} \leftarrow$ nearest_neighbor_in_$\mathbb{R}^3$ ($p_{rand}$,$X_{reach}$)
    $x_{new} \leftarrow$ circular_arc ($x_{near}$,$p_{rand}$)
    if no_collision($x_{near}$,$x_{new}$) then
        $\tau \leftarrow$ add_vertex($x_{new}$)
        $\tau \leftarrow$ add_edge($x_{near}$,$x_{new}$)
    end if
end while
return $\tau$
```

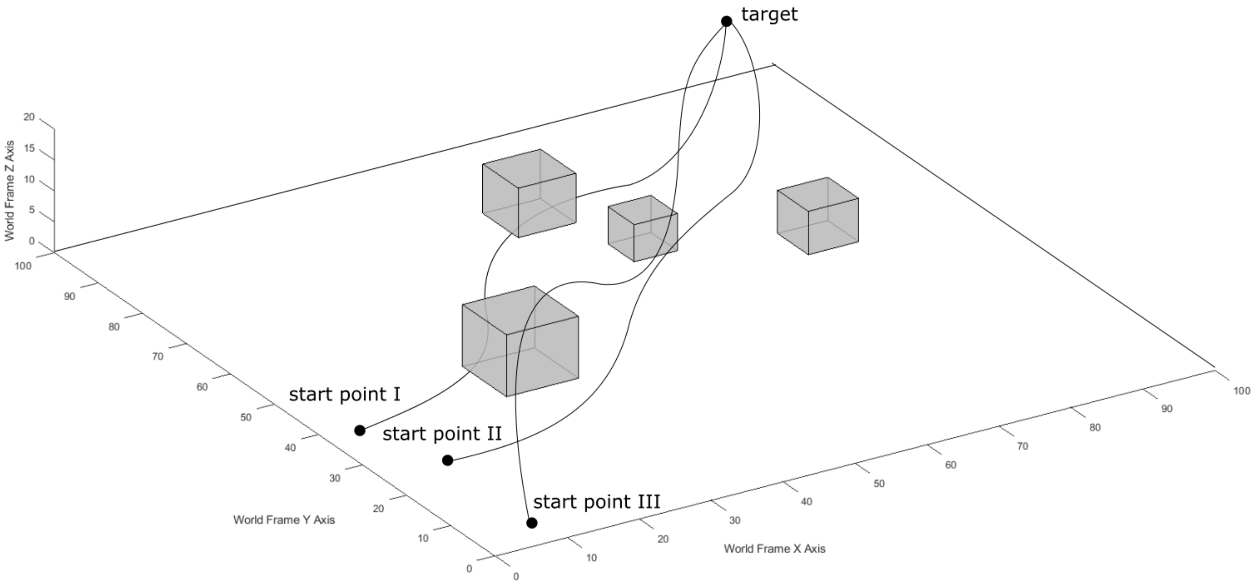

Figure 3.6: Three optimized paths were generated for three different start nodes using proposed RG-RRT based path planning algorithm.

3.3.4 Closed-loop Re-planning

To simulate needle manipulation error and position reading error that ubiquitously existed in mechanical actuators and vision-based controls, random errors were added to the needle tip pose matrix to test the dependability of closed-loop re-planning. Figure 3.7 indicates the two stages in the planning process that errors show up frequently.

Figure 3.8 shows the re-planning process after an error presented in an insertion

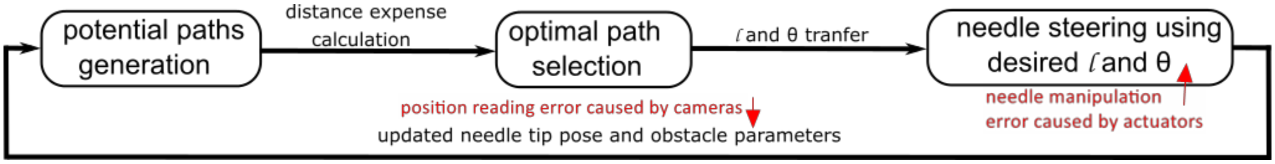

Figure 3.7: Two stages where needle manipulation error and position reading error most likely to occur.

segment(consists of multiple steps with the same step length).

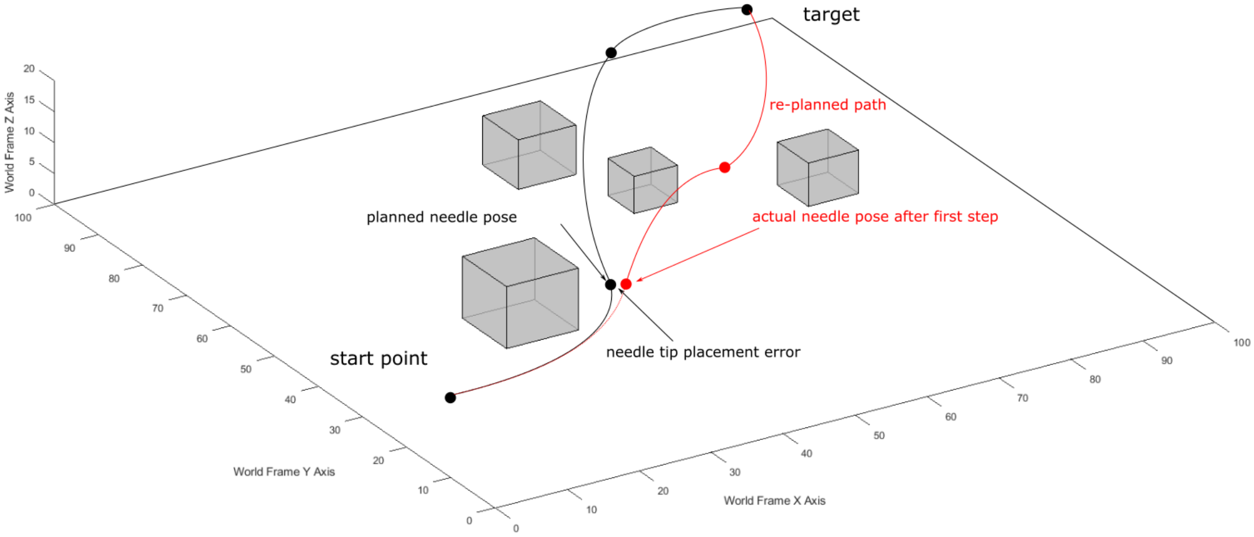

Figure 3.8: The path re-planning process of RG-RRT based algorithm. After the needle tip deviated from its planned position after the first insertion, the second optimized path was planned based on current needle tip pose.

3.4 Straight-curve-straight Path Planning and Closed-loop Re-planning for Fracture-directed Steerable Needles

Due to the special correlation between insertion radius and step length in fracture-directed needle steering approach, and the limitation of RRT method. The RG-RRT based path planner is effective but not always efficient in terms of distance expense. Here we propose another heuristic path planning algorithm named straight-curve-straight path planning method to lower the distance expense. The proposed two-dimensional SCS path planning algorithm is shown below in algorithm 2:

Algorithm 2 SCS_2D(x_{init}, t)

```
$x_v \leftarrow$ all_vertices_of_obstacle_in_$\mathbb{R}^2$
$x_{targ} \leftarrow$ target
while (process_time < t) do
    for $x_{vi} \in x_v$ do
        if no_collision($x_{init}$, $x_{targ}$) then
            find minimum reachable radius to drive needle tip from initial point to target
        else if no_collision($x_{init}$, $x_{vi}$, $x_{targ}$) then
            find the minimum valid $r_{\alpha i}$_&_$r_{\beta i}$
        else print "path not available"
        end if
        $d_{exp} \leftarrow$ calculated distance expense from $x_{init}$ to target for each valid path
    end for
end while
return path with $min(d_{exp})$
```

The path planning procedure of SCS planner is to first find a line connection between the start point and an obstacle vertex, then a line connection between the vertex and target location while having no collision with the obstacle in state space.

Then find two points $x_{m\alpha}$ and $x_{m\beta}$ on the middle perpendicular lines of each line segment. A path that starts from the initial point and passes $x_{m\alpha}$, $x_{m\beta}$, and target location will then be generated. Finally, the fillets with reachable radius r_α and r_β orient the needle from a line segment to another line segment. The collision checking function examines both line segments and generated fillets to avoid potential intersections with obstacles. The reorientations remain valid while $l_{c\alpha}$ greater the distance from start point x_{init} to $x_{m\alpha}$ and $l_{c\beta}$ greater the distance from $x_{m\alpha}$ to target location. The geometric representation of SCS path planner can be found in Figure 3.9

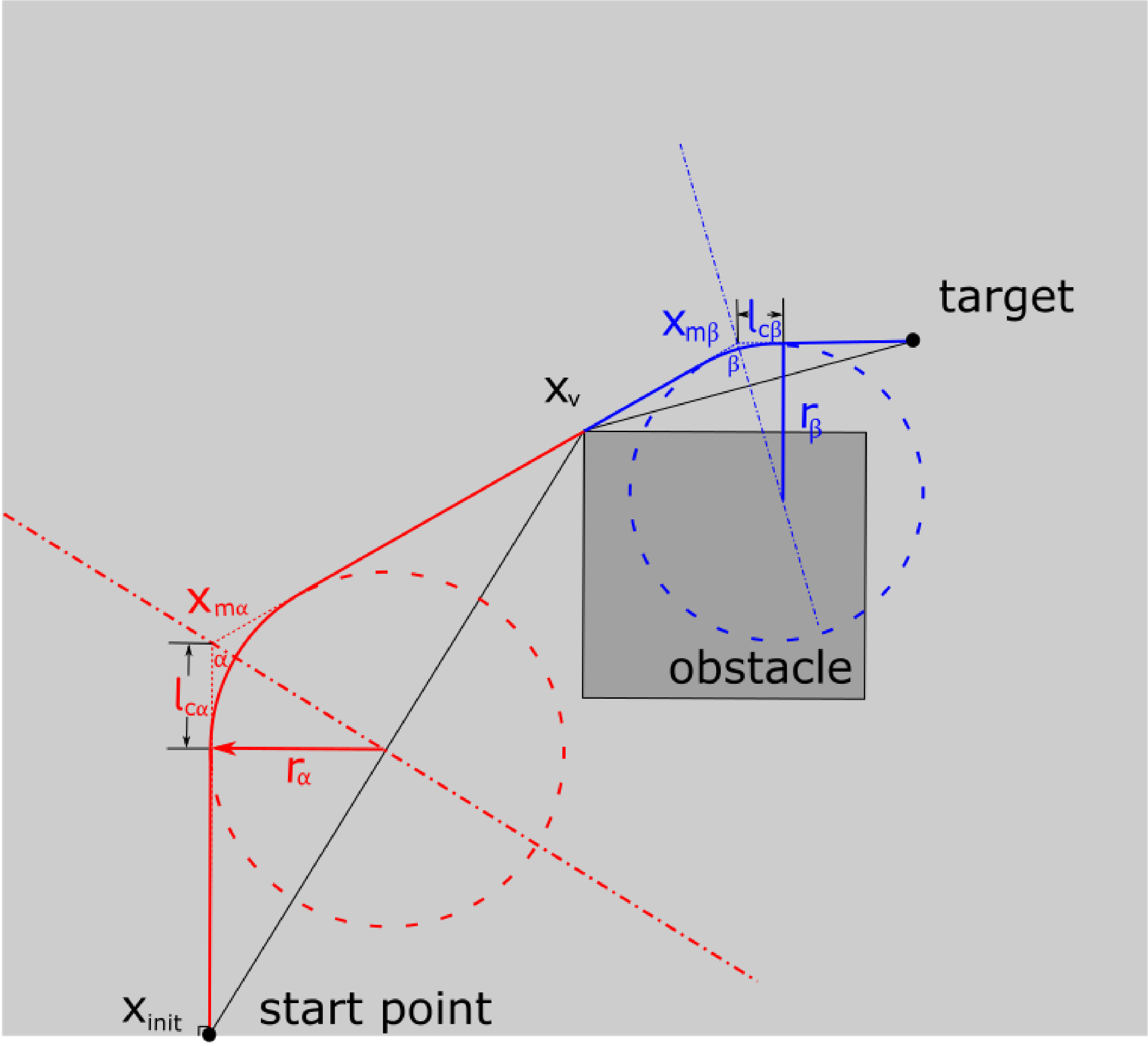

Figure 3.9: SCS path planner. r_α and r_β indicate the minimal reachable insertion radius. Reorientations are valid when $l_{c\alpha}$ greater the distance from start point x_{init} to $x_{m\alpha}$ and $l_{c\beta}$ greater the distance from $x_{m\alpha}$ to target location

The re-planning process happens after each reorientation where the needle tip could point to an undesired direction due to manipulation error. Once the needle deviates from the planned path, the planner takes the current location as an initial point to re-plan the path. As shown in Figure 3.10

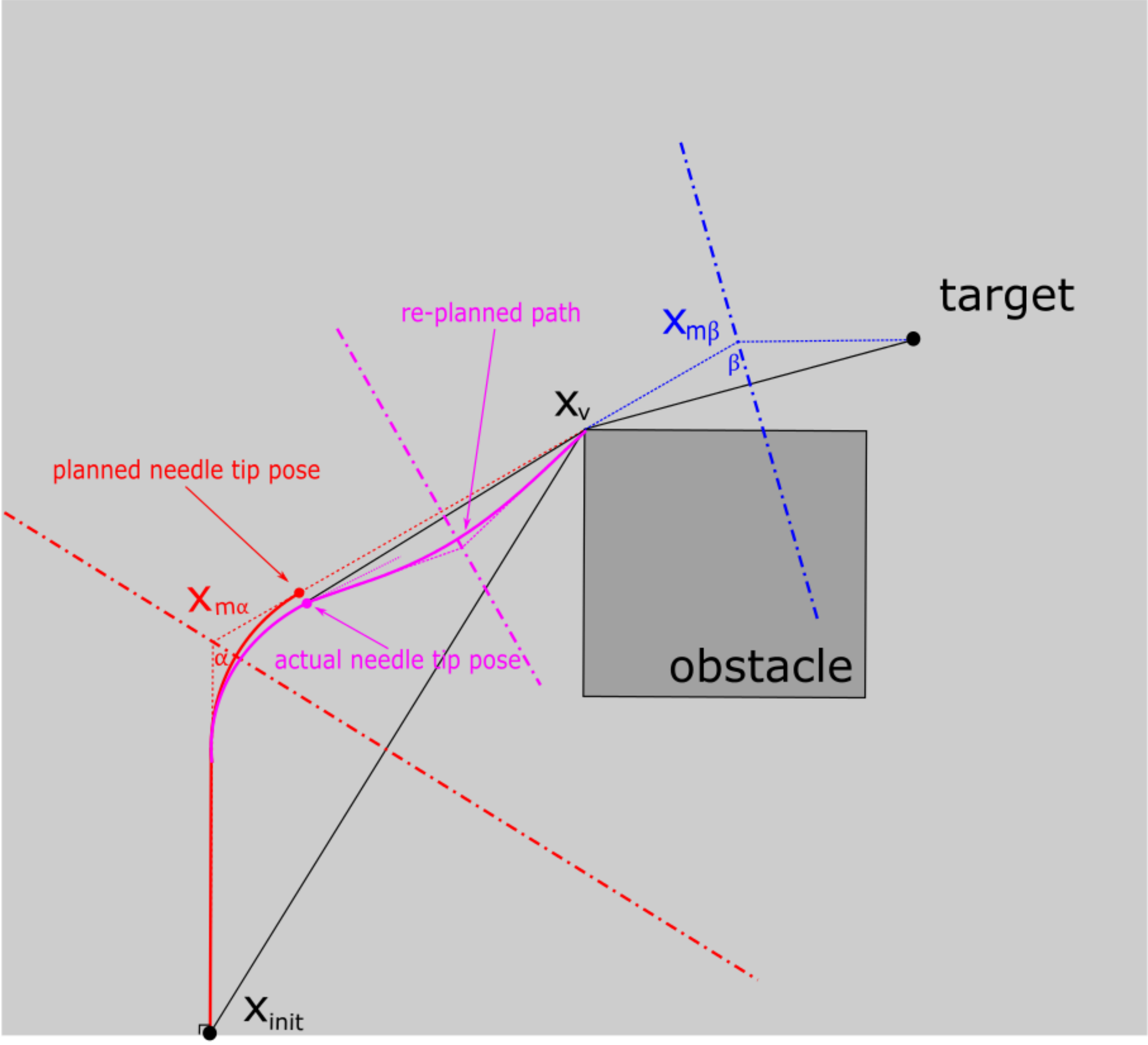

Figure 3.10: Re-planning of SCS path planner.

The planning strategy of the proposed SCS planner is adjustable by tuning the insertion radius selection. If the planning is focused on reducing distance expenses, the selection of the insertion radius is set to ascending search. If the planning strategy is aimed at reducing tissue strain, the selection of insertion radius can be set to descending search.

3.5 Discussion

3.5.1 Algorithm Performance

The proposed RG-RRT based planner was tested in MatLab environment on a 2.60GHz 4-core Intel®Core™i7 PC. 40 trails were performed using random start nodes on sidewalls. The average CPU time for obtaining an optimized path without re-planning was 2.74s, together with a 100% successful rate. The path planning performed in 15% SEBS tissue using high bending stiffness tube-wire combination is shown in Figure 3.6, the mechanical properties of corresponding tube, wire, and tissue phantom can be found in Table 2.11 and 2.12. Targeting errors along x-axis, y-axis, and z-axis are 0.27±0.24mm, 0.31±0.31mm, and 0.41±0.34mm respectively. The size of state space is 100mm * 100mm * 20mm.

3.5.2 Additional Error Caused by Correlation between Insertion Radius and Step Length

All of the resultant insertion radii of fracture-directed steerable needles have a corresponding step length. This leads to the situation that not all planned insertion circular arc can be precisely followed since the length of the insertion arcs is not necessarily the integer multiple of step length. In the presented simulation, the needle follows the planned path until the maximum integral multiple of step length has been reached, then the remainder which is the remaining length of the arc will be directly followed with an equivalent step length. Such behavior brings a minor error to the needle tip pose, thus, adjustments provided by re-planning algorithm is essential to achieve a successful insertion.

3.5.3 Late-stage Correction Challenge in RG-RRT Based Planner

Despite the minor error occurs at the end of each insertion segment. There is another reason that closed-loop re-planning serving a critical component of fracture-directed steerable needles. Unlike bevel-tip steerable needles that only have a lower boundary of its insertion radius, the insertion radius of fracture-directed steerable needles is limited by both lower boundary and upper boundary. Although fracture-directed steerable needles have outstanding performance in narrow space based on its ability to reach a tight radius as small as 6.9mm while using TPU(Thermoplastic polyurethane) tube, it suffers from the corresponding upper limit 14.4mm at the same time. This characteristic directly restricted the flexibility of late-stage insertion correction. The late-stage correction of bevel-tip steerable needles can be simply driving towards the target while performing fine-tuning using the duty-cycle technique. The fracture-directed steerable needles are unable to correct its orientation once the target location falls out of the reachable insertion radii due to inaccurate needle insertion. From the perspective of the path planning algorithm, one way of solving the late-stage correction problem is to plan the path only around the midpoint of reachable insertion radii when close to the target location. Another solution is to break down the planning based on the insertion segment into insertion steps, but such modification will result in a significant increase of CPU time.

3.5.4 Heuristic Algorithm of SCS path planner

A heuristic path planning algorithm was presented to provide a possible path planning approach that reduces the distance expense of insertions. This proposed SCS path planner first selects the shortest path from a start point to the target location then drive the needle tip through fillets with minimum reachable insertion radius to re-orient. Due to the boundaries of achievable insertion radii, the SCS planner may not be able to find a valid path for some initial points or re-plan a new path from a deviated endpoint of insertion. The sacrifice of success rate on random start points brings the capability of obtaining the lowest distance expense path from a selected initial point.

3.6 Conclusion

In this chapter, the kinematic model of fracture-directed steerable needles was introduced. A RG-RRT based path planning and re-planning algorithm were also presented. The advantages and disadvantages of this path planning algorithm were discussed regards the characteristics of fracture-directed steerable needles. The presented RG-RRT based planner was tested in MatLab environment on a 2.60GHz 4-core Intel®Core™i7 PC. 40 trails were performed using random start nodes on sidewalls. The average CPU time for obtaining an optimized path without re-planning was 2.74s, together with a 100% successful rate. A heuristic path planning algorithm was also presented for achieving the lowest distance expense path in two-dimensional space, this algorithm will be further developed to accommodate three-dimensional path planning and needle steering.

CHAPTER FOUR

CONCLUSION AND FUTURE WORK

This dissertation has presented a new class of needle insertion systems named as fracture-directed steerable needles. A comprehensive predictive model for resultant insertion radius has been developed so that the resultant needle tip positions of insertions with all different types of needle tip shapes, stylet geometries, step lengths, and tissue phantom Young's Moduli can be estimated. Then a RG-RRT based path planning algorithm was proposed based on the predictive model to perform needle steering in three-dimensional space.

4.1 Design of Needle Insertion Device

The design and assembly of a new class of needle insertion system named as fracture-directed steerable needles have been presented in chapter 2. The main part of the needle insertion system consists of two linear slides and one rotational servo motor. Other components, including limit switches, collets and bearings, are connected to the main structure by 3D printed parts and traditional fasteners. The linear slide and servo motor are controlled by micro-step drivers to achieve accurate linear motion and the rotational servo achieves accurate rotational motion through internal feedback. The control of the needle insertion device is accomplished through firmware running on a chipKit uC32 microcontroller, which accepts simple linear and rotational velocity commands from a PC running control scripts in the Python environment. The microcontroller is continually monitoring the status of the limit switches to ensure no portion of the system is driven past its physical limits. This robotic solution enables coordinated simultaneous motions of two input degrees of freedom. The insertion system was designed to drive the needle in one translational motion along the needle shaft and one rotational motion about the needle shaft. Actuators control the speed of insertion and rotation, l and θ directly for an insertion radius r. A simultaneous rotation mechanism was implemented to address the rotation lag caused by the friction between stylet and tissue phantom. Collets were installed concentric and coaxial on both tube and wire platforms to enhance the grip of nitinol materials and avoid buckling. Limit switches were applied to prevent the over retraction or insertion of the inner nitinol wire so the actual step length can accurately fall under the range of insertion radius predictive model.

4.2 Pre-shaped Needle & Step Length Model

Generally, the insertion radius decreases with decreased step length. For each combination of tissues and stylet shapes, we have used several equal-interval step lengths to get different curvatures of needle insertion. The achievable insertion radius, as a function of the step length of the stylet out of the tube before following with the tube, can be fitted with a high degree of accuracy to a line. For each of the stylet designs, the demonstrated linear relationship between step length and curvature is valid for a limited range of the insert lengths tested.

4.3 Resultant Insertion Radius & Mechanical Properties of the Soft Tissue, and the Needle

The equations related to the bending stiffness and curvature for calculating multiple overlapped curved tubes has been developed by Webster *et. al.*[71]:

$$\kappa_C = \frac{\sum_{i=1}^{n} E_i I_i \kappa_i}{\sum_{i=1}^{n} E_i I_i} = \frac{K_t \kappa_t + K_b \kappa_b + K_w \kappa_w}{K_t + K_b + K_w} \tag{4.1}$$

where κ_C is the combined curvature where the tube and wire are fully overlapped, and κ_t, κ_b, κ_w and K_t, K_b, K_w are the curvature and bending stiffness of the tissue channel, tube, and wire, respectively. I_i is the cross-sectional moment of inertia and E is the Young's Modulus.

$$K_i = E_i I_i \tag{4.2}$$

The product of the Young's Modulus (Modulus of Elasticity) and cross-sectional moment of inertia is bending stiffness. Here is where we make the assumption and treat the tissue channel as an outer tube. Because of the relatively small strains of the tissue using the relative stiffness heuristic, this simplifying assumption is valid.

By switching K_t to the left side, we can obtain equation below from equation(4.1):

$$K_t = \frac{K_b\kappa_b - K_b\kappa_C + K_w\kappa_w - K_w\kappa_C}{\kappa_C - \kappa_t} \tag{4.3}$$

Since the Nitinol tubes we used in the experiment are straight and the tissue channel holds the same curvature as the wire, κ_b=0, κ_t=κ_w.

Thus, equation(4.3) can be written as:

$$K_t = \frac{-K_b\kappa_C + K_w\kappa_w - K_w\kappa_C}{\kappa_C - \kappa_w} \tag{4.4}$$

In fracture-directed stylet-and-tube needle steering approach, a channel is created first by an inner Nitinol stylet, and then is followed by a tube. Therefore, knowing the equivalent bending stiffness of the tissue channel after insertion of the needle is essential for predicting the resultant ROC and path planning. Thus, A finite element analysis has been developed for predicting equivalent bending stiffness of the tissue channel after needle insertion. The similarity of the models obtained from both FEA and experiments reveals that the insertion radius of curvature is predictable by given the mechanical properties of the combination of tissue phantom, tube, and wire at a selected step length. To achieve a quality insertion with scarce tissue damage, the bending stiffness of the wire should be approximately one magnitude lower than the bending stiffness of the tube. If the bending stiffness of the wire is too close to the bending stiffness of the tube, the combined curvature of the tube and wire will be relatively high which increases the difficulty at the beginning of the insertion. If the bending stiffness of the wire is too low from the bending stiffness of the tube, it's harder for the tube to follow the wire in relatively soft tissue. Since the equivalent bending stiffness of the tissue channel is a variable that reacts to the inserted stylet in this model.

4.4 Comprehensive Predictive Model of Insertion Radius of Curvature

A complete predictive model for the resultant insertion radius has been proposed, it's a combination of the mechanical property model and the step length model, it can be described as $\kappa_r = \mathrm{f}(\ell, K_w, K_b, K_t, \kappa_w, \kappa_b)$ where κ_r is the insertion curvature, ℓ is step length, κ_t, κ_b, κ_w and K_t, K_b, K_w are the curvature and bending stiffness of the tissue channel, tube, and wire, respectively. the comprehensive predictive models were established on the data grids obtained from experiments in various tissue phantoms. Experiments follow the standard insertion procedures described in the steering method section. A top view photo was taken after each insertion. Then a curve with constant curvature was fitted into the captured image using MatLab to acquire insertion radius at designated step length. Based on the relatively linear relationship between resultant radius and step length, once a proper combination of the outer tube and inner wire was selected for tissue phantom with specified Young's Modulus, a surface present resultant insertion radius can be generated. This model can be potentially expanded among different pre-set needle shapes and diverse tissue phantoms. Finite element analysis was conducted to enhance the reliability of all provided predictive models. Data points collected from FEA only had minor differences comparing to experimental data. The maximum relative error based on experimental data was observed in 25% SEBS tissue phantom with 0.04 strain nitinol wire and high bending stiffness tube, the value of the maximum relative error was 4.08%. More than 75% of relative errors were fallen under of range of 1.44%-2.27%.

4.5 Needle Steering Path Planning and Closed-loop Re-planning

The kinematic model of fracture-directed steerable needles was introduced as a preliminary of path planning algorithm. A RG-RRT based path planning and re-planning algorithm were presented. The advantage and disadvantage of this path planning algorithm were discussed regards the characteristics of fracture-directed steerable needles. The presented RG-RRT based planner was tested in MatLab environment on a 2.60GHz 4-core Intel®Core™i7 PC. 40 trails were performed using random start nodes on sidewalls. The average CPU time for obtaining an optimized path without re-planning was 2.74s, together with a 100% successful rate. A novel heuristic path planning algorithm named as straight-curve-straight method is proposed to lower down the distance expense. The low distance expense of this planner is benefited from the bending stiffness equilibrium of fracture-directed steering method. It always provides an optimized path with the lowest distance expense, and the strategy of planning can be adapted to the lowest tissue strain, etc. The remaining challenges for fracture-directed steerable needles research are to first conduct insertion experiments with proposed path planner in three-dimensional space to examine the controllability and planner performance. Then test both the adaptability of the proposed predictive model and the effectiveness of steering approach in ex vivo for clinical applications. A further development that extends the capability of the current straight-curve-straight method into three-dimensional space manipulation will also be future work for the research of fracture-directed steerable needles.

BIBLIOGRAPHY

[1] Niki Abolhassani and RajniV Patel. Deflection of a flexible needle during insertion into soft tissue. In *2006 International Conference of the IEEE Engineering in Medicine and Biology Society*, pages 3858–3861. IEEE, 2006.

[2] Troy K Adebar, Joseph D Greer, Paul F Laeseke, Gloria L Hwang, and Allison M Okamura. Methods for improving the curvature of steerable needles in biological tissue. *IEEE Transactions on Biomedical Engineering*, 63(6):1167–1177, 2016.

[3] Ron Alterovitz and Ken Goldberg. *Motion planning in medicine: Optimization and simulation algorithms for image-guided procedures.* Springer, 2008.

[4] Mariana C Bernardes, Bruno V Adorno, Philippe Poignet, Nabil Zemiti, and Geovany A Borges. Adaptive path planning for steerable needles using duty-cycling. In *2011 IEEE/RSJ International Conference on Intelligent Robots and Systems*, pages 2545–2550. IEEE, 2011.

[5] John C Blasko, Tim Mate, John E Sylvester, Peter D Grimm, and William Cavanagh. Brachytherapy for carcinoma of the prostate: techniques, patient selection, and clinical outcomes. In *Seminars in radiation oncology*, volume 12, pages 81–94. Elsevier, 2002.

[6] Jordi Bruix, Morris Sherman, Josep M Llovet, Michel Beaugrand, Riccardo

Lencioni, Andrew K Burroughs, Erik Christensen, Luigi Pagliaro, Massimo Colombo, and Juan Rodés. Clinical management of hepatocellular carcinoma. conclusions of the barcelona-2000 easl conference. *Journal of hepatology*, 35(3):421–430, 2001.

[7] Van Khuyen Bui, Sukho Park, Jong-Oh Park, and Seong Young Ko. A novel curvature-controllable steerable needle for percutaneous intervention. *Proceedings of the Institution of Mechanical Engineers, Part H: Journal of Engineering in Medicine*, 230(8):727–738, 2016.

[8] Jessica Burgner, Philip J Swaney, Trevor L Bruns, Marlena S Clark, D Caleb Rucker, E Clif Burdette, and Robert J Webster. An autoclavable steerable cannula manual deployment device: Design and accuracy analysis. *Journal of medical devices*, 6(4), 2012.

[9] Christopher Burrows, Riccardo Secoli, and Ferdinando Rodriguez y Baena. Experimental characterisation of a biologically inspired 3d steering needle. In *2013 13th International Conference on Control, Automation and Systems (ICCAS 2013)*, pages 1252–1257. IEEE, 2013.

[10] Nuttapong Chentanez, Ron Alterovitz, Daniel Ritchie, Lita Cho, Kris K Hauser, Ken Goldberg, Jonathan R Shewchuk, and James F O'Brien. Interactive simula-

tion of surgical needle insertion and steering. In *ACM SIGGRAPH 2009 papers*, pages 1–10. 2009.

[11] HCM Clogenson, J Dankelman, and JJ van den Dobbelsteen. Steerable guidewire for magnetic resonance guided endovascular interventions. *Journal of Medical Devices*, 8(2), 2014.

[12] Noah J Cowan, Ken Goldberg, Gregory S Chirikjian, Gabor Fichtinger, Ron Alterovitz, Kyle B Reed, Vinutha Kallem, Wooram Park, Sarthak Misra, and Allison M Okamura. Robotic needle steering: Design, modeling, planning, and image guidance. In *Surgical robotics*, pages 557–582. Springer, 2011.

[13] M Dattoli, K Wallner, and J Blasko. Prostate brachytherapy made complicated, 2001.

[14] Simon P DiMaio and SE Salcudean. Needle steering and model-based trajectory planning. In *International Conference on Medical Image Computing and Computer-Assisted Intervention*, pages 33–40. Springer, 2003.

[15] Simon P DiMaio and Septimiu E Salcudean. Needle steering and motion planning in soft tissues. *IEEE Transactions on Biomedical Engineering*, 52(6):965–974, 2005.

[16] Vincent Duindam, Ron Alterovitz, Shankar Sastry, and Ken Goldberg. Screw-based motion planning for bevel-tip flexible needles in 3d environments with

obstacles. In *2008 IEEE international conference on robotics and automation*, pages 2483–2488. IEEE, 2008.

[17] Pierre E Dupont, Jesse Lock, Brandon Itkowitz, and Evan Butler. Design and control of concentric-tube robots. *IEEE Transactions on Robotics*, 26(2):209–225, 2009.

[18] Pierre E Dupont, Jesse Lock, Brandon Itkowitz, and Evan Butler. Design and control of concentric-tube robots. *IEEE Transactions on Robotics*, 26(2):209–225, 2010.

[19] Joann G Elmore, Gary M Longton, Patricia A Carney, Berta M Geller, Tracy Onega, Anna NA Tosteson, Heidi D Nelson, Margaret S Pepe, Kimberly H Allison, Stuart J Schnitt, et al. Diagnostic concordance among pathologists interpreting breast biopsy specimens. *Jama*, 313(11):1122–1132, 2015.

[20] Johnathan A Engh, Davneet S Minhas, Douglas Kondziolka, and Cameron N Riviere. Percutaneous intracerebral navigation by duty-cycled spinning of flexible bevel-tipped needles. *Neurosurgery*, 67(4):1117–1123, 2010.

[21] Johnathan A Engh, Gregg Podnar, Si Yi Khoo, and CN Riviere. Flexible needle steering system for percutaneous access to deep zones of the brain. In *Proceedings of the IEEE 32nd annual northeast bioengineering conference*, pages 103–104. IEEE, 2006.

[22] Gabor Fichtinger, Jonathan P Fiene, Christopher W Kennedy, Gernot Kronreif, Iulian Iordachita, Danny Y Song, Everette C Burdette, and Peter Kazanzides. Robotic assistance for ultrasound-guided prostate brachytherapy. *Medical image analysis*, 12(5):535–545, 2008.

[23] Giada Gerboni, Joseph D Greer, Paul F Laeseke, Gloria L Hwang, and Allison M Okamura. Highly articulated robotic needle achieves distributed ablation of liver tissue. *IEEE Robotics and Automation Letters*, 2017.

[24] Daniel Glozman and Moshe Shoham. Flexible needle steering and optimal trajectory planning for percutaneous therapies. In *International Conference on Medical Image Computing and Computer-Assisted Intervention*, pages 137–144. Springer, 2004.

[25] Daniel Glozman and Moshe Shoham. Image-guided robotic flexible needle steering. *IEEE Transactions on Robotics*, 23(3):459–467, 2007.

[26] Henry Ford Hospital. Newly approved ultrasound device eliminates risks and pain of liver biopsy. *PR Newswire.*

[27] Mohamed Gouse Jushiddi, John JE Mulvihill, Drahomir Chovan, Aladin Mani, Camelia Shanahan, Christophe Silien, Syed Ansar Md Tofail, and Peter Tiernan. Simulation of biopsy bevel-tipped needle insertion into soft-gel. *Computers in biology and medicine*, 111:103337, 2019.

[28] Vinutha Kallem and Noah J Cowan. Image guidance of flexible tip-steerable needles. *IEEE Transactions on Robotics*, 25(1):191–196, 2009.

[29] Mohsen Khadem, Carlos Rossa, Nawaid Usmani, Ron S Sloboda, and Mahdi Tavakoli. Introducing notched flexible needles with increased deflection curvature in soft tissue. In *Advanced Intelligent Mechatronics (AIM), 2016 IEEE International Conference on*, pages 1186–1191. IEEE, 2016.

[30] Zahra Khashei Varnamkhasti and Bardia Konh. Design and performance study of a novel minimally invasive active surgical needle. *Journal of Medical Devices*, 13(4), 2019.

[31] Seong Young Ko, Brian L Davies, and Ferdinando Rodriguez y Baena. Two-dimensional needle steering with a "programmable bevel" inspired by nature: Modeling preliminaries. In *2010 IEEE/RSJ International Conference on Intelligent Robots and Systems*, pages 2319–2324. IEEE, 2010.

[32] Seong Young Ko and Ferdinando Rodriguez y Baena. Toward a miniaturized needle steering system with path planning for obstacle avoidance. *IEEE Transactions on Biomedical Engineering*, 60(4):910–917, 2012.

[33] Louis B Kratchman, Mohammed M Rahman, Justin R Saunders, Philip J Swaney, and Robert J Webster III. Toward robotic needle steering in lung biopsy: a tendon-actuated approach. In *Medical Imaging 2011: Visualization,*

Image-Guided Procedures, and Modeling, volume 7964, page 79641I. International Society for Optics and Photonics, 2011.

[34] James J Kuffner and Steven M LaValle. Rrt-connect: An efficient approach to single-query path planning. In *Proceedings 2000 ICRA. Millennium Conference. IEEE International Conference on Robotics and Automation. Symposia Proceedings (Cat. No. 00CH37065)*, volume 2, pages 995–1001. IEEE, 2000.

[35] Ann Majewicz, Steven P Marra, Mark G Van Vledder, MingDe Lin, Michael A Choti, Danny Y Song, and Allison M Okamura. Behavior of tip-steerable needles in ex vivo and in vivo tissue. *IEEE Transactions on Biomedical Engineering*, 59(10):2705–2715, 2012.

[36] The American Cancer Society medical and editorial content team. Key statistics about liver cancer. *American Cancer Society.*

[37] The American Cancer Society medical and editorial content team. Key statistics for prostate cancer. *American Cancer Society.*

[38] Sarthak Misra, Kyle B Reed, Andrew S Douglas, KT Ramesh, and Allison M Okamura. Needle-tissue interaction forces for bevel-tip steerable needles. In *Biomedical Robotics and Biomechatronics, 2008. BioRob 2008. 2nd IEEE RAS & EMBS International Conference on*, pages 224–231. IEEE, 2008.

[39] Sarthak Misra, Kyle B Reed, Benjamin W Schafer, KT Ramesh, and Allison M Okamura. Mechanics of flexible needles robotically steered through soft tissue. *The International journal of robotics research*, 29(13):1640–1660, 2010.

[40] Randy A Mrozek, Brad Leighliter, Christopher S Gold, Ian R Beringer, H Yu Jian, Mark R VanLandingham, Paul Moy, Mark H Foster, and Joseph L Lenhart. The relationship between mechanical properties and ballistic penetration depth in a viscoelastic gel. *Journal of the mechanical behavior of biomedical materials*, 44:109–120, 2015.

[41] Maria Neumann and Jessica Burgner-Kahrs. Considerations for follow-the-leader motion of extensible tendon-driven continuum robots. In *Robotics and Automation (ICRA), 2016 IEEE International Conference on*, pages 917–923. IEEE, 2016.

[42] Stephen Okazawa, Richelle Ebrahimi, Jason Chuang, Septimiu E Salcudean, and Robert Rohling. Hand-held steerable needle device. *IEEE/ASME Transactions on Mechatronics*, 10(3):285–296, 2005.

[43] Matthew J Oldfield, Alexander Leibinger, Tian En Timothy Seah, and Ferdinando Rodriguez y Baena. Method to reduce target motion through needle–tissue interactions. *Annals of biomedical engineering*, 43(11):2794–2803, 2015.

[44] Mark D O'Leary, Christina Simone, Toshikatsu Washio, Kiyoshi Yoshinaka, and

Allison M Okamura. Robotic needle insertion: Effects of friction and needle geometry. In *2003 IEEE International Conference on Robotics and Automation (Cat. No. 03CH37422)*, volume 2, pages 1774–1780. IEEE, 2003.

[45] James D Pampush, David J Daegling, Anna E Vick, W Scott McGraw, Ryan M Covey, and Andrew J Rapoff. Technical note: Converting durometer data into elastic modulus in biological materials. *American journal of physical anthropology*, 146(4):650–653, 2011.

[46] Wooram Park, Jin Seob Kim, Yu Zhou, Noah J. Cowan, Allison M. Okamura, and Gregory S. Chirikjian. Diffusion-based motion planning for a nonholonomic flexible needle model. In *Proc. IEEE Int. Conf. Robot. Autom.*, pages 4600–4605, Barcelona, Spain, April 2005. IEEE.

[47] Wooram Park, Kyle B. Reed, Allison M. Okamura, and Gregory S. Chirikjian. Estimation of model parameters for steerable needles. *Proc. IEEE Int. Conf. Robot. Autom.*, pages 3703 –3708, may. 2010.

[48] Sachin Patil and Ron Alterovitz. Interactive motion planning for steerable needles in 3d environments with obstacles. In *2010 3rd IEEE RAS & EMBS International Conference on Biomedical Robotics and Biomechatronics*, pages 893–899. IEEE, 2010.

[49] Andrew J Petruska, Fabio Ruetz, Ayoung Hong, Luca Regli, Oguzkan Sürücü,

Ajmal Zemmar, and Bradley J Nelson. Magnetic needle guidance for neurosurgery: Initial design and proof of concept. In *Robotics and Automation (ICRA), 2016 IEEE International Conference on*, pages 4392–4397. IEEE, 2016.

[50] HJ Qi, K Joyce, and MC Boyce. Durometer hardness and the stress-strain behavior of elastomeric materials. *Rubber chemistry and technology*, 76(2):419–435, 2003.

[51] Kyle B Reed, Ann Majewicz, Vinutha Kallem, Ron Alterovitz, Ken Goldberg, Noah J Cowan, and Allison M Okamura. Robot-assisted needle steering. *IEEE robotics & automation magazine*, 18(4):35–46, 2011.

[52] Kyle B. Reed, Allison M. Okamura, and Noah J. Cowan. Modeling and control of needles with torsional friction. *IEEE Trans. Biomed. Eng.*, 56(12):2905–2916, December 2009. NIHMS192959.

[53] Marta Scali, Tim P Pusch, Paul Breedveld, and Dimitra Dodou. Needle-like instruments for steering through solid organs: A review of the scientific and patent literature. *Proceedings of the Institution of Mechanical Engineers, Part H: Journal of Engineering in Medicine*, page 0954411916672149, 2016.

[54] Marta Scali, Paulien AH Veldhoven, Paul WJ Henselmans, Dimitra Dodou, and Paul Breedveld. Design of an ultra-thin steerable probe for percutaneous in-

terventions and preliminary evaluation in a gelatine phantom. *PloS one*, 14(9), 2019.

[55] Patrick Sears and Pierre Dupont. A steerable needle technology using curved concentric tubes. In *2006 IEEE/RSJ international conference on intelligent robots and systems*, pages 2850–2856. IEEE, 2006.

[56] Riccardo Secoli and Ferdinando Rodriguez y Baena. Closed-loop 3d motion modeling and control of a steerable needle for soft tissue surgery. In *2013 IEEE International Conference on Robotics and Automation*, pages 5831–5836. IEEE, 2013.

[57] Alexander Shkolnik, Matthew Walter, and Russ Tedrake. Reachability-guided sampling for planning under differential constraints. In *2009 IEEE International Conference on Robotics and Automation*, pages 2859–2865. IEEE, 2009.

[58] Inc. Smooth-On. Addition cure silicone rubber compounds product and technical review @MISC, May 2017.

[59] Inc. Smooth-On. Super-soft, addition cure silicone rubbers product and technical review @MISC, May 2017.

[60] Philip J Swaney, Jessica Burgner, Hunter B Gilbert, and Robert J Webster. A flexure-based steerable needle: high curvature with reduced tissue damage. *IEEE Transactions on Biomedical Engineering*, 60(4):906–909, 2012.

[61] Philip J Swaney, Jessica Burgner, Hunter B Gilbert, and Robert J Webster. A flexure-based steerable needle: high curvature with reduced tissue damage. *IEEE Transactions on Biomedical Engineering*, 60(4):906–909, 2013.

[62] John P Swensen and Noah J Cowan. Torsional dynamics compensation enhances robotic control of tip-steerable needles. In *Robotics and Automation (ICRA), 2012 IEEE International Conference on*, pages 1601–1606. IEEE, 2012.

[63] Russell H Taylor. A perspective on medical robotics. *Proceedings of the IEEE*, 94(9):1652–1664, 2006.

[64] Nick J van de Berg, Tonke L de Jong, Dennis J van Gerwen, Jenny Dankelman, and John J van den Dobbelsteen. The influence of tip shape on bending force during needle insertion. *Scientific Reports*, 7:40477, 2017.

[65] Nick J van de Berg, Dennis J van Gerwen, Jenny Dankelman, and John J van den Dobbelsteen. Design choices in needle steering—a review. *IEEE/ASME Transactions on Mechatronics*, 20(5):2172–2183, 2014.

[66] Jur Van Den Berg, Sachin Patil, Ron Alterovitz, Pieter Abbeel, and Ken Goldberg. Lqg-based planning, sensing, and control of steerable needles. In *Algorithmic Foundations of Robotics IX*, pages 373–389. Springer, 2010.

[67] Robert J Webster, Jasenka Memisevic, and Allison M Okamura. Design consider-

ations for robotic needle steering. In *Proceedings of the 2005 IEEE International Conference on Robotics and Automation*, pages 3588–3594. IEEE, 2005.

[68] Robert J. Webster III, Jin S. Kim, Noah J. Cowan, Greg S. Chirikjian, and Allison M. Okamura. Nonholonomic modeling of needle steering. *Int. J. Robot. Res.*, 25(5/6):509–526, May 2006.

[69] Robert J Webster III, Jin Seob Kim, Noah J Cowan, Gregory S Chirikjian, and Allison M Okamura. Nonholonomic modeling of needle steering. *The International Journal of Robotics Research*, 25(5-6):509–525, 2006.

[70] Robert J Webster III, Joseph M Romano, and Noah J Cowan. Mechanics of precurved-tube continuum robots. *IEEE Transactions on Robotics*, 25(1):67–78, 2008.

[71] Robert J Webster III, Joseph M Romano, and Noah J Cowan. Mechanics of precurved-tube continuum robots. *IEEE Transactions on Robotics*, 25(1):67–78, 2009.

[72] Thomas R Wedlick and Allison M Okamura. Characterization of pre-curved needles for steering in tissue. In *Engineering in Medicine and Biology Society, 2009. EMBC 2009. Annual International Conference of the IEEE*, pages 1200–1203. IEEE, 2009.

[73] Peter NT Wells and Hai-Dong Liang. Medical ultrasound: imaging of soft tissue strain and elasticity. *Journal of the Royal Society Interface*, 8(64):1521–1549, 2011.

[74] Jijie Xu, Vincent Duindam, Ron Alterovitz, and Ken Goldberg. Motion planning for steerable needles in 3d environments with obstacles using rapidly-exploring random trees and backchaining. In *2008 IEEE international conference on automation science and engineering*, pages 41–46. IEEE, 2008.

[75] Fan Yang, Mahdieh Babaiasl, and John P Swensen. Fracture-directed steerable needles. *Journal of Medical Robotics Research*, page 1842002, 2018.

[76] Fan Yang, Mahdieh Babaiasl, and John P Swensen. Fracture-directed steerable needles. *Journal of Medical Robotics Research*, 4(01):1842002, 2019.

[77] Peter A York, Philip J Swaney, Hunter B Gilbert, and Robert J Webster. A wrist for needle-sized surgical robots. In *2015 IEEE International Conference on Robotics and Automation (ICRA)*, pages 1776–1781. IEEE, 2015.